

ABSTRACT

Title of Document: INVESTIGATION OF PULSED COHERENT
INJECTION LOCKING OF A MODE-
LOCKED LASER

Arthur Wayne Liu, Master of Science, 2007

Directed By: Professor Julius Goldhar
Department of Electrical and Computer
Engineering

Pulsed coherent injection locking of a mode-locked laser was investigated. This method combines optically-driven mode-locking with coherent injection locking to produce pulsed light which is both synchronized and optically coherent with an injected signal. A high quality pulse train from a commercial laser was injected into a monolithic mode-locked laser fabricated at the Laboratory for Physical Sciences. A coherent output was achieved when the repetition rate was matched and the longitudinal modes were tuned correctly. Under these conditions we observed a dip in the reflected injecting signal, indicating destructive interference with the monolithic laser output. While this serves as a simple monitor for coherent injection, the coherently locked output spectrum was significantly broader than that of the injected signal and a small change in mode detuning produced a large spectral change. The variations of temporal and spectral characteristics of the monolithic laser were qualitatively explained with a simple theoretical model.

INVESTIGATION OF
PULSED COHERENT INJECTION LOCKING
OF A MODE-LOCKED LASER

By

Arthur Wayne Liu

Thesis submitted to the Faculty of the Graduate School of the
University of Maryland, College Park, in partial fulfillment
of the requirements for the degree of
Master of Science
2007

Advisory Committee:
Professor Julius Goldhar, Chair/Advisor
Professor Thomas E. Murphy
Dr. Christopher J.K. Richardson

© Copyright by
Arthur Wayne Liu
2007

Dedication

To my parents.

Acknowledgements

First, I would like to thank my advisor, Professor Julius Goldhar, for the opportunity he has granted me as a research assistant. His guidance in my research has been invaluable. I have benefited from his knowledge both as a student in several of his courses, and as a research assistant in his lab. In addition to his technical expertise, his enthusiasm for research has inspired me. I have appreciated his friendly personality and the patience with which he answers my questions, no matter how simple they may be.

I would also like to thank Dr. Christopher J. K. Richardson. This thesis would not have been possible without his work on the design and fabrication of colliding pulse mode-locked lasers with tunable repetition rates.

I would also like to thank Dr. Thomas E. Murphy. I learned a great deal in his course on nonlinear optics. I am grateful to both Dr. Richardson and Dr. Murphy for serving on my thesis examining committee. I appreciate all the comments they offered.

I would like to acknowledge the fellow students who worked with me on my research. Dr. Shuo-Yen Tseng served as a mentor to me during my initial months at the Laboratory for Physical Sciences (LPS). He introduced me to the basic aspects of working with optical components, such as splicing optical fibers and aligning the optical cross-correlator. The experiment I performed on optical switching using cross phase modulation is based on the theoretical treatment in his dissertation.

I would also like to acknowledge Arun Mampazhy for his work on fabricating the self colliding pulse mode-locked laser. Arun and I worked together to characterize the laser and gather the data presented in this thesis. His proposal work was instrumental in helping me to understand the operation of the laser.

I would like to mention the other students and researchers at LPS who have befriended me and supported me along the way. They include Ricardo Pizarro, Dyan Ali, Dong Hun Park, Victor Yun, Dr. Yongzhang Leng, Dr. Younggu Kim, Wei-Yen Chen, and Li-Chiang Simon Kuo. I have enjoyed our conversations around the lunch table, at the coffee shop, and around the lab.

I would like to thank all of my friends, especially Benjamin Snow, for their companionship and encouragement. Finally and most importantly, I would like to thank my family for their constant love and support.

Table of Contents

| | |
|--|-----|
| Dedication..... | ii |
| Acknowledgements..... | iii |
| Table of Contents..... | v |
| List of Figures..... | vi |
| Chapter 1: Introduction..... | 1 |
| Chapter 2: Pulse propagation in a single pass semiconductor optical amplifier (SOA) | 5 |
| 2.1 Introduction..... | 5 |
| 2.2 Nonlinear pulse propagation in single mode optical waveguides..... | 6 |
| 2.3 Pulse propagation in semiconductor optical amplifiers..... | 11 |
| 2.4 Optical switching using XPM in SOAs..... | 20 |
| 2.4.1 Operating principle..... | 20 |
| 2.4.2 Experiment on XPM in SOAs..... | 21 |
| 2.4.3 Modeling of XPM in SOAs..... | 30 |
| Chapter 3: Semiconductor Monolithic Mode-locked Lasers..... | 35 |
| 3.2 Techniques of Mode-locking..... | 41 |
| 3.3 Types of Semiconductor Mode-locked Lasers..... | 45 |
| 3.4 Experiments with Passive Mode-locking in a SCPM Laser..... | 51 |
| Chapter 4: CW Injection Locking in Monolithic Lasers..... | 65 |
| 4.1 Introduction to CW Injection Locking Theory..... | 65 |
| 4.2 Experiment on CW Injection Locking in Monolithic Lasers..... | 75 |
| 4.3 Reflected Power as a Diagnostic for CW Injection Locking..... | 82 |
| Chapter 5: Pulsed Coherent Injection Locking of a Mode-locked Laser..... | 91 |
| 5.1 Description of Pulsed Coherent Injection Locking of a Mode-locked Laser .. | 91 |
| 5.2 Experimental Setup..... | 95 |
| 5.3 Experimental Results..... | 101 |
| Chapter 6: Theoretical Model..... | 126 |
| Chapter 7: Conclusion..... | 140 |
| Appendix..... | 143 |
| Bibliography..... | 151 |

List of Figures

| | |
|---|----|
| Figure 2.1: The time dependent gain (a) and phase shift (b) of an SOA with 2.7 ps FWHM input pulse. | 18 |
| Figure 2.2: Calculated input and output pulse shape from a typical SOA..... | 19 |
| Figure 2.3: Schematic of an optical switch using XPM in an SOA..... | 20 |
| Figure 2.4: Experimental setup for demonstrating the switching window in an SOA. EDFA: Erbium doped fiber amplifier. BPF: Band-pass filter. FBG: Fiber Bragg grating. PC: Polarization controller. CORR: Cross-correlator. | 23 |
| Figure 2.5: Measured spectra of CW signal input to SOA (dotted line) and broadened CW output (solid line). The longer-wavelength broadening is clearly evident. Some shorter-wavelength broadening is also present. The input curve has been shifted up by a constant 7.5 dBm for purpose of comparison. | 24 |
| Figure 2.6: Experimental setup for measuring auto-correlation of ML pulses..... | 27 |
| Figure 2.7: Measured auto-correlation of ML pulse. Data (solid line) is plotted along with simulated 3.82ps FWHM Gaussian pulse (dotted line). | 28 |
| Figure 2.8: Cross-correlation measurement of switching window (solid line) with simulated Gaussian (dotted line) of 5.4 ps FWHM for comparison. | 29 |
| Figure 2.9: Cross-correlation measurement as in Figure 2.7, but with only control pulses (solid line) or only CW signal (dotted line). | 30 |
| Figure 2.10: Simulated spectra of CW signal input to SOA (dashed line) and broadened CW output (solid line). The longer-wavelength broadening is clearly evident. | 32 |
| Figure 2.11: Measured transmission functions (solid lines) of the two BPFs placed after the SOA in the switching experiment. The model uses Gaussian curves (dotted lines) with peak transmission and FWHM chosen to match the measured transmission functions. | 33 |
| Figure 2.12: Measured (solid line) and simulated (dotted line) transmission functions of the FBG placed after the SOA in the switching experiment. | 33 |
| Figure 2.13: Simulated switching window, with FWHM equal to 4.3 ps. Compare to experimental result, with FWHM about 4.7 ps (Figure 2.8)..... | 34 |
| Figure 3.1: Examples of signals in time that correspond to N equally spaced axial modes of different amplitude and phase distributions. | 40 |

| | |
|--|----|
| Figure 3.2: Free-running laser axial modes and modulation-induced sidebands..... | 42 |
| Figure 3.3: Process of passive mode-locking. | 44 |
| Figure 3.4: Schematic of tandem construction of monolithic passive mode-locked laser. | 47 |
| Figure 3.5: Schematic of colliding pulse (CPM) construction of monolithic passive mode-locked laser. | 48 |
| Figure 3.6: Schematic of colliding pulse (CPM) construction of monolithic passive mode-locked laser. | 49 |
| Figure 3.7: Schematic of ring construction of monolithic passive mode-locked laser (top view). | 50 |
| Figure 3.8: Schematic of extended cavity construction of monolithic passive mode-locked laser. | 51 |
| Figure 3.9: Schematic of cross-section of SCPM laser (not to scale). | 53 |
| Figure 3.10: Schematic of fabricated SCPM laser on submount and mount structure. | 55 |
| Figure 3.11: SCPM laser with input and output coupled through angled fiber tips. .. | 56 |
| Figure 3.12: Peak RF Repetition Frequency for different values of V_{SA} , I_{HG} , and I_{LG} | 60 |
| Figure 3.13: Measured RF spectrum of the monolithic laser in passive self colliding pulse mode-locking (SCPM) operation. High gain section is biased at $I_{HG} = 60$ mA , saturable absorber section is biased at $V_{SA} = -2.2$ V , and low gain section is biased at $I_{LG} = 220$ mA | 63 |
| Figure 3.14: Measured optical spectrum of the monolithic laser in passive self colliding pulse mode-locking (SCPM) operation. High gain section is biased at $I_{HG} = 60$ mA , saturable absorber section is biased at $V_{SA} = -2.2$ V , while low gain section biasing is varied with values $I_{LG} = 185$ mA, 205 mA, and 225 mA. | 64 |
| Figure 3.15: Measured auto-correlation trace of the monolithic laser in passive self colliding pulse mode-locking (SCPM) operation. High gain section is biased at $I_{HG} = 60$ mA , saturable absorber section is biased at $V_{SA} = -2.2$ V , and low gain section biasing is biased at $I_{LG} = 185$ mA | 64 |

| | |
|---|-----|
| Figure 4.1: Schematic of model for CW injection locking..... | 67 |
| Figure 4.2: Phase difference $\phi_1 - \phi$ between the injected wave and the injection locked laser output wave, for several values of the power ratio $P_{inc,refl} / P_{out}$ | 73 |
| Figure 4.3: Phasor diagrams for injection locked laser, at center and at edges of locking range..... | 74 |
| Figure 4.4: Calculated output intensity of a CW laser as a function of pumping ratio. The condition $r = 1$ corresponds to laser threshold..... | 77 |
| Figure 4.5: Measured optical output power of fabricated laser in CW mode as a function of uniform pumping current. | 78 |
| Figure 4.6: Measured optical spectrum of free-running CW laser. | 79 |
| Figure 4.7: Measured optical spectrum of Photonetics CW laser signal. | 81 |
| Figure 4.8: Measured optical spectrum of CW injection locked laser..... | 81 |
| Figure 4.9: Modified schematic of model of CW injection locking..... | 83 |
| Figure 4.10: Total output power from injection side facet of laser, when injection locking is achieved..... | 86 |
| Figure 4.11: Measured total power from injection side of laser, as pumping current is tuned, for power ratio of 1/10. | 89 |
| Figure 4.12: Measured total power from injection side of laser, as pumping current is tuned, for power ratio of 1/100. | 89 |
| Figure 5.1: Diagram illustrating optically-driven active or hybrid mode-locking..... | 93 |
| Figure 5.2: Diagram illustrating pulsed coherent injection locking. | 94 |
| Figure 5.3: Experimental setup for demonstrating pulsed injection locking of a self colliding pulse mode-locked (SCPM) laser. ML Laser: commercial hybrid mode- locked laser. EDFA: Erbium doped fiber amplifier. BPF: Band-pass filter. ATT: Variable optical attenuator. SCPM Laser: monolithic, passive self colliding pulse mode-locked laser. POW: Optical power meter. POL: Optical polarization analyzer. OSA: Optical spectrum analyzer. RFSA: Radio frequency (RF) spectrum analyzer. CORR: Cross correlator. PC: Polarization controller..... | 96 |
| Figure 5.4: Measured injection side interfered power as a function of low-gain section current I_{LG} , for a power ratio of $P_{inc} / P_{out} = 1/10$ | 103 |

| | |
|---|-----|
| Figure 5.5: Measured injection side interfered power as a function of low-gain section current I_{LG} , for a power ratio of $P_{inc}/P_{out} = 1/10$ | 103 |
| Figure 5.6: Reflected power curve for a power ratio of 1/10. The range over which RF locking occurs is marked..... | 106 |
| Figure 5.7: Reflected power curve for a power ratio of 1/100. The range over which RF locking occurs is marked..... | 106 |
| Figure 5.8: RF spectrum of pulsed injection locked SCPM laser, under bias condition such that it is RF locked to the injection laser. | 107 |
| Figure 5.9: RF spectrum of pulsed injection locked SCPM laser, under bias condition such that it is not RF locked to the injection laser. | 108 |
| Figure 5.10: Reflected power curve for a power ratio of 1/10. Labels A, B, C, and D correspond to the selected spectra at 204 mA, 213 mA, 214 mA, and 215 mA. | 110 |
| Figure 5.11: Measured output spectra of laser at 211 mA. Representative of the spectra outside the locking range. Spectra essentially same as free-running case. | 110 |
| Figure 5.12: Measured output spectra of laser at 213 mA. Representative of the spectra at the point of maximum power reduction. Shift to higher wavelengths. | 111 |
| Figure 5.13: Measured output spectra of laser at 214 mA. Representative of unstable condition at a point of moderate power reduction. | 111 |
| Figure 5.14: Measured output spectra of laser at 215 mA. Representative of spectra at a point of minimal power reduction. Shift to lower wavelengths..... | 112 |
| Figure 5.15: Cross-correlation trace at pumping current of 211 mA, corresponding to a point in RF locking range but outside coherent locking range. | 115 |
| Figure 5.16: Cross-correlation trace at pumping current of 213 mA, corresponding to the point of maximum power reduction..... | 115 |
| Figure 5.17: Cross-correlation trace at pumping current of 214 mA, corresponding to a point of moderate power reduction. | 116 |
| Figure 5.18: Cross-correlation trace at pumping current of 215 mA, corresponding to a point of minimal power reduction..... | 116 |

| | |
|---|-----|
| Figure 5.19: Reflected power curve for a power ratio of 1/100. Labels A, B, C, and D correspond to the selected spectra at 208 mA, 211 mA, 212 mA, and 213 mA. | 118 |
| Figure 5.20: Measured output spectra of laser at 208 mA. Representative of spectra outside the locking range. Spectra essentially same as free-running case..... | 119 |
| Figure 5.21: Measured output spectra of laser at 211 mA. Representative of spectra at the point of maximum power reduction. Weak shift to higher wavelengths. | 119 |
| Figure 5.22: Measured output spectra of laser at 212 mA. Representative of unstable condition at a point of moderate power reduction. | 120 |
| Figure 5.23: Measured output spectra of laser at 213 mA. Representative of spectra at a point of minimal power reduction. Shift to lower wavelengths..... | 120 |
| Figure 5.24: Cross-correlation trace at pumping current of 209 mA, corresponding to a point in RF locking range but outside coherent locking range. | 123 |
| Figure 5.25: Cross-correlation trace at pumping current of 211 mA, corresponding to the point of maximum power reduction..... | 123 |
| Figure 5.26: Cross-correlation trace at pumping current of 212 mA, corresponding to a point of moderate power reduction. | 124 |
| Figure 5.27: Cross-correlation trace at pumping current of 213 mA, corresponding to a point of minimal power reduction..... | 124 |
| Figure 6.1: Schematic of numerical model for pulsed injection locking of a mode-locked laser. | 126 |
| Figure 6.2: Calculated reflected power diagnostic. | 133 |
| Figure 6.3: Calculated laser spectra for various values of θ | 134 |
| Figure 6.4: Selected calculated laser output spectra, for values of θ within the coherent locking range. A shift in the peak of the spectrum occurs as θ is tuned. | 136 |
| Figure 6.5: Calculated laser pulses for various values of θ | 138 |
| Figure 6.6: Selected calculated laser pulses for values of θ within the coherent injection locking range..... | 138 |

Chapter 1: Introduction

Future optical telecommunications systems will require sources of pulsed light with repetition rates in the microwave range. Monolithic semiconductor mode-locked lasers are of great interest for generating such light signals. These devices are compact, easy to fabricate, and highly integrable into existing opto-electronic technology. However, monolithic lasers also suffer from several disadvantages, including timing jitter and broad optical spectra.

All-optical clock recovery is one possible application of monolithic lasers. Clock recovery is the generation of a clock signal that has the same repetition rate as an incoming optical data signal, and is synchronized with it. All-optical clock recovery directly uses the data signal to perform synchronization. Much research has been performed in this area. All-optical clock recovery can be achieved by injecting the data signal into a monolithic laser to establish optically-driven mode-locking. This has been demonstrated by a number of researchers [1], [2], [3], [4]. However, in these schemes, the optical frequency of the monolithic laser output is chosen to be different from that of the injected data. We refer to this case as incoherent mode-locking. There are a few scattered references to systems in which coherent injection mode-locking played a role [5], [6], but this regime has not been investigated in detail. In our work, we are focusing specifically on this coherent locking regime.

The motivation of this thesis was to pursue a potential method of producing a clock signal which is not only synchronized but also coherent with the data signal. This type of clock signal is at the same optical wavelength as that of the data. A coherent clock signal may be used in homodyne detection systems, which can

theoretically achieve a 3 dB noise figure improvement over optically amplified detection schemes commonly used today. However, coherent injection locking requires precise alignment of the optical wavelength, and is therefore often considered much more difficult to achieve than incoherent mode-locking [13]. A coherent clock recovery scheme requires a method for controlling both the repetition rate and the optical spectrum of the laser output. Our goal is to obtain a better understanding of how monolithic mode-locked lasers work, in order to better control the repetition rate, optical spectrum, and pulse shape produced by these lasers.

In our experiment, a clean train of pulses from an external laser was injected into a monolithic mode-locked laser. We determined the regime where coherent injection locking occurred and characterized the output of the laser.

The thesis begins by discussing how an optical pulse becomes distorted in time and spectrum as it travels through a single pass semiconductor optical amplifier (SOA). The theory has been extensively studied [10], and is reviewed in Chapter 2. The relevant equations describe the effect of amplifier nonlinearities, and are useful for any application involving pulse propagation through an SOA. The technique of filter-assisted optical switching is presented as an exercise to demonstrate understanding of the theory. The same equations are used to simulate the performance of a mode-locked laser where the pulse makes multiple passes through saturable amplifiers and absorbers.

To develop an understanding of pulsed coherent injection locking of a mode-locked laser, it is necessary to study simpler cases of laser operation. The theory of mode-locking in semiconductor lasers is reviewed in Chapter 3. Optically-driven

mode-locking is the method used to control the repetition rate and synchronization of the monolithic laser.

The theory of CW coherent injection locking is reviewed in Chapter 4. Injection locking is the method used to control the optical spectrum of the monolithic laser. It involves establishing optical coherence between the injected signal and the monolithic laser. Injection locking in the pulsed (mode-locked) regime is more complicated and there is no published theoretical treatment. We will develop a simple model to simulate this case.

Both the theories of mode-locking and CW injection locking have been developed for simple laser systems. However, the monolithic laser is a strongly nonlinear device, as understood from the theory of pulse propagation in an SOA. Although the results from these simple theories are not directly applicable for explaining monolithic lasers, they provide a useful framework for discussion.

Chapter 5 describes the experiments we performed to study pulsed coherent injection locking of a mode-locked laser. Experimental data on the RF spectra, optical spectra, and cross-correlation traces are presented and discussed. In particular, the spectrum of the pulsed coherently injection locked laser is much broader than that of the injected laser. This is quite unlike the result of CW coherent injection locking. Also the spectral peak of the injection locked laser shifts significantly as the mode detuning is varied slightly.

In Chapter 6, a discussion of the experimental results is presented. This discussion is based in the framework of the simple theories reviewed earlier. A simple theoretical model is presented based on the equations for pulse propagation in

an SOA. Numerical simulations of situations similar to our experiments were performed, and qualitative agreement was observed.

In Chapter 7, we summarize our results and propose directions for future work.

Chapter 2: Pulse propagation in a single pass semiconductor optical amplifier (SOA)

2.1 Introduction

This chapter examines how optical pulses travel through a semiconductor laser medium. We begin in Section 2.2 by introducing the nonlinear Schrödinger equation which governs electromagnetic pulse propagation in any medium. Then, Section 2.3 considers the properties of semiconductor optical amplifiers (SOAs). In particular, we use the relationship between the carrier density and the susceptibility of the laser medium. The linewidth enhancement factor yields a direct relationship between the gain and the phase response of the laser medium. This allows us to derive equations relating the gain and phase modulation provided by the medium to the pulse intensity that is launched into the medium. The fact that the gain of a semiconductor amplifier depends on the intensity of the input pulse means that it is a nonlinear device. Variation in the intensity of the input to an SOA affects the instantaneous phase of the signal output from the SOA. It will be shown that an input pulse induces a monotonic phase variation from the SOA, which leads to a frequency chirp that is imposed on the pulse.

If a single pulse is launched into the SOA, the phase response will depend on the intensity of that pulse itself. This is called self-phase modulation. If multiple signals are launched into the SOA, the phase response depends on the total intensity of all the input signals. In this way, one signal can be used to affect the phase and

therefore the frequency chirp of a different signal. This is called cross-phase modulation.

The nonlinearity of the gain and phase response of an SOA can be exploited to realize an optical switch. By utilizing the cross-phase modulation effect, a control signal is used to selectively alter the phase of a separate signal. As a result, the altered signal experiences an instantaneous frequency chirp which causes it to shift in spectrum. The shifted pulses can be selected using a band-pass filter. The operating principle, experimental setup and results, and theoretical modeling of this switch are presented in Section 2.4.

The equations relating the gain and phase response of a semiconductor amplifier to the input intensity are also important for studying pulsed coherent injection locking of a mode-locked laser. In Chapter 6, a simple theoretical model of the pulsed injection system is presented. This model is based on the equations developed in this chapter, and treats the mode-locked laser as a series of lumped components. The saturable components are modeled as nonlinear devices which experience self-phase modulation.

2.2 Nonlinear pulse propagation in single mode optical waveguides

All the experimental work we conducted used single mode optical waveguide structures. This section reviews the theory of nonlinear pulse propagation in such structures. We begin the analysis by introducing the wave equation which governs electromagnetic wave propagation in a source-free medium

$$\nabla^2 E - \mu_0 \frac{\partial^2 D}{\partial t^2} = 0 \quad (2.1)$$

Here, D is the electric displacement field, μ_0 is the permeability of free space, and the Laplacian operator ∇^2 applies to the spatial dimensions x , y , and z . Eq. (2.1) assumes that there is no free current density flowing in the medium, and no free charge density, so that $\bar{J} = 0$ and $\rho = 0$. This general expression represents a three dimensional problem which describes electromagnetic fields that vary in x , y , and z . In addition, the waves may consist of any number of frequency components.

For now, let us consider a monochromatic wave with frequency ω_0 . In the frequency domain, the electric and displacement fields are related by the frequency-dependent dielectric constant

$$\tilde{D}(x, y, z, \omega_0) = \varepsilon(x, y, z, \omega_0) \tilde{E}(x, y, z, \omega_0) \quad (2.2)$$

It must be stressed that ε is in general a function of x , y , and z , and a slowly varying function of ω .

We now consider a solution of the electric field in the form of

$$E(x, y, z, t) = F(x, y) A e^{-j(\beta_0 z - \omega_0 t)} + c.c. \quad (2.3)$$

Eq. (2.3) represents a wave propagating in the z direction. It will be shown that F represents the transverse waveguide mode, A is the amplitude of the wave, and β_0 is the propagation constant. For now, since we assumed a monochromatic wave, the amplitude A is a constant with respect to z . Only certain functions $F(x, y)$ will satisfy the wave equation, Eq. (2.1). Those allowed functions are each associated with an specific value of β_0 . By substituting Eq. (2.3) into Eq. (2.1), and using the

relation (2.2), we arrive at an equation which yields the relationship between the allowed forms of $F(x, y)$ and values of β_0

$$\frac{\partial^2 F}{\partial x^2} + \frac{\partial^2 F}{\partial y^2} + (\omega^2 \mu_0 \varepsilon(x, y, z, \omega_0) - \beta_0^2) F = 0 \quad (2.4)$$

Note that in general, the $\partial^2 D / \partial t^2$ term in Eq. (2.1) yields terms that include the first and second time derivatives of ε . However, we neglect the time dependence of ε in the assumption that it is a slowly varying function of ω . In Eq. (2.4), the solutions $F(x, y)$ are eigenfunctions and the corresponding values of β_0 are eigenvalues. If the distribution of $\varepsilon(x, y, z, \omega_0)$ is known for a given ω_0 , Eq. (2.4) can be solved for the eigenfunctions and eigenvalues, assuming any bound solutions exist. All the waveguide structures we use in our experiments are designed such that only one form of $F(x, y)$ exists as a bound solution. Such a waveguide is called a single-mode waveguide, and $F(x, y)$ is the transverse waveguide mode. This mode propagates in the z direction according to its propagation constant β_0 . We introduce the definition of the effective index of refraction n_{eff} as

$$\beta_0 \equiv \frac{n_{eff}(\omega_0) \omega_0}{c} \quad (2.5)$$

Next, we relax the restriction that the electric field is monochromatic. This is necessary to consider the case of pulsed light. In this case, the electric field E contains many frequency components, and the amplitude A is no longer a constant with respect to z . In this case, the time-domain representations of the electric and

displacement fields $E(x, y, z, t)$ and $D(x, y, z, t)$, and of the amplitude $A(z, t)$, are related to the frequency-domain representations by the Fourier transform, as in [7]

$$E(x, y, z, t) = \int_{-\infty}^{\infty} \tilde{E}(x, y, z, \omega) \exp(j\omega t) \frac{d\omega}{2\pi} \quad (2.6)$$

$$D(x, y, z, t) = \int_{-\infty}^{\infty} \tilde{D}(x, y, z, \omega) \exp(j\omega t) \frac{d\omega}{2\pi} \quad (2.7)$$

$$A(z, t) = \int_{-\infty}^{\infty} \tilde{A}(z, \omega - \omega_0) \exp[j(\omega - \omega_0)t] \frac{d\omega}{2\pi} \quad (2.8)$$

Strictly speaking, the eigenvalue equation of Eq. (2.4) must be solved for each frequency component present. However, for pulsed light, we consider the case that the spread of frequency components is centered around the value ω_0 . We also assume that the spread is narrow enough such that the form of $F(x, y)$ is the same for each of the frequencies present. With this assumption, the value of $\varepsilon(x, y, z, \omega_0)$ that strictly pertains only to the ω_0 component, is assumed to apply to the entire wave. By introducing Eq. (2.8) into Eq. (2.3), and comparing the result to the form of Eq. (2.6), we see that

$$\tilde{E}(x, y, z, \omega) = F(x, y) \tilde{A}(z, \omega - \omega_0) e^{-j\beta_0 z} \quad (2.9)$$

Using the form of Eq. (2.9), along with the relation of Eq. (2.2), we can once again solve Eq. (2.1) to arrive at an equation given by

$$-j2\beta_0 \frac{\partial \tilde{A}(z, \omega - \omega_0)}{\partial z} + (\beta^2 - \beta_0^2) \tilde{A}(z, \omega - \omega_0) = 0 \quad (2.10)$$

Again, we have neglected any time dependence of ε . Also, we have made the assumption that A is a slowly varying envelope, and therefore we have neglected the

term that contains the second derivative of \tilde{A} with respect to z . We recognize the quantity β as

$$\beta = \frac{\omega}{c} \sqrt{\frac{\epsilon(\omega)}{\epsilon_0}} \quad (2.11)$$

Eq. (2.10) governs the propagation of the signal envelope \tilde{A} . This is the important equation for the purpose of analyzing the semiconductor optical amplifier.

The quantity β is, in general, a function of frequency. Recall that we assumed that the envelope signal $\tilde{A}(z, \omega)$ consists primarily of frequency components near some center frequency ω_0 . It follows that the values of β under consideration will not differ much from β_0 , the value of the propagation constant at ω_0 . Therefore, Eq. (2.10) can be approximated as

$$\frac{\partial \tilde{A}(z, \omega - \omega_0)}{\partial z} + j(\beta - \beta_0) \tilde{A}(z, \omega - \omega_0) = 0 \quad (2.12)$$

We approximate the quantity β with a second order Taylor series expansion [8]

$$\beta = \beta_0 + \Delta\beta_{NL} + \beta' \cdot (\omega - \omega_0) + \frac{1}{2} \beta'' \cdot (\omega - \omega_0)^2 \quad (2.13)$$

where the derivative terms are evaluated at the center frequency ω_0 . The $\Delta\beta_{NL}$ term is due to nonlinear effects related to the susceptibility of the material. The various coefficients in this expansion have the following definitions [9]

$$\beta(\omega_0) = \frac{\omega_0}{v_p(\omega_0)} \equiv \frac{\omega_0}{\text{phase velocity}} \quad (2.14)$$

$$\beta' = \left. \frac{d\beta}{d\omega} \right|_{\omega=\omega_0} = \frac{1}{v_g(\omega_0)} \equiv \frac{1}{\text{group velocity}} \quad (2.15)$$

$$\beta'' = \left. \frac{d^2\beta}{d\omega^2} \right|_{\omega=\omega_0} = \frac{d}{d\omega} \left(\frac{1}{v_g(\omega_0)} \right) \equiv \text{group velocity dispersion} \quad (2.16)$$

Substituting (2.13) into (2.12), we obtain

$$\frac{\partial \tilde{A}}{\partial z} + j\Delta\beta_{NL}\tilde{A} + j\beta' \cdot (\omega - \omega_0) \cdot \tilde{A} + \frac{1}{2} j\beta'' \cdot (\omega - \omega_0)^2 \cdot \tilde{A} = 0 \quad (2.17)$$

Transforming Eq. (2.17) from the frequency domain back to the time domain, we obtain the nonlinear Schrödinger equation

$$\frac{\partial A}{\partial z} + \beta' \frac{\partial A}{\partial t} + j \frac{1}{2} \beta'' \frac{\partial^2 A}{\partial t^2} - j\Delta\beta_{NL}A = 0 \quad (2.18)$$

2.3 Pulse propagation in semiconductor optical amplifiers

In semiconductor waveguides, the gain and index of refraction depend on the carrier density, which is in turn affected by the injection current and optical intensity. For the purpose of deriving effective parameters of the nonlinear coefficients, consider the carrier-density rate equation for semiconductor optical amplifiers (SOAs) is given by [10]

$$\frac{\partial N}{\partial t} = D\nabla^2 N + \frac{I}{qV} - \frac{N}{\tau_c} - \frac{a(N - N_0)}{\hbar\omega_0} |E|^2 \quad (2.19)$$

where N is the carrier density for electrons and holes, D is the diffusion coefficient, I is the injection current, q is the electron charge, V is the active volume, τ_c is the spontaneous carrier lifetime, $\hbar\omega_0$ is the photon energy, a is the gain coefficient, and N_0 is the carrier density at transparency.

We simplify the carrier-density rate equation by neglecting carrier diffusion. This assumption is valid as long as the transverse width w and thickness d of the active region of the SOA are much shorter than the diffusion length, and as long as the amplifier length L is much longer than the diffusion length, which is typically on the order of microns. This is an applicable assumption for the devices used in this thesis. In this regime, the carrier density is nearly constant as a function of the transverse dimensions. We also define the gain as [10]

$$g(N) = \Gamma a \cdot (N - N_0) \quad (2.20)$$

where Γ is a confinement factor which takes into account the effects of the transverse waveguide mode F . This allows us to rewrite Eq. (2.19) in terms of the signal envelope A . The quantity $|A|^2$ is the intensity of the signal. Neglecting the diffusion term, the carrier-density rate equation (2.19) becomes

$$\frac{\partial N}{\partial t} = \frac{I}{qV} - \frac{N}{\tau_c} - \frac{g(N)}{\hbar\omega_0} |A|^2 \quad (2.21)$$

We also define the mode cross-section σ , the saturation energy E_{sat} , the transparency current I_0 , and the unsaturated or small-signal gain g_0 as [10]

$$\sigma = \frac{wd}{\Gamma} \quad (2.22)$$

$$E_{sat} = \frac{\hbar\omega_0\sigma}{a} \quad (2.23)$$

$$I_0 = \frac{qV N_0}{\tau_c} \quad (2.24)$$

$$g_0 = \Gamma a N_0 \left(\frac{I}{I_0} - 1 \right) \quad (2.25)$$

Using these definitions, and renormalizing the intensity by the cross-sectional area of the active region of the SOA, such that $|A|^2$ represents the power of the signal ($|A|^2 \rightarrow |A|^2/wd$), we obtain an equation describing the gain saturation

$$\frac{\partial g}{\partial t} = \frac{g_0 - g}{\tau_c} - \frac{g \cdot |A|^2}{E_{sat}} \quad (2.26)$$

The frequency-dependent dielectric constant in Eq. (2.2) is given by [10]

$$\varepsilon = n_b^2 + \chi \quad (2.27)$$

where the background refractive index n_b depends on the transverse waveguide mode F . The susceptibility χ represents the contribution of the charge carriers, and therefore χ is a function of N . The imaginary part of χ is associated with the gain or loss of the SOA. The real part of χ is associated with the phase shift that a signal experiences in propagating through the SOA. A simple equation is used to model the dependence of χ on N , given by [10]

$$\chi(N) = -\frac{\bar{n}c}{\omega_0}(\alpha + j) \cdot a \cdot (N - N_0) \quad (2.28)$$

where \bar{n} is the effective mode index. The linewidth enhancement factor, or Henry α factor, takes into consideration the change in refractive index due to the charge carriers. Substituting the expression for gain, Eq. (2.20), into the susceptibility, Eq. (2.28), we obtain

$$\chi(N) = -\frac{\bar{n}c}{\omega_0}(\alpha + j) \frac{g}{\Gamma} \quad (2.29)$$

The nonlinear term in the propagation constant (2.13) is related to the susceptibility by [8]

$$\Delta\beta_{NL} = \frac{\omega_0\Gamma}{2nc} \chi \quad (2.30)$$

Using this expression, and neglecting the term containing $\partial^2 A/\partial t^2$ which relates to group velocity dispersion, the pulse propagation equation (2.18) becomes,

$$\frac{\partial A}{\partial z} + \frac{1}{v_g} \frac{\partial A}{\partial t} = j \frac{\omega_0\Gamma}{2nc} \chi A - \frac{1}{2} \alpha_{loss} A \quad (2.31)$$

This is the equation for pulse propagation in an SOA. Here, we include an extra term on the right hand side to account for the unsaturable loss α_{loss} of the material.

Substituting the form of the susceptibility of Eq. (2.29) into the pulse propagation equation, Eq. (2.31), we obtain

$$\frac{\partial A}{\partial z} + \frac{1}{v_g} \frac{\partial A}{\partial t} = \frac{A}{2} [(-j\alpha + 1)g - \alpha_{loss}] \quad (2.32)$$

The gain saturation equation, Eq. (2.26), and the pulse propagation equation, Eq. (2.32), describe the propagation of a signal through an SOA and the interaction of the signal with gain of the SOA. These equations can be further simplified by transforming to a time frame τ that moves with the pulse [10]

$$\tau = t - z/v_g \quad (2.33)$$

In this time frame, the pulse propagation equation becomes

$$\frac{\partial A}{\partial z} = \frac{A}{2} [(-j\alpha + 1)g - \alpha_{loss}] \quad (2.34)$$

The gain saturation equation simply becomes

$$\frac{\partial g}{\partial \tau} = \frac{g_0 - g}{\tau_c} - \frac{g \cdot |A|^2}{E_{sat}} \quad (2.35)$$

The signal envelope A represents the power of the signal. In general, A is a complex-valued function, and can be expressed as a phasor as

$$A = \sqrt{P} \exp(-j\phi) \quad (2.36)$$

where $P(z, \tau)$ is the amplitude and $\phi(z, \tau)$ is the phase. Introducing the notation of Eq. (2.36) into the pulse propagation equation, Eq. (2.34), and separating the real and imaginary terms of the resulting expression, we obtain two equations. The real terms form an equation which describes the change in the amplitude of the signal

$$\frac{\partial P}{\partial z} = (g - \alpha_{loss}) P \quad (2.37)$$

The imaginary terms form an equation which describes the change in the phase

$$\frac{\partial \phi}{\partial z} = \frac{1}{2} \alpha g \quad (2.38)$$

The propagation of a pulse in an SOA is governed by the set of three equations, Eqs. (2.35), (2.37), and (2.38). A further simplification can be made if the unsaturable loss α_{loss} of the SOA is negligible. In this case, Eq. (2.37) can be directly integrated to obtain [10]

$$P_{out}(\tau) = P_{in}(\tau) \cdot \exp[h(\tau)] \quad (2.39)$$

where $h(\tau)$ is the gain at each point of the signal in time, integrated over the length of the SOA. By integrating over the length of the SOA, we are able to find the total

gain imparted by the SOA on each point of the pulse in time. This integrated gain is given by

$$h(\tau) = \int_0^L g(z, \tau) dz \quad (2.40)$$

Similarly, Eq. (2.38) can be directly integrated to obtain

$$\phi_{out}(\tau) = \phi_{in}(\tau) + \frac{1}{2} \alpha \cdot h(\tau) \quad (2.41)$$

Finally, making use of Eqs. (2.37) and (2.39), we can integrate Eq. (2.35) to obtain a differential equation for the gain

$$\frac{\partial h(\tau)}{\partial \tau} = \frac{g_0 L - h(\tau)}{\tau_c} - \frac{P_{in}(\tau)}{E_{sat}} (\exp[h(\tau)] - 1) \quad (2.42)$$

For a given input signal with power $P_{in}(\tau)$, Eq. (2.42) can be solved numerically to calculate the integrated gain $h(\tau)$. Then, Eqs. (2.39) and (2.41), along with the phase of the input signal, $\phi_{in}(\tau)$, can be used to calculate the power and phase of the output signal.

The gain equation, Eq. (2.42), can be solved analytically if the signal pulse width τ_p is much shorter than the carrier lifetime τ_c [10]. In this case, because the pulse duration is so short, the change of the gain is dominated by gain saturation. Gain recovery does not act fast enough to have a substantial effect. Therefore, the first term on the right hand side of the equation, $(g_0 L - h(\tau))/\tau_c$, can be neglected.

We define an exponential gain factor [9]

$$G(\tau) = \exp[h(\tau)] \quad (2.43)$$

Substituting the gain factor, Eq. (2.43), into the gain equation, Eq. (2.42), and neglecting the gain recovery term, we obtain [11]

$$\frac{dG}{G(1-G)} = \frac{P_{in}(\tau)}{E_{sat}} d\tau \quad (2.44)$$

From Eq. (2.44), we see that the time rate of change of the gain is driven by the power of the input signal. Therefore, the gain itself as a function of time depends on the energy in the input signal. To solve for an expression for the gain, we integrate both sides of Eq. (2.44) from $\tau' = \tau_0$ to $\tau' = \tau$, and we obtain

$$\ln\left(\frac{G}{G-1}\right)\Bigg|_{G=G(\tau_0)}^{G(\tau)} = \frac{1}{E_{sat}} \int_{\tau_0}^{\tau} P_{in}(\tau') d\tau \quad (2.45)$$

We define the input energy at time τ as the accumulated energy in the input pulse up to time τ [9]

$$U_{in}(\tau) = \int_{\tau_0}^{\tau} P_{in}(\tau') d\tau \quad (2.46)$$

The starting time τ_0 is simply some point in time far enough before the start of the input signal when the gain is at its fully recovered, unsaturated value. Therefore,

$$G(\tau_0) = G_0 = \exp[h(\tau_0)] = \exp(g_0 L) \quad (2.47)$$

Using the definitions of Eqs. (2.46) and (2.47), the expression for the gain in Eq. (2.45) becomes the Frantz-Nodvik equation [9]

$$G(\tau) = \frac{G_0}{G_0 - (G_0 - 1) \exp[-U_{in}(\tau)/E_{sat}]} \quad (2.48)$$

This analytical solution is useful for modeling the gain variation during a short pulse, and was used in modeling our laser system as described in Chapter 6.

To demonstrate the effect of an SOA on an optical pulse, we numerically solved the differential equation for gain, Eq. (2.42), for the case of a Gaussian input pulse with a pulse width of 2.3 ps FWHM and pulse energy of 0.063 pJ. Typical SOA parameters were used, including a saturation energy of 10 pJ, an unsaturated gain of 32.4 dB, a carrier lifetime τ_c of 200 ps, and a linewidth enhancement factor of 3. Once the solution for the gain is obtained, we used Eq. (2.41) to calculate the phase of the output signal. The result is shown in Figure 2.1.

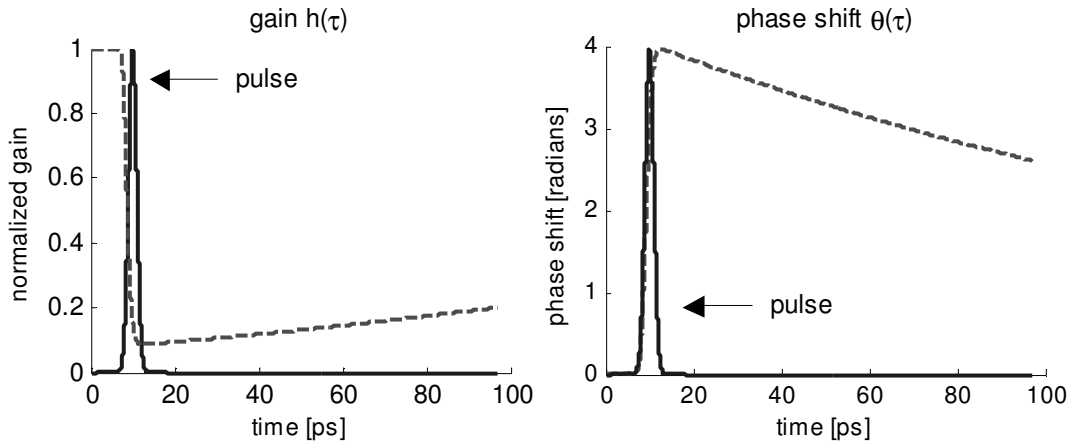


Figure 2.1: The time dependent gain (a) and phase shift (b) of an SOA with 2.7 ps FWHM input pulse.

As shown in Figure 2.1(a) the gain starts from an unsaturated value and is quickly saturated by the input pulse. After the duration of the input pulse, the gain slowly recovers according to the carrier lifetime τ_c . The phase shift associated with gain saturation is shown in Figure 2.1(b). As the gain saturates, a sharp monotonic increase in phase occurs. After the duration of the input pulse, the phase slowly relaxes back to the unsaturated value. In Section 2.4, it will be shown how this phase shift can be exploited to implement an optical switch.

In addition to imposing a phase shift, the SOA also amplifies the pulse. Since the gain is a function of time, the amplification is not uniform across the pulse. Therefore, the pulse shape is modified by the SOA. The normalized input and output pulse shapes are plotted in Figure 2.2. The leading edge of the output pulse is sharper than that of the input Gaussian pulse. This is typical of amplifiers and is due to the fact that the leading edge experiences a larger gain than the trailing edge [10]. The output pulse has a FWHM of 2.36 ps, which is slightly broader than the input pulse. Due to this type of pulse reshaping, the peak of the pulse appears to advance forward in time.

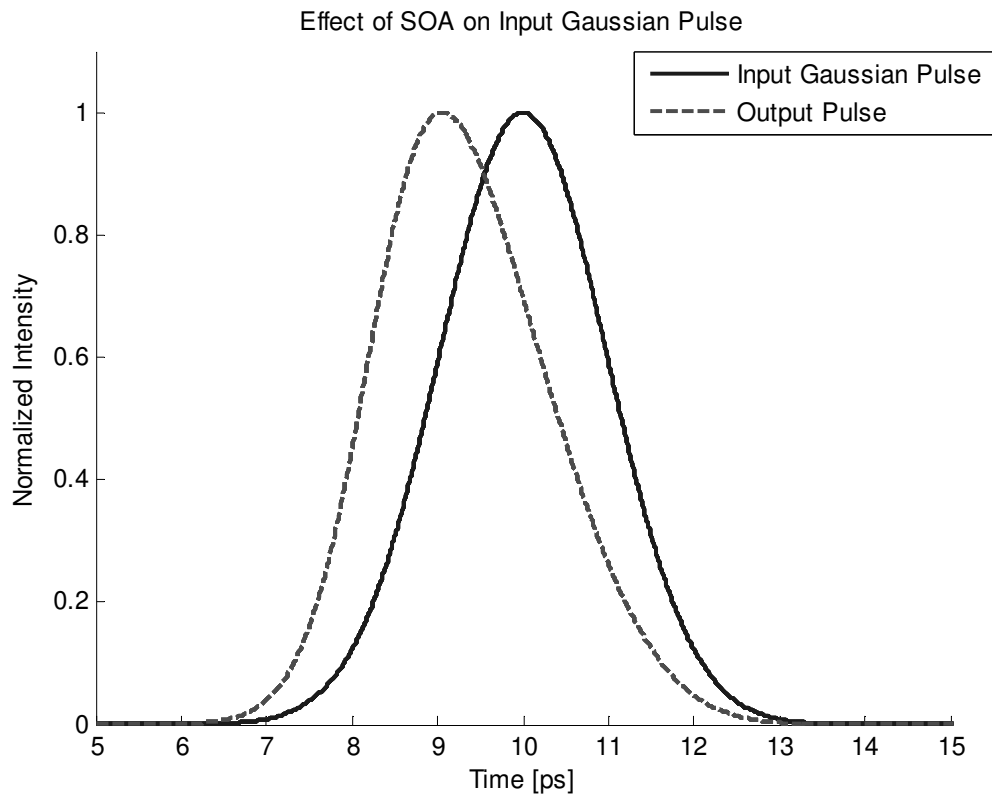


Figure 2.2: Calculated input and output pulse shape from a typical SOA.

2.4 Optical switching using XPM in SOAs

2.4.1 Operating principle

The time-dependent gain saturation and phase shift effects in SOAs described in Section 2.3 can be used to implement an optical switch. The purpose of this device is to select certain designated pulses from a signal. The selection is determined by control pulses. This principle is illustrated in Figure 2.3.

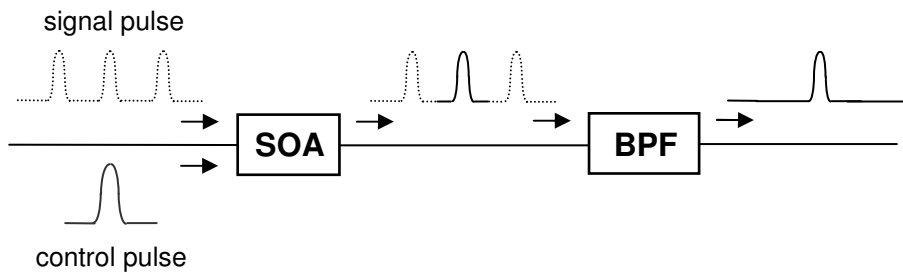


Figure 2.3: Schematic of an optical switch using XPM in an SOA.

In this setup, strong control pulses and weak signal pulses are launched into a properly pumped SOA. The control pulses must contain enough energy to saturate the gain of the SOA according to Eq. (2.42). The signal pulses must be weak enough such that they have negligible effect on the gain saturation. As we know from Eq. (2.41), a change in gain is accompanied by a change in phase. If the control and signal pulse widths are much shorter than the carrier lifetime τ_c , the dominant phase change will be due to the gain saturation, while the slower gain recovery has a negligible effect.

The gain saturation induces a sharp, positive change in phase. This is associated with a red shift in optical wavelength, or equivalently, a positive frequency chirp as defined by

$$\Delta\omega(\tau) = \frac{d\theta}{d\tau} \quad (2.49)$$

If the signal pulse to be selected is aligned in time with a control pulse, the signal pulse also experiences the phase change induced by the control pulse. Since the aligned signal pulse is shifted to a longer wavelength, it can be selected by a band-pass filter (BPF) placed at the output of the SOA. Those signal pulses which are not aligned with a control pulse will be rejected by the BPF since they are not red-shifted.

2.4.2 Experiment on XPM in SOAs

The optical switch setup is experimentally demonstrated using a commercial mode-locked (ML) semiconductor laser for the control pulses and a continuous wave (CW) laser for the signal. The ML laser used is a TMLL-1550 hybrid mode-locked laser from u²t Photonics. It generates pulses with pulse widths of 2.7 ps (FWHM). The tunable repetition rate of the ML is set to 10 GHz and the tunable center wavelength is set to 1550 nm. The CW laser used is a Tunics 1550 wavelength tunable laser from Photonetics. The wavelength of the CW laser is set to 1558.3 nm. The experiment uses an Alcatel 1901 SOA.

In Section 2.4.1, it is explained that only those signal pulses which are aligned in time with a control pulse will experience the phase and wavelength shift induced

by gain saturation. Since we use a CW laser instead of pulses, this experimental setup has a signal that is always “on.” Portions of the CW signal that coincide in time with a control pulse will be red-shifted, while other portions will not. As a result, the narrow spectrum of the CW signal that is launched into the SOA becomes broadened. It develops significant longer-wavelength components which are the red-shifted portions of the signal.

The experimental setup is shown in Figure 2.4. The control pulses from the ML laser are combined with the CW signal in a 50/50 splitter. The combination is launched into the SOA, where the gain saturation and phase shifting occurs. The output of the SOA is sent through a Fiber Bragg grating (FBG) to attenuate the portions of the original CW signal which were not phase-shifted. The available FBG is not tunable, and has a center wavelength of 1558.3 nm. This led to the choice of 1558.3 nm as the input CW wavelength. The signal out of the FBG is sent through a BPF to select the phase-shifted portion of the CW signal. The BPF is centered at 1560.3 nm and has a FWHM of 1.5 nm.

The wavelength-shifted signal captured by the BPF is a measure of the switching window of the SOA. The switching window is the time interval during which input signal pulses will be red-shifted by the SOA. For high-speed communications, short switching windows are required so that the switching operation may be toggled at a higher rate. Due to the uncertainty principle, the wider the BPF is in spectrum, the shorter the switching window will be in time. However, the FWHM of the BPF cannot be made so wide that it captures the unshifted components of the original input signal. Therefore, stronger red-shifting by the SOA

is desired because it allows for the center wavelength of the BPF to be tuned farther from the unshifted wavelength. This, in turn, allows for the use of a wider BPF. According to Eq. (2.41), a larger linewidth enhancement factor α and a larger gain $h(\tau)$ are desirable.

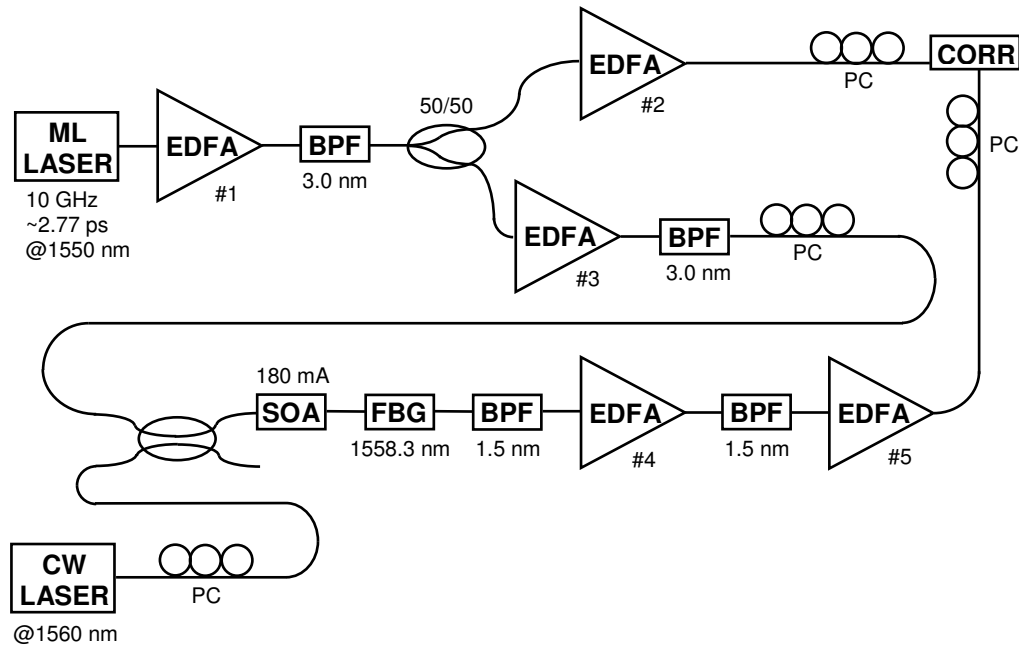


Figure 2.4: Experimental setup for demonstrating the switching window in an SOA. EDFA: Erbium doped fiber amplifier. BPF: Band-pass filter. FBG: Fiber Bragg grating. PC: Polarization controller. CORR: Cross-correlator.

The measured spectra of the CW signal input to the SOA and the resulting output from the SOA are shown in Figure 2.5. As expected, significant red-shifted components are observed in the output spectrum. It should be noted that the plotted curve of the CW signal input has been shifted up by a constant 7.5 dBm in order to place it on the same level as the output curve. This makes it easier to compare the presence of red-shifted components in the output with the lack of red-shifted components in the input.

The peak of the unshifted CW component is also observed to shift to a slightly lower wavelength. This is due to the slow recovery of the gain and phase response in the SOA after the initial fast saturation [8]. In addition, some blue-shifted components are also observed in the output spectrum. This is due to various ultrafast phenomena including carrier heating, spectral hole burning, and two photon absorption [8]. These blue-shifting effects are not important for the switching operation, since the switch relies on selecting the red-shifted components while filtering out the blue-shifted and unshifted components.

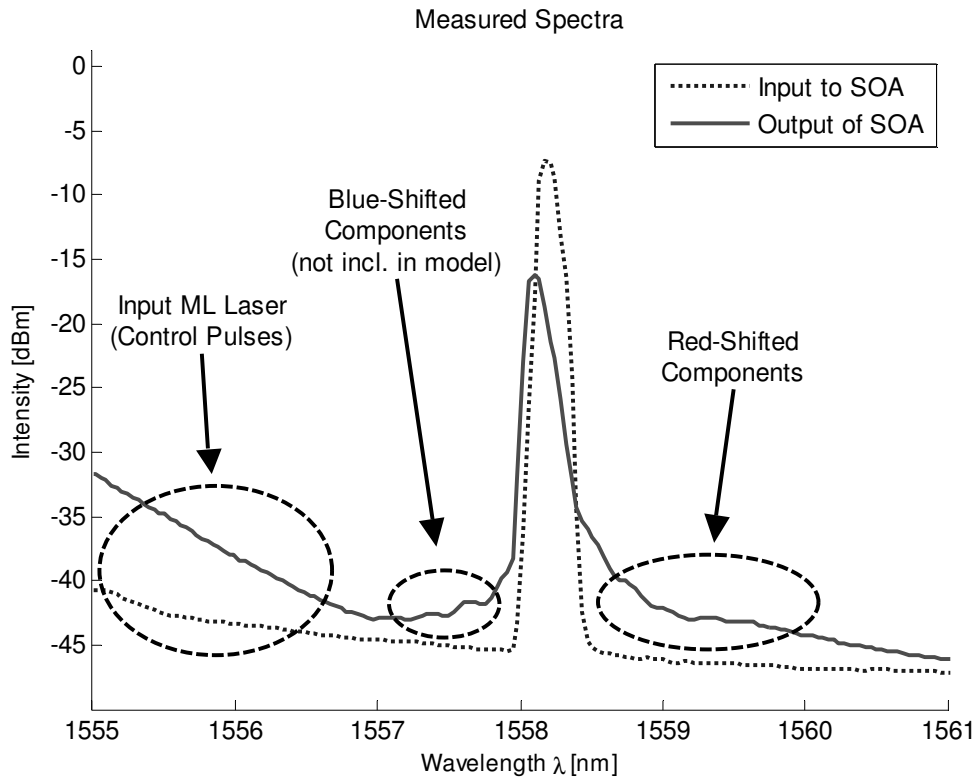


Figure 2.5: Measured spectra of CW signal input to SOA (dotted line) and broadened CW output (solid line). The longer-wavelength broadening is clearly evident. Some shorter-wavelength broadening is also present. The input curve has been shifted up by a constant 7.5 dBm for purpose of comparison.

As shown in Figure 2.4, the ML laser is used for two purposes. First, it is used for the control pulses in the switching operation of the SOA. EDFAs #1 and #3 ensure that the control pulses launched into the SOA are strong enough to saturate the gain of the SOA. Both EDFAs #1 and #3 are followed by a 3.0 nm FWHM BPF to attenuate the amplified spontaneous emission (ASE) generated by those amplifiers. Second, the ML is used as a reference signal for measuring the switching window signal.

The switching window is measured using an FR-103XL cross-correlator from Femtochrome Research, Inc. This type of device is used because the available photodetectors for oscilloscopes are not able to resolve pulses with widths on the order of picoseconds. The cross-correlator (CORR) performs the cross-correlation of two input signals using second harmonic generation (SHG) by a nonlinear crystal. SHG is a nonlinear process which depends strongly on the polarization of the input signals. Therefore, polarization controllers (PC) are placed in the paths of both inputs to the CORR. The CORR also requires relatively high input powers. This creates the need for EDFAs #2, #4, and #5 in Figure 2.4. The BPF at the output of EDFA #4, which has a FWHM of 1.5 nm, serves to further shape the switching window, as well as to attenuate the ASE from EDFA #4, so that this noise is not fed into EDFA #5.

The CORR does not directly measure the switching window. Rather, it gives a time-averaged cross-correlation between the ML pulses and the switching window.

The cross-correlation of two functions is defined as

$$(f * g)(t) = \int f^*(\tau) g(t + \tau) d\tau \quad (2.50)$$

For functions that are even and real, the cross-correlation is equivalent to convolution. It can be thought of as sliding one function past another by adjusting the delay between the two functions, while integrating the product of the two for each value of delay. The CORR uses a mechanical rotating mirror assembly to continuously sweep the physical path length, and therefore the delay, of one of the input signals. The path length of the other input signal is fixed. The SHG product generated by the nonlinear crystal depends on the intensities of the two input signals, so nonlinear crystal physically performs the integration in Eq. (2.50). The rate of rotation of the mirror assembly is on the millisecond scale, so the correlation trace generated by the CORR is easily detected by a standard oscilloscope.

An important case to consider is that of the correlation between two Gaussian curves. Let $f(x) = \exp\left[-(x/a)^2 \cdot 4\ln(2)\right]$ and $g(x) = \exp\left[-(x/b)^2 \cdot 4\ln(2)\right]$, which are Gaussian curves with FWHM equal to a and b , respectively. The cross-correlation between these two functions is another Gaussian curve

$$(f * g)(x) = \exp\left[-\left(x^2/(a^2 + b^2)\right) \cdot 4\ln(2)\right] \quad (2.51)$$

The cross-correlation has a FWHM equal to c , given by

$$c = \sqrt{a^2 + b^2} \quad (2.52)$$

If $f(x)$ is much narrower than $g(x)$, which is the limit that $a \ll b$, the correlation will be a reproduction of $g(x)$. For functions which are not Gaussian, or which are Gaussian but possess phase variation, Eq. (2.52) will not be exactly correct. Still, as long as the input functions are fairly pulse-like, the equation will yield some measure of the relationship between the FWHM widths of the input and output functions.

Ideally, if Gaussian pulses that are significantly narrower than the switching window were available, the CORR could be used to directly measure the switching window. In practice, the pulses generated by the ML laser do not satisfy this condition. The ML laser pulses were measured by sending the ML signal through a 50/50 splitter, and then taking the correlation of the two split paths, as shown in Figure 2.6. The cross-correlation of a function with itself is also called auto-correlation. Setting $a = b$ in Eq. (2.52), the auto-correlation of a Gaussian pulse has FWHM equal to

$$c = a\sqrt{2} \quad (2.53)$$

The measured auto-correlation trace of the ML laser is plotted in Figure 2.7, and is compared to a Gaussian curve of FWHM 3.82 ps. It is clear that the auto-correlation of the ML pulse is very nearly Gaussian in shape, with a FWHM of about 3.82 ps. Using Eq. (2.53), and assuming that the ML pulse is Gaussian with negligible phase variation, the FWHM of the ML pulse itself is about 2.7 ps. This is not much narrower than the switching window. Still, since the ML laser FWHM is known, Eq. (2.52) can be used to estimate the FWHM of the switching window.

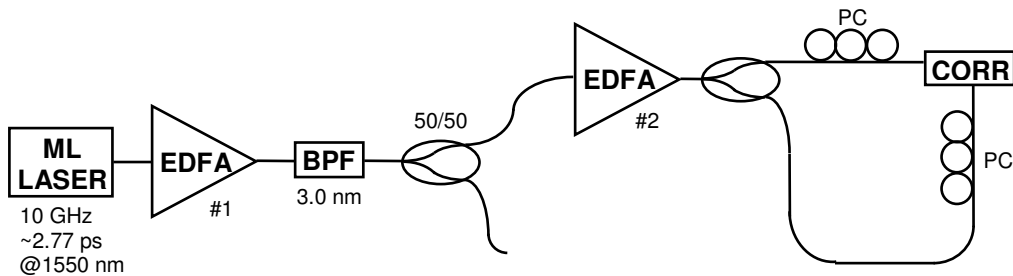


Figure 2.6: Experimental setup for measuring auto-correlation of ML pulses.

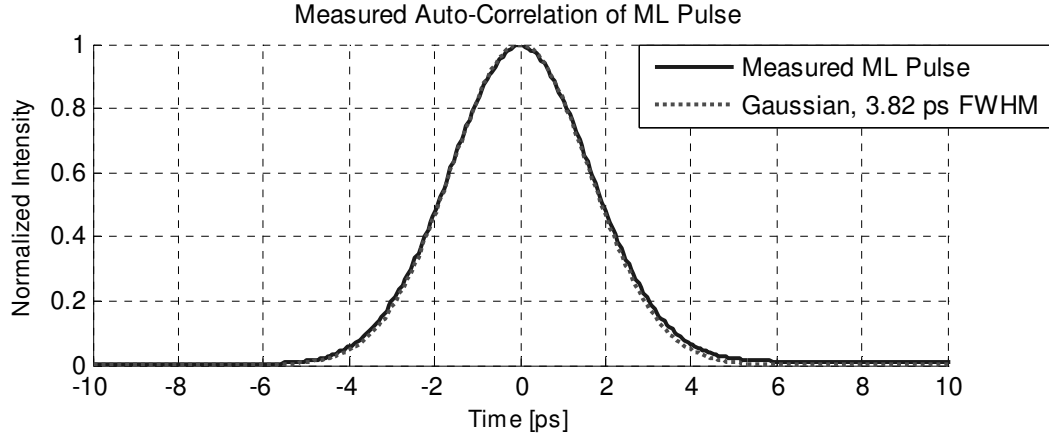


Figure 2.7: Measured auto-correlation of ML pulse. Data (solid line) is plotted along with simulated 3.82ps FWHM Gaussian pulse (dotted line).

The experimental setup in Figure 2.4 is used to measure the switching window by cross-correlating the switching signal with the ML laser pulses. The result is shown in Figure 2.8 along with a simulated Gaussian curve of FWHM 5.4 ps. The cross-correlation trace closely matches the Gaussian curve. If the switching window is assumed to be Gaussian with negligible phase variation, the FWHM of the switching window can be found using Eq. (2.52) and the experimentally obtained FWHM of the ML laser, 2.7 ps. This yields a result of 4.7 ps for the FWHM of the switching window.

Close observation of Figure 2.8 shows that the cross-correlation trace of the switching window features a pedestal that starts at 20 ps and ends at 120 ps. This is a normal feature of the cross-correlator, and is related to the fact that a 10 GHz ML laser pulse train is being correlated with a signal that consists of both the switching window, which repeats at a 10 GHz rate, as well as background energy that is not at 10 GHz. The sources of the background energy include the ASE from the SOA and the various amplifiers shown in Figure 2.4, EDFAs #2, #4, and #5. In Figure 2.9, the dotted curve shows a flat pedestal that is measured when the control pulse is

deactivated by turning off EDFA #3. With no control pulse launched into the SOA, the CW signal does not experience the red-shifted broadening, and the result is simply a correlation of ML laser pulses with ASE from the various amplifiers in the setup. However, the pedestal in the cross-correlation trace of Figure 2.8 is not flat. This was experimentally determined to be a result of the control pulses, as shown in the solid curve in Figure 2.9. When the CW signal is turned off, only the control pulses are launched into the SOA. Despite the two BPFs placed after the SOA, some energy at 10 GHz still reaches the CORR. The correlation between this energy with the ML pulses produces an uneven step in the pedestal. This step is the uneven pedestal in the cross-correlation trace of the switching window.

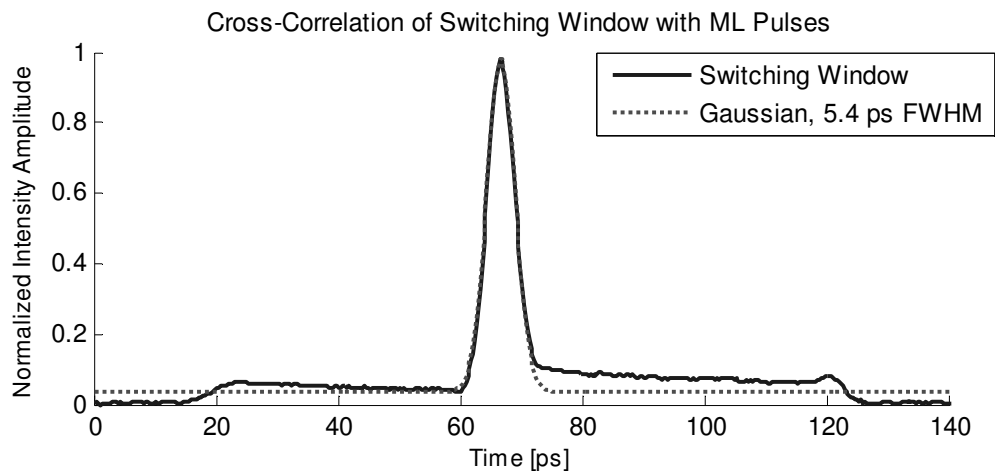


Figure 2.8: Cross-correlation measurement of switching window (solid line) with simulated Gaussian (dotted line) of 5.4 ps FWHM for comparison.

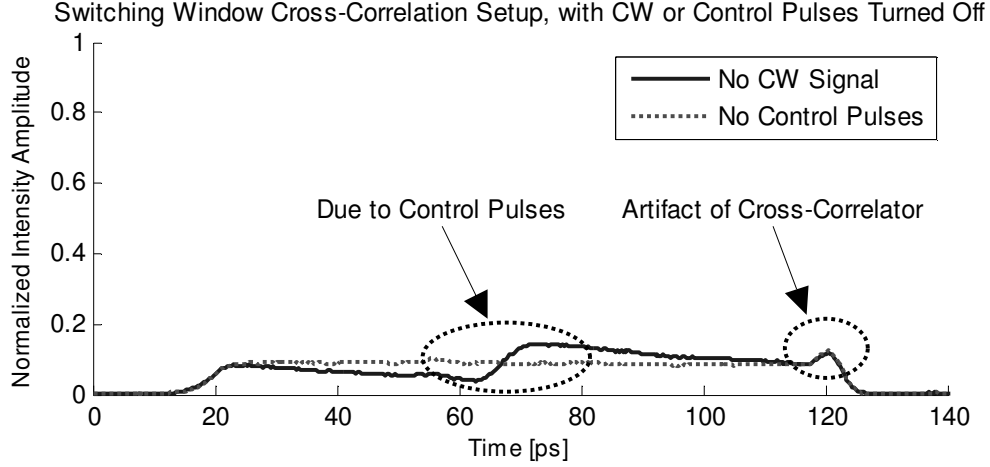


Figure 2.9: Cross-correlation measurement as in Figure 2.7, but with only control pulses (solid line) or only CW signal (dotted line).

2.4.3 Modeling of XPM in SOAs

A model was developed to simulate the switching operation using the equations presented in Section 2.3 and shown in Figure 2.4. The model begins at the input of the SOA. The signal launched into the SOA consists of a Gaussian pulse and a CW signal. The Gaussian pulse represents the ML laser control pulse, and is generated in the model with no phase variation. Therefore, the calculations are performed on a shifted frequency domain that is centered around the optical frequency ω_p of the ML laser. The CW signal, which is taken to have an optical frequency ω_{CW} , is generated in the model as a constant amplitude electric field with a phase that varies linearly as $\exp(-i(\omega_{CW} - \omega_p)t)$. This ensures that the CW signal is offset from the Gaussian pulse in frequency space by the correct amount. Using the

values in the experiment, ω_p corresponds to 1550 nm and ω_{CW} corresponds to 1558.3 nm.

The model numerically solves Eq. (2.42) for the integrated gain $h(\tau)$, using the generated Gaussian pulse and CW signal as the input. The output of the SOA is calculated simply by applying Eqs. (2.39) and (2.41) to the input,

$$E_{out}(\tau) = E_{in}(\tau) \cdot \exp(h(\tau)/2) \cdot \exp(i\alpha_H h(\tau)/2) \quad (2.54)$$

where $E_{in}(\tau)$ is the sum of the input Gaussian pulse and CW signal and α_H is the linewidth enhancement factor.

The calculated electric field output of the SOA is then transformed to the frequency domain. The resulting spectrum is plotted in Figure 2.10 along with the spectrum of the generated input. The simulation shows good qualitative agreement with the experimental results shown in Figure 2.5. Significant red-shifted components are observed in the output spectrum, similar to the experimental measurement. The shift of the CW peak to a slightly shorter wavelength and the presence of weaker blue-shifted components are also consistent with the experiment.

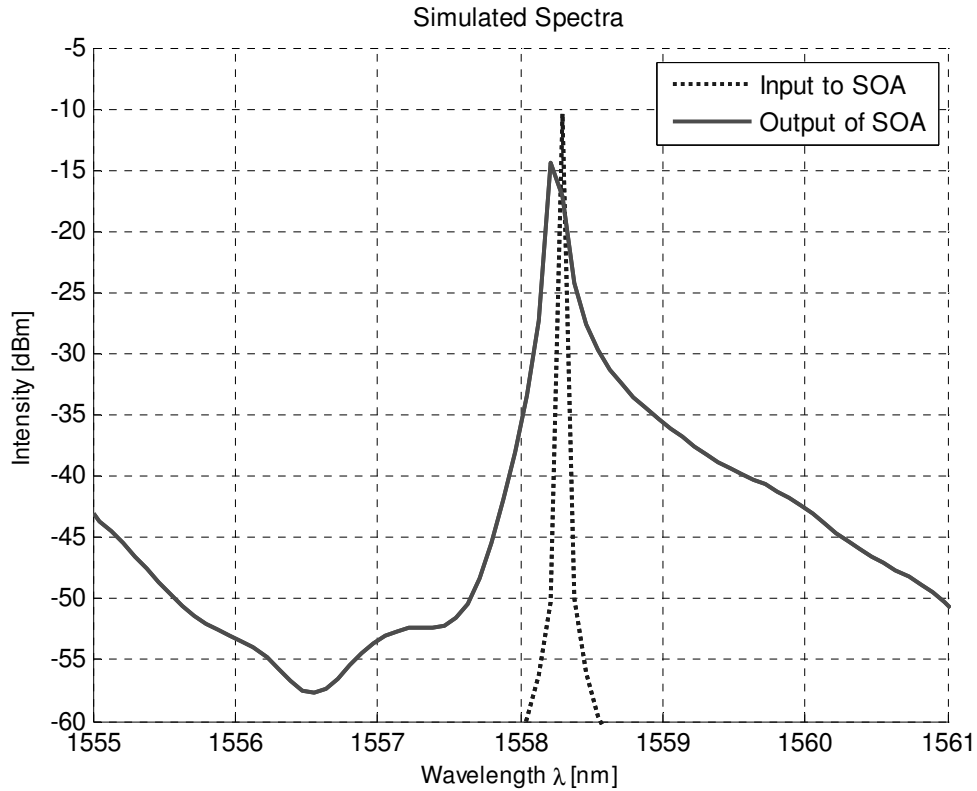


Figure 2.10: Simulated spectra of CW signal input to SOA (dashed line) and broadened CW output (solid line). The longer-wavelength broadening is clearly evident.

The output spectrum is then multiplied by the transmission functions of two BPFs and one FBG, to simulate the experiment in Figure 2.4. The model assumes that the BPFs are Gaussian filters with no phase variation. To demonstrate the appropriateness of this approximation, the measured transmission functions of the two BPFs are shown in Figure 2.11 along with the Gaussian filters used in the model. The simulated Gaussian filters have peak transmission and FWHM values chosen to match the values of the measured BPFs. The FBG is modeled as a fiber with a sinusoidally modulated refractive index [12]. The measured and simulated transmission functions of the FBG are shown in Figure 2.12.

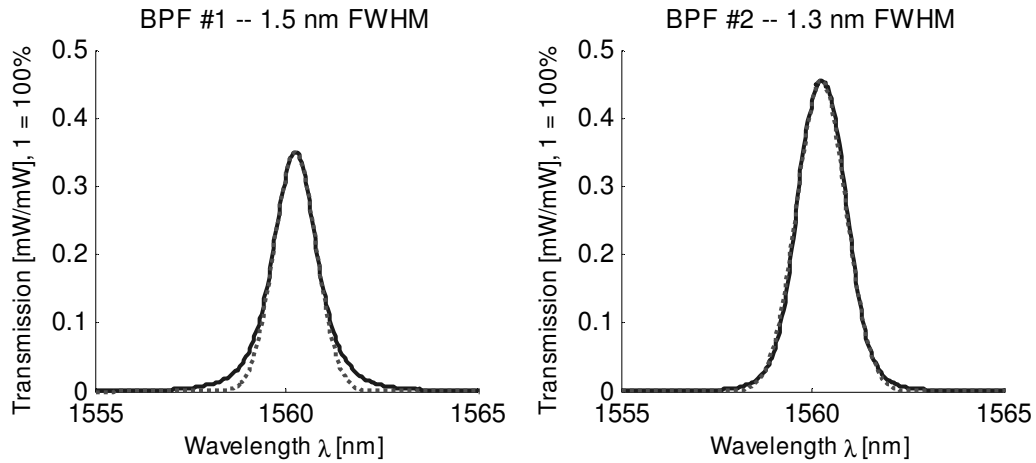


Figure 2.11: Measured transmission functions (solid lines) of the two BPFs placed after the SOA in the switching experiment. The model uses Gaussian curves (dotted lines) with peak transmission and FWHM chosen to match the measured transmission functions.

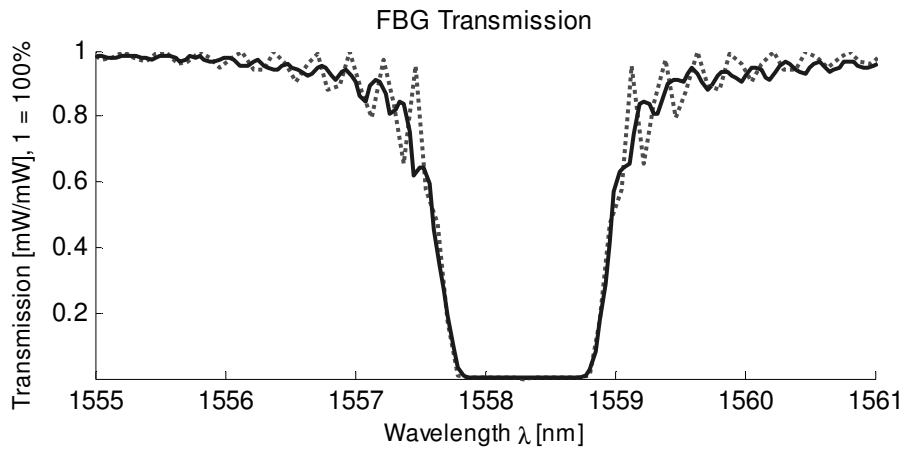


Figure 2.12: Measured (solid line) and simulated (dotted line) transmission functions of the FBG placed after the SOA in the switching experiment.

The spectrum after the BPFs and FBG is then transformed back to the time domain. The result is the simulated switching window, and is shown in Figure 2.13. The simulated switching window has a FWHM of 4.3 ps, which is slightly less than the measured result of 4.7 ps that was shown in Figure 2.8. The discrepancy may arise from several factors. In the experiment, the switching window is measured by a cross-correlation of the actual switching window signal with the ML laser pulses.

The FWHM of the switching window is calculated from the FWHM of the measured cross-correlation trace by (2.52), which is valid for unchirped Gaussian pulses. Since the switching window signal is not exactly Gaussian in shape, and certainly has some phase variation, the result of 4.7 ps is an estimate. In addition, the simulation makes several simplifying assumptions. The BPFs are modeled as having perfectly Gaussian intensity transmission profiles. As illustrated in Figure 2.11, the actual transmission shapes are not exactly Gaussian. Also, the actual BPFs may impose a phase variation on the transmitted signal. In addition, the simulation does not take into account any effect of the various EDFAs used in the experiment. It assumes that the gain profiles of the EDFAs are flat and have no phase variation over the spectral region of interest.

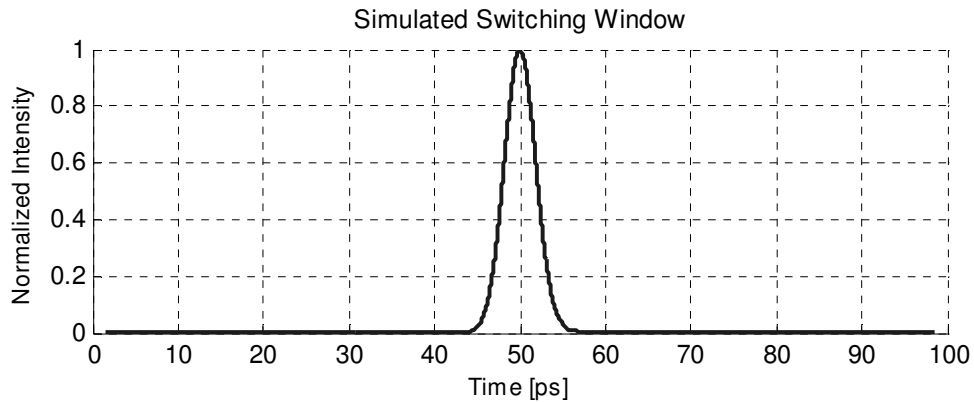


Figure 2.13: Simulated switching window, with FWHM equal to 4.3 ps. Compare to experimental result, with FWHM about 4.7 ps (Figure 2.8).

Chapter 3: Semiconductor Monolithic Mode-locked Lasers

3.1 Introduction to Mode-locking Theory

As mentioned in Chapter 1, mode-locking is a method for producing a pulsed laser and for controlling the repetition frequency of the pulses. In general, mode-locking (ML) is a regime of laser operation in which the laser generates light that is characterized by several sharp and equally spaced frequency structures with a fixed phase relationship [13]. In a laser which consists of a linear cavity, the frequency structures are called axial or longitudinal modes. This refers to the fact that only a certain discrete set of frequencies, or wavelengths, satisfies the round trip phase shift condition for steady state operation [9]. This type of spectrum corresponds to a periodic signal in time and vice versa. The repetition rate is determined by the length of the laser cavity, and is equal to the spacing of the axial modes, as given by

$$\frac{2\pi}{T} = \frac{v_g}{2L} = \Delta\omega_{ax} \quad (3.1)$$

where T is the period of repetition, v_g is the group velocity inside the cavity, L is the length of the cavity, and $\Delta\omega_{ax}$ is the spacing of the axial modes. The spectral width $\delta\omega_q$ of each axial mode depends on the number of periods n_{period} the signal exists in time, and is of the order $\delta\omega_q \approx \Delta\omega_{ax}/n_{period}$ [9]. In steady state, the signal is assumed to exist for an infinite number of periods. This corresponds to infinitesimally sharp axial modes, or a discrete spectrum.

As just described, mode-locking involves the presence of many axial modes with a fixed phase relationship. Each axial mode is specified by its amplitude and optical frequency. Accordingly, the electric field corresponding to a single axial mode can be written in phasor notation as [9]

$$E_1(t) = \text{Re} \left\{ A_1 e^{j(\omega_1 t + \phi_1)} \right\} \quad (3.2)$$

where A_1 is the amplitude of the mode, ω_1 is the optical frequency of the mode, and ϕ_1 is the phase of the mode. These three quantities are constant for a laser in steady state operation. A signal which consists of many axial modes can then be written as a sum of the electric fields of each of the modes. For the special case of a signal that consists of N axial modes of equal amplitudes and phases, the electric field is

$$E(t) = \sum_{n=0}^{N-1} A_0 e^{j(\omega_0 + n\Delta\omega_{ax})t} e^{j\phi_0} = A_0 \frac{e^{jN\Delta\omega_{ax}t} - 1}{e^{j\Delta\omega_{ax}t} - 1} e^{j\omega_0 t} e^{j\phi_0} \quad (3.3)$$

where A_0 is the constant amplitude of the modes and ϕ_0 is the constant phase of the modes. Here, the lowest frequency mode has an optical frequency of ω_0 , and the modes are equally spaced by $\Delta\omega_{ax}$. The intensity of this signal is given by

$$I(t) = |E(t)|^2 = A_0^2 \frac{1 - \cos(N\Delta\omega_{ax}t)}{1 - \cos(\Delta\omega_{ax}t)} = A_0^2 \frac{\sin^2(N\Delta\omega_{ax}t/2)}{\sin^2(\Delta\omega_{ax}t/2)} \quad (3.4)$$

Since the phases of each of the modes are the same, the value of the absolute phase ϕ_0 is unimportant.

Simulated signals with modes of equal amplitudes and phases with are shown in Figure 3.1 (a), (b), and (c) for the cases of 4, 5, and 8 modes, respectively. For each case, two periods of the signal in time are shown, along with the corresponding discrete spectrum. It is clear that when the mode amplitudes and phases are equal, the

signal in time takes the form of a single dominant pulse per period, with much weaker subsidiary peaks. The FWHM pulse width of the signal in time is given roughly by $\tau_p \approx T/N$ [9]. This inverse relationship between pulse width and the number of modes is qualitatively observed in Figure 3.1 (a), (b), and (c), as the pulse width clearly decreases as the number of modes is increased from 4 to 8. This represents an idealized case of mode-locking.

In general, the spectrum of the signal is specified by the number of axial modes present, the amplitude distribution of the modes, and the phase relationship between the modes. Eq. (3.4) applies to the case of a rectangular amplitude distribution and constant phases among the modes, and the plots in Figure 3.1 (a), (b), and (c) present the results for different numbers of modes. It was seen that the signal pulse width decreases with an increasing number of modes. Other cases can easily be explored by numerically adding the electric fields of modes which do not have equal amplitudes or phases, with each mode specified in the form of Eq. (3.2). A series of calculations reveals that adjusting the amplitude distribution while keeping the phase constant can clean up the signal shape, and that the crucial requirement for pulse train formation is the constant phase.

The effect of the mode amplitude distribution is examined by calculating the cases of a Gaussian distribution and a random distribution. The case of a Gaussian distribution of mode amplitudes with the phases equal is shown in Figure 3.1 (d). Once again, the signal in time takes the form of a train of pulses, but pulse shape is now Gaussian and there are no subsidiary peaks. This demonstrates that the amplitude distribution can be tailored to suppress the subsidiary peaks, and shows

that mode-locking can indeed be used to generate short optical pulses. In the other case, the results of random amplitude distributions are shown in Figure 3.1 (e) and (f). Here, the phases are still kept constant. Even with such poorly behaved amplitude distributions, the signal still takes the form of a single dominant pulse per period. The random amplitudes simply make the subsidiary peaks slightly larger. This case is calculated and presented twice simply to demonstrate that the random nature of the mode amplitudes is linked to the amplitudes of the subsidiary peaks.

The critical requirement for all of the cases just examined is the constant phase between the axial modes. If this restriction is relaxed, the signal no longer takes the form of a pulse train. Figure 3.1 (g) and (h) show two cases of rectangular amplitude distributions with different random phases. The signal in time is still periodic, but there is no single dominant pulse per period. Even when the amplitude distribution is changed to a Gaussian, which helped to clean up the pulses for the case of equal phases, the resulting signal in time still fails to take the form of a pulse train. The result is shown in Figure 3.1 (i) and (j).

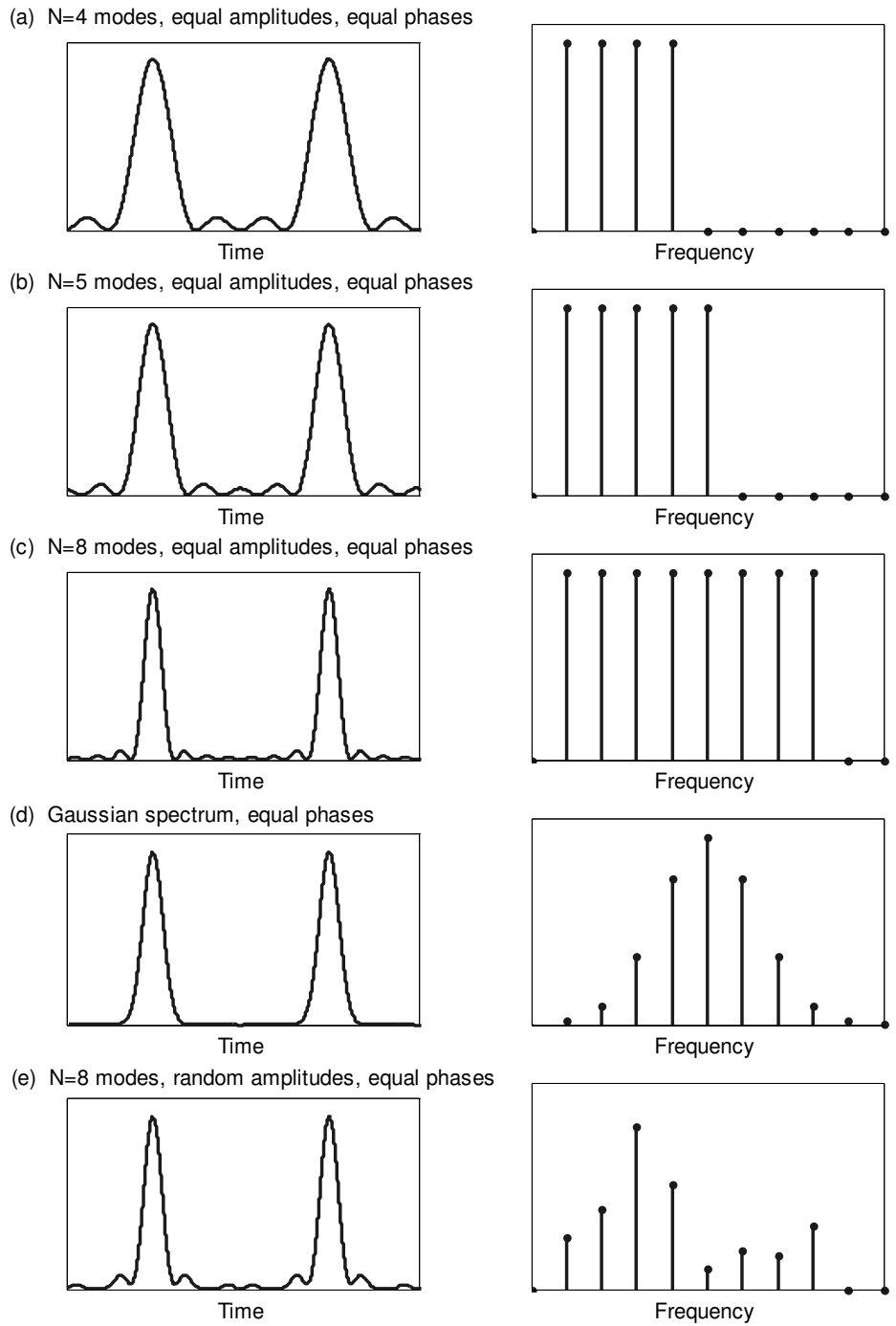


Figure 3.1: Examples of signals in time that correspond to N equally spaced axial modes of different amplitude and phase distributions.

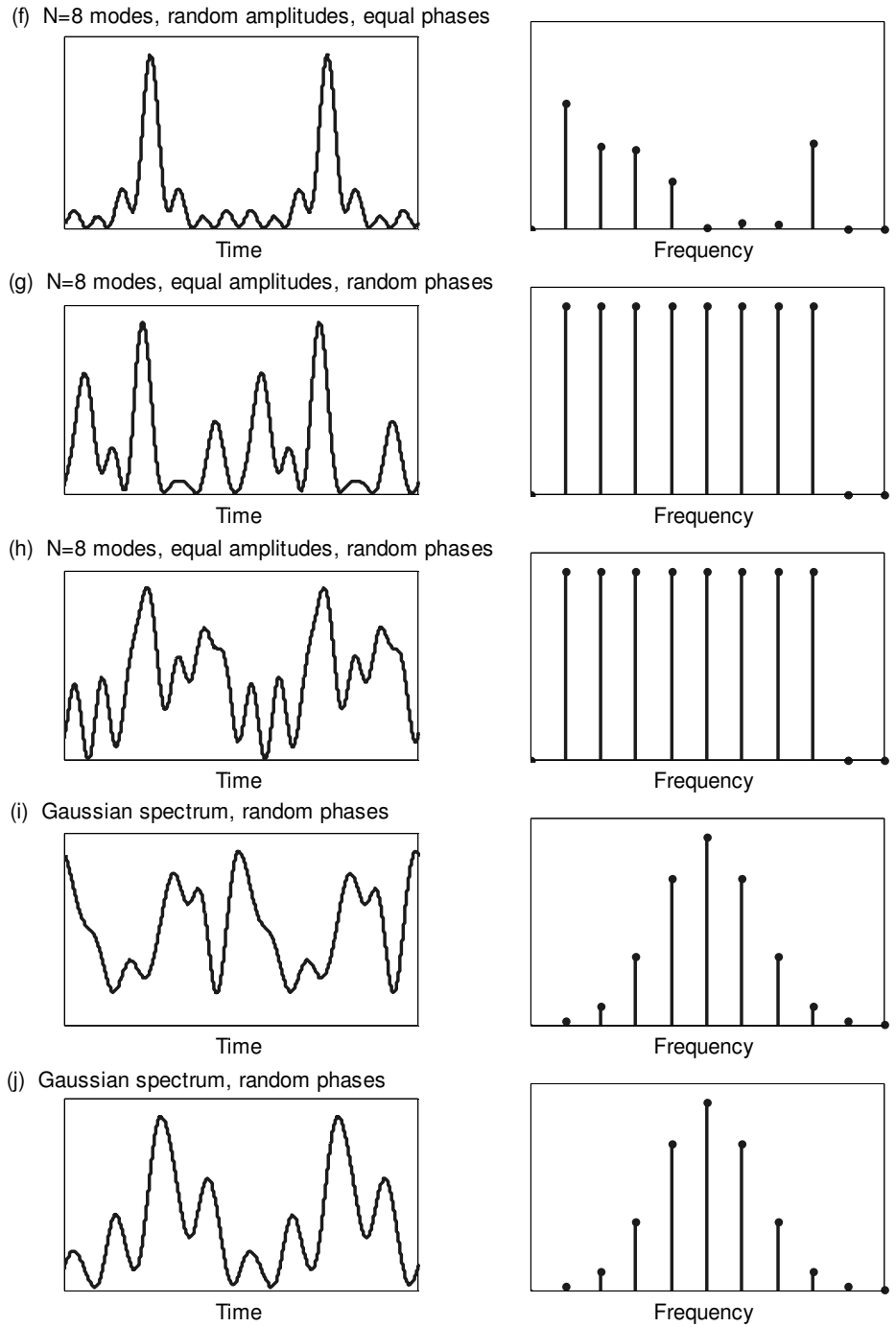


Figure 3.1: Examples of signals in time that correspond to N equally spaced axial modes of different amplitude and phase distributions.

The most common definition of mode-locking refers to the case shown in Figure 3.1 (d), and is characterized by a spectrum of equally spaced frequency modes with a well behaved amplitude distribution and a constant phase across all the modes. This is strictly referred to as amplitude modulation (AM) mode-locking. A less commonly studied case is frequency modulation (FM) mode-locking, in which the phase difference between adjacent modes is π rather than 0 [13]. FM mode-locking can be used to produce either pulse trains, like AM mode-locking, or a very different type of constant amplitude, frequency-swept operation [9]. In this work we focus on AM mode-locking.

3.2 Techniques of Mode-locking

Mode-locking requires a method of generating the type of spectrum described in Section 3.1. This type of operation is achieved in one of three ways. In active mode-locking, one of the laser parameters is modulated at the repetition frequency of the laser cavity. In passive mode-locking, a nonlinear device is introduced into the system. In hybrid mode-locking, the active and passive techniques are used together.

Active mode-locking is achieved by modulating one of the laser parameters at a frequency equal to the cavity repetition rate, or an integer multiple n of that rate [9]. Different methods are used to modulate a key parameter such as the laser gain. Implemented correctly, this creates short time windows of net gain during which pulses can build up. If the modulation frequency is exactly or closely equal to the cavity repetition rate, there will be a single time window per round trip in the cavity. In spectrum, this means that each of the axial modes ω_q present in the unmodulated

laser acquires sidebands at frequencies $\omega_n = \omega_q \pm n \omega_m$, where ω_m is the modulation frequency. Since ω_m is chosen to be exactly or very closely equal to $\Delta\omega_{ax}$ or one of its harmonics, these sidebands will fall exactly or very closely on the other axial modes already present in the unmodulated laser. This is illustrated in Figure 3.2, although the detuning between the free-running modes and the sidebands are exaggerated. The sidebands will tend to injection lock the axial modes with which they coincide, as long as their detuning is within a certain range. As will be described in Chapter 4, the injection locking process will lock the phases and optical frequencies of the sidebands and the unmodulated axial modes. Therefore, modulation has the effect of coupling each of the axial modes to one another [9].

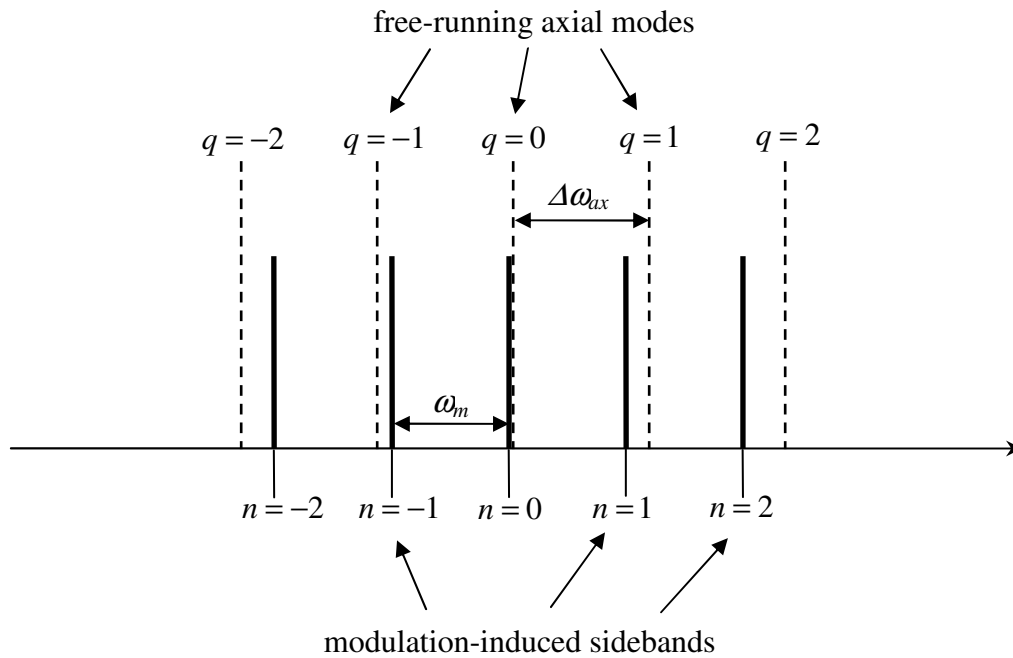


Figure 3.2: Free-running laser axial modes and modulation-induced sidebands.

Passive AM mode-locking is achieved by introducing a nonlinear device in the laser cavity [10]. In the most common configuration, a saturable absorber (SA) is introduced which works together with the saturable gain of the laser to produce short pulses. The type of saturable absorbers used in passive mode-locked lasers are slow saturable absorbers [14], which are characterized by a recovery time τ_c much longer than the typical signal pulse width τ_p [15]. Therefore, these saturable absorbers act much like the saturable amplifiers described in Chapter 2. The saturation and recovery dynamics of these saturable absorbers are described by the same gain equations presented in Section 2.3, namely Eqs. (2.39), (2.41), and (2.42), or the approximate gain solution of (2.48). The main distinction between a saturable amplifier and a saturable absorber is the value of the unsaturated gain or absorption G_0 . For an amplifier the value is greater than one and for an absorber the value is less than one. The solution to Eq. (2.42) yields the gain and absorption as functions of time. Passive mode-locking occurs when these functions of time add to form a single short window of net gain per round trip in the laser cavity during which mode-locked pulses can form.

Passive mode-locking can be described by a self consistent process in time, as illustrated in Figure 3.3 [9]. Initially, before the arrival of a mode-locked pulse, the absorption must be greater than the gain. This is a situation of net loss. As the mode-locked pulse arrives, it must quickly saturate the absorber to create a situation of net gain. Next, the pulse must saturate the amplifier to close the window of net gain. Eventually, both the absorber and the amplifier must recover back to their initial values in order for the process to be self consistent. Mode-locking is achieved by this

process because the peak of the pulse experiences amplification while the leading and trailing edges of the pulse experience loss. On each round trip through the laser cavity, the pulse will be shaped by this interaction between the gain and absorption profiles.

According to this description of passive mode-locking, the saturable absorber must satisfy two requirements. First, the SA must have a lower saturation energy E_{sat} than the saturable amplifier [16]. This is necessary for the proper formation of the net gain window. Second, the SA must have a recovery time τ_c at least as short as that of the saturable amplifier [9]. Otherwise, additional windows of net gain may form during the recovery time.

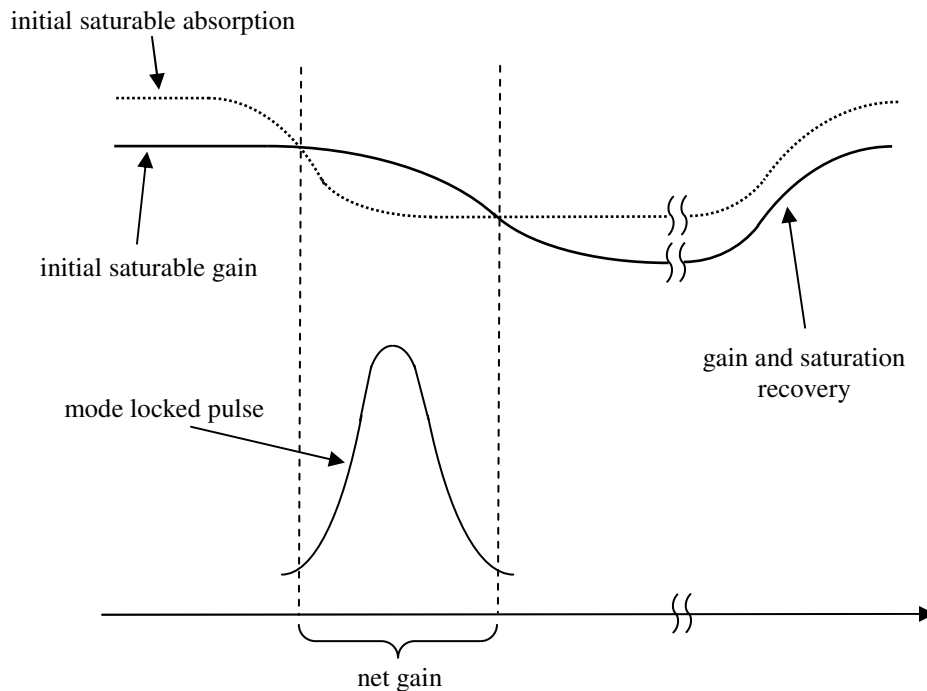


Figure 3.3: Process of passive mode-locking.

3.3 Types of Semiconductor Mode-locked Lasers

Mode-locking with both active and passive techniques has been achieved in a variety of laser types, including Nd:YAG lasers and organic dye lasers. In particular, much research has been devoted to mode-locking in semiconductor diode lasers, since it was first demonstrated by Ho, et al. [17]. Diode lasers are attractive candidates due to their easy fabrication, compact size, integrability into optoelectronic technology, and easy pumping. A good review is given by Avrutin [13]. The two general types of structures that have been developed for mode-locking in semiconductor lasers are external cavity lasers and monolithic lasers. The latter are of greater interest and will be discussed in detail. In particular, different types of monolithic constructions including tandem, colliding pulse mode-locked (CPM), self colliding pulse mode-locked (SCPM), ring cavity, and extended cavity.

In the external cavity construction, the signal inside the laser cavity is coupled to a larger external cavity. This may be a resonant air filled cavity or a fiber cavity. This construction allows for easy tuning of the mode-locked pulse repetition rate by adjusting the external cavity length. It also permits the introduction of diffraction gratings to control the laser spectrum. External cavity lasers also exhibit lower timing jitter than monolithic lasers [18]. However, the additional components of this structure outside the semiconductor pose the problem of maintaining mechanical stability. Optical coupling between the semiconductor laser and the external cavity must also be considered. In addition, the maximum repetition rate achievable is limited by the challenges of fabricating shorter external cavities. Repetition rates of up to 20 GHz were achieved in a passive mode-locked external cavity laser,

producing pulses with FWHM from 0.2 to 6 ps [14]. In order to meet the need for higher repetition rates and to realize mechanically simpler designs, it is desirable to eliminate the need for the external cavity.

In the monolithic construction, the mode-locked laser consists of a single semiconductor laser cavity, and is therefore mechanically simpler than the external cavity construction. In the monolithic structure, the laser cavity itself determines the mode-locked repetition rate. In order to achieve repetition rates on the order of tens or hundreds of GHz, it is necessary for the monolithic laser cavity to have lengths on the order of hundreds of μm to a few mm. Although this is longer than commonly used laser diodes [13], devices of this size range are now readily fabricated.

In general, the monolithic laser construction for mode-locking involves separating the waveguide structure into two or more sections. This is done by separating the electrical contact layer into isolated portions. At least one section will be forward biased to provide the normal laser amplification. The other sections can then be pumped with a modulated current to achieve active mode-locking, or reverse biased to achieve passive mode-locking. In this work, we focus on monolithic passive mode-locked lasers. These types of lasers can be categorized by the number and placement of their constituent sections.

The simplest monolithic construction is the tandem, or two-section waveguide. The construction for passive mode-locking in a tandem waveguide is shown in Figure 3.4. The gain section is pumped by a DC current. The saturable absorber is realized by applying a negative voltage bias. This type of saturable absorber formed by a waveguide is characterized by a recovery time τ_c around 10 to

15 ps [14]. If we consider mode-locked pulses on the order of picoseconds, this device satisfies the condition to be considered a slow saturable absorber [19].

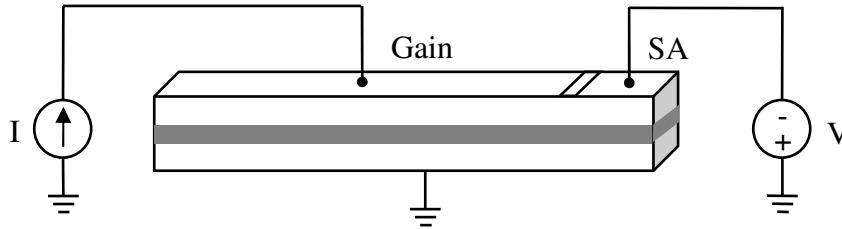


Figure 3.4: Schematic of tandem construction of monolithic passive mode-locked laser.

Another type of monolithic construction is called a colliding pulse mode-locked (CPM) laser. In this construction, the saturable absorber is placed in the center of the waveguide cavity rather than at the facet [13], as shown in Figure 3.5. A pulse propagating through the saturable absorber saturates the absorption for itself and for energy counterpropagating from the opposite direction. In the steady state operation of this construction, two pulses counterpropagate in the laser cavity and collide in the saturable absorber. Since the energies of two pulses combine to saturate the absorber, the saturation is stronger. This incoherent colliding pulse effect helps produce shorter and more stable mode-locked pulses because the effective saturation energy of the saturable absorber is reduced. The counterpropagating fields also tend to form standing waves in the saturable absorber, which leads to the formation of a temporary diffraction grating. This coherent colliding pulse effect tends to further decrease the effective saturation energy, although the effect in semiconductor waveguides is weak compared to the case of dye lasers [14]. The CPM construction

has been successfully implemented to produce nearly transform limited, 1.1 ps wide pulses at repetition rates ranging from 40 GHz to 350 GHz [20]. At lower repetition rates, hybrid mode-locking constructions have produced 6 ps wide pulses, although these were strongly chirped [21].

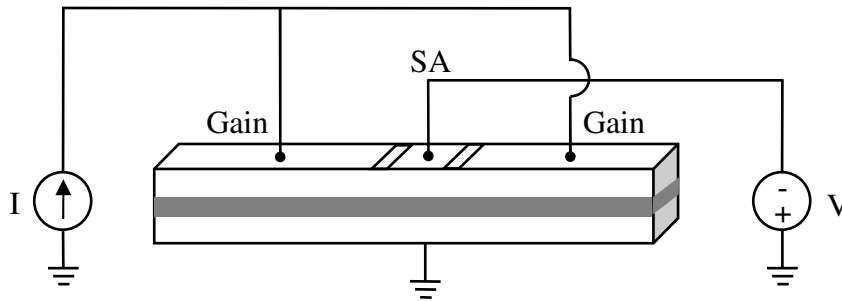


Figure 3.5: Schematic of colliding pulse (CPM) construction of monolithic passive mode-locked laser.

A variation on the CPM construction is the self-colliding pulse mode-locked (SCPM) construction, as shown in Figure 3.6. As in the tandem construction, the saturable absorber is placed at one facet of the laser cavity. In order to achieve colliding pulse action, the facet at the saturable absorber is coated with a high reflection surface. The mode-locked pulse then collides with itself as it reflects off the surface. An advantage of the SCPM laser is that it achieves the same repetition rate as the CPM construction with half the length. Since it is easier to fabricate shorter waveguides, this makes it easier to reach lower repetition rates. In addition, SCPM lasers are easier to fabricate because, unlike the standard CPM configuration, the SCPM does not require the saturable absorber to be placed at the exact center of the cavity. It is much easier to fabricate a waveguide with two separate section, and

simply cleave the ends of the desired cavity at any arbitrary location on the waveguide. The cleaving process used to produce the laser waveguide cavity naturally results in a significant reflection coefficient at the facet.

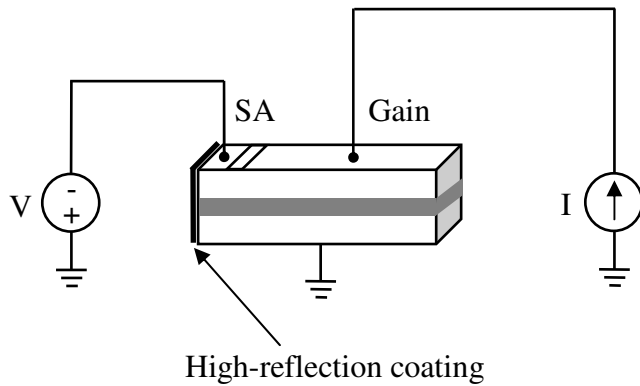


Figure 3.6: Schematic of colliding pulse (CPM) construction of monolithic passive mode-locked laser.

Another variation on the colliding pulse mode-locking construction has been achieved with ring lasers. In this construction, photolithographic techniques are used to create a waveguide in a self-enclosed ring geometry, as depicted in Figure 3.7. As with the linear cavity constructions, the gain and saturable absorber sections are differentiated by separating the metal contact layer into isolated portions. The output of the laser is typically extracted using a multimode interference (MMI) coupler. An advantage of the ring laser construction is that the counterpropagating pulses will collide in the saturable absorber even if it is not placed in the middle of the cavity. In addition, the ring laser has the advantage of achieving greater accuracy in producing a specified cavity length compared to the cleaving processes necessary to produce linear cavities. The disadvantage of ring lasers is the loss introduced by the waveguide bends and scattering from waveguide imperfections due to lithography

and etching. Passive mode-locking has been successfully implemented in semiconductor ring lasers to produce transform limited, 1.3 ps FWHM pulses at a repetition rate of 86 GHz [22].

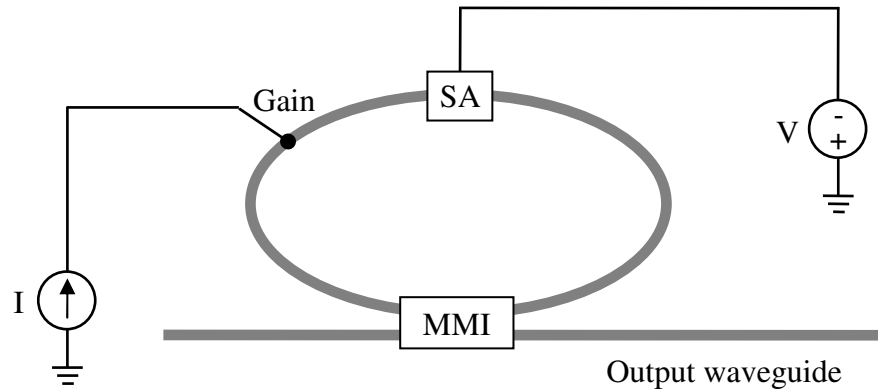


Figure 3.7: Schematic of ring construction of monolithic passive mode-locked laser (top view).

A further variation on the linear cavity construction is the extended cavity laser, as depicted in Figure 3.8. The linear and ring cavity structures discussed above share the quality that all the separated waveguide sections are either forward biased to create gain media or reverse biased to create saturable absorbers. This requires relatively high threshold currents, from tens to hundreds of mA, and suffers from greater noise and jitter problems compared to the external cavity laser construction. By incorporating a long passive waveguide region, an attempt is made to achieve the advantages of the external cavity in a monolithic structure. The passive regions in these constructions are called extended cavities. Various methods for producing the extended cavity have been experimentally verified. In one method, a quantum well intermixing (QWI) step is introduced into the waveguide fabrication process, which increases the band gap energy in one portion of the cavity to make it a passive

waveguide [23]. The resulting extended cavity laser exhibited better noise and jitter characteristics than previous monolithic mode-locked lasers, and produced 3.5 ps FWHM pulses with less chirp than previous lasers. A disadvantage of extended cavity lasers is that the repetition frequency of the pulses is more difficult to tune due to the high quality factor of the passive waveguide [13].

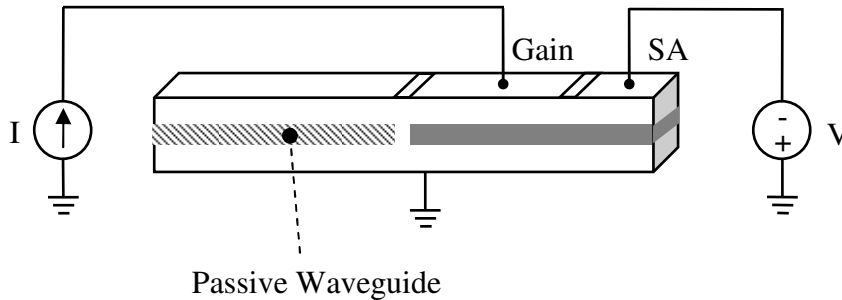


Figure 3.8: Schematic of extended cavity construction of monolithic passive mode-locked laser.

3.4 Experiments with Passive Mode-locking in a SCPM Laser

To demonstrate the technique of passive mode-locking, measurements were performed on a monolithic self colliding pulse mode-locked (SCPM) laser. The fabrication process of the SCPM laser is briefly described. The design includes the gain and saturable absorber sections typical in an SCPM laser, but also incorporates a longer low-gain section which performs the function of an extended cavity. The SCPM laser is subjected to varying operating conditions, and the repetition rate of the laser signal is monitored to characterize the passive mode-locking operation. The optical spectrum, RF spectrum, and cross correlation trace data of the SCPM laser in passive mode-locking operation are presented.

A monolithic semiconductor laser was fabricated by Arun Mampazhy at the Laboratory of Physical Sciences (LPS) with the University of Maryland, College Park. The fabrication process included standard photolithography techniques. The design of the laser is based on previous work performed at LPS by Dr. C. J. K. Richardson and Dr. J. Goldhar [24]. In that work, a symmetric CPM laser was fabricated and characterized. The design of the SCPM laser used in this work is the same, except the CPM configuration is cleaved in half to form an SCPM configuration. Commercially available IQE wafers with an InGaAsP active region on InP bulk substrate were used. The wafers are about $370\mu\text{m}$ thick. The basic cross-sectional structure of the semiconductor p-i-n diode laser is depicted in Figure 3.9.

The laser structure is composed of a lower cladding, an active region, an upper cladding, and a cap layer. The $0.8\mu\text{m}$ -thick lower cladding is n-doped with an Si dopant concentration on the order of 10^{18} cm^{-3} . The multiple quantum well active region is intrinsic, although it is sandwiched between two $0.1\mu\text{m}$ -thick graded index separate confinement heterostructure (GRINSCH) layers which are designed to improve the band structure of the laser diode. Above the upper GRINSCH layer is a $0.05\mu\text{m}$ -thick etch stop layer and a $0.05\mu\text{m}$ -thick spacer layer for strain relief. Above this is the $1.6\mu\text{m}$ -thick upper cladding, which is p-doped with a Zn dopant concentration on the order of 10^{18} cm^{-3} . The $0.25\mu\text{m}$ -thick cap layer is strongly p-doped with a Zn dopant concentration on the order of 10^{19} cm^{-3} . The cap layer provides a good ohmic contact for electrical pumping. The cap and upper cladding layers are wet etched, forming a $2\mu\text{m}$ -thick and $3\mu\text{m}$ -wide ridge that serves as the waveguide. These layers comprise the basic semiconductor structure.

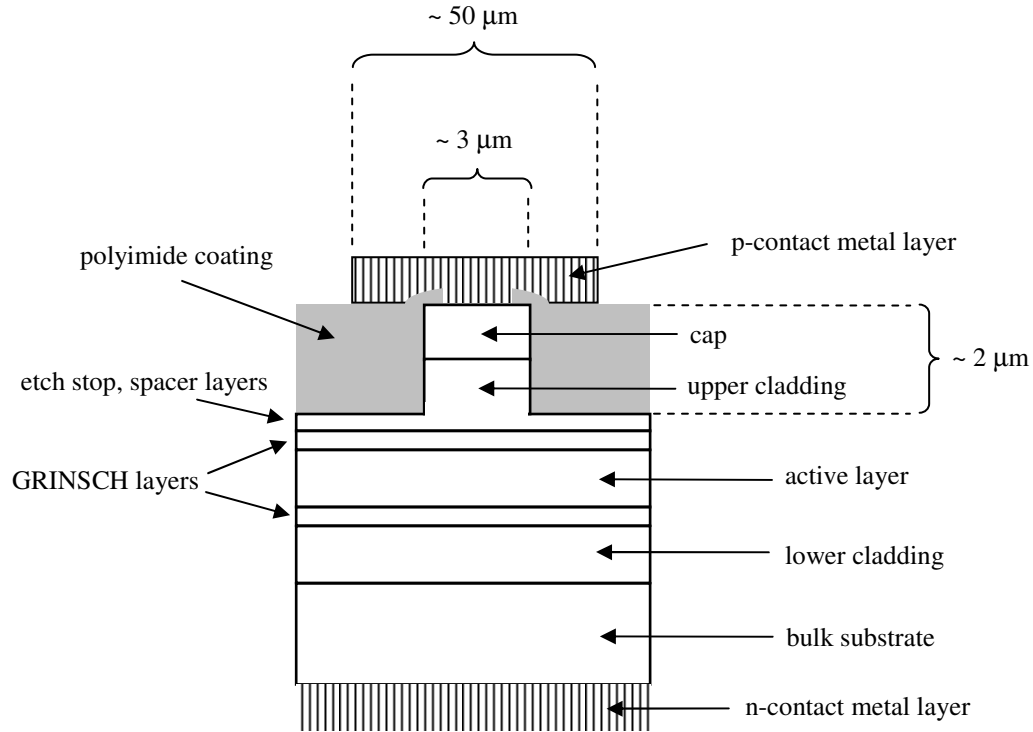


Figure 3.9: Schematic of cross-section of SCPM laser (not to scale).

To operate the semiconductor structure as a laser, it is necessary to have points of contact for electrical pumping. The semiconductor structure is coated with PI2562 polyimide using adhesion promoter VM651, partially cured, coated with a second polyimide layer, and then fully cured. The coating is then dry etched using a reactive ion etching (RIE) process to create a window through the polyimide to the cap layer. Next, the p-contact metal layer, consisting of a 50 \AA -thick layer of Ti, a 300 \AA -thick layer of Pt, and a $1 \mu\text{m}$ -thick layer of Au, is deposited by e-beam lithography. The p-contact layer is $50 \mu\text{m}$ wide, and is deposited through a mask which includes $10 \mu\text{m}$ -long gaps that run perpendicular to the waveguide. These gaps separate the p-contact into isolated pieces of specified lengths. Then, the n-contact metal layer is added onto the bottom surface of the bulk substrate using an e-beam

CHA evaporator. Finally, the portions of the cap layer which lie under the $10\mu\text{m}$ -long gaps of the p-contact metal are etched away. This completes the separation of the monolithic laser diode into electrically isolated sections.

The fabricated laser diode structure is cleaved to form a laser cavity. To meet the goal of a pulse repetition rate of roughly 10.8 GHz, the laser cavity is cleaved to a total length of 4 mm. This total length is split into three sections. The first section will be biased as a saturable absorber, and the second section will be biased as a gain medium. These two sections comprise the standard SCPM configuration described in Section 3.3. The third section will also be biased as a gain medium, but it will be less strongly biased. It is intended to function like the extended cavity described in Section 3.3, but without requiring special fabrication techniques, and will be used to tune the effective cavity length. The length of each section was controlled in fabrication by the mask used for depositing the p-contact metal layer, and also by the cleaving of the end facets. The saturable absorber section is $75\mu\text{m}$ long, the high-gain section is $400\mu\text{m}$ long, and the low-gain section is $3525\mu\text{m}$ long.

The final product of the SCPM laser is shown in Figure 3.10. First, the fabricated laser diode structure is cleaved to form a laser cavity of the desired length. Then, to prepare the laser diode structure for passive mode-locking operation, the laser is mounted onto a submount structure. The laser cavity is soldered onto the conducting base of the submount, providing an electrical ground connection to the n-contact layer of the laser. The different sections of the p-contact layer of the laser are wire-bonded to different electrically isolated pads on the submount structure. The submount structure itself is then soldered onto a larger mount structure which is fitted

with electrically isolated pins. Each of the pads on the submount is wirebonded to one of the pin contacts on the larger mount structure. The pins are mechanically stable enough to support connections to standard electrical wires. To operate the laser in a passive mode-locking regime, each pin is connected to a standard DC current or voltage power supply. This allows each section of the laser to be independently biased as either a gain medium or saturable absorber.

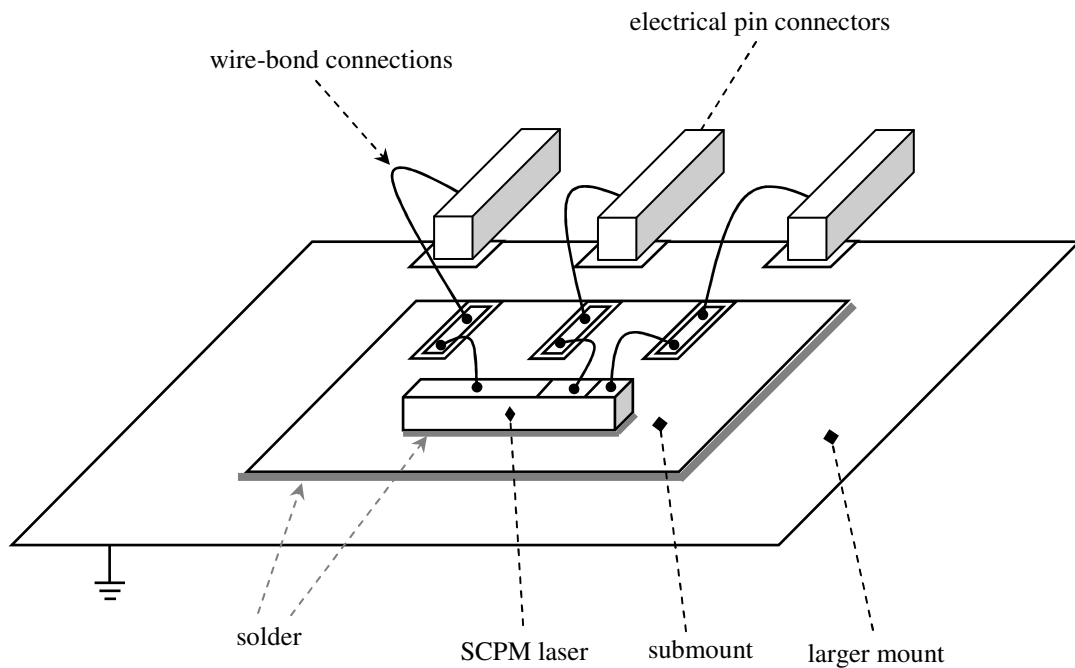


Figure 3.10: Schematic of fabricated SCPM laser on submount and mount structure.

The monolithic SCPM laser, on its mount structure, is placed on a vacuum-pump secured, temperature-controlled stage prepared by Dr. Shuo-Yen Tseng of the Laboratory of Physical Sciences (LPS). The light emitted from both sides of the SCPM laser is coupled to optical fibers with angled tips. This is depicted in Figure 3.11. The optical fibers are carefully aligned to the two facets of the SCPM laser using electronically controlled translation stages.

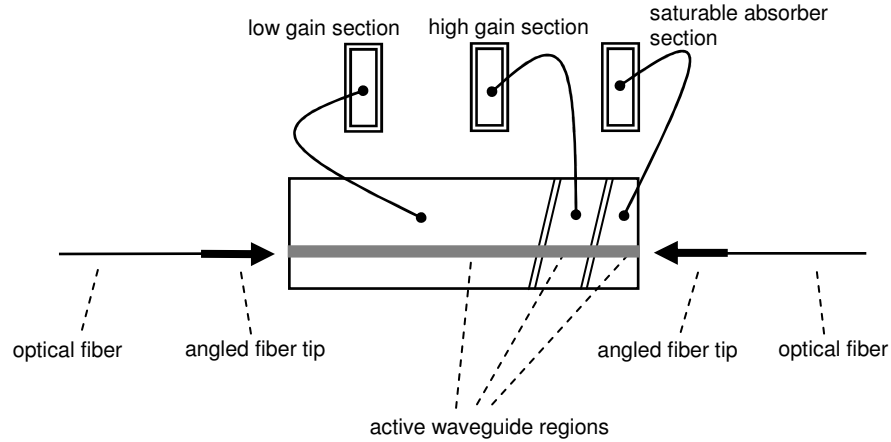


Figure 3.11: SCPM laser with input and output coupled through angled fiber tips.

The monolithic laser can be operated in several different regimes of operation, depending on the biasing conditions of the three sections. Each section may be forward or reverse biased with current or voltage sources. The biasing conditions must be properly set to bring the SCPM laser to passive mode-locking operation. Other possible regimes of operation include continuous wave (CW) lasing and self pulsation [20]. In order to verify the regime of operation of the laser, we measure its RF and optical spectra.

Passive mode-locking is achieved when the high-gain and low-gain sections are forward biased to produce gain media, and the saturable absorber section is reverse biased to produce an absorbing medium. Thus, the three controllable variables of the SCPM laser are the low-gain section pumping current I_{LG} , the high-gain section pumping current I_{HG} , and the saturable absorber section reverse bias voltage V_{SA} . As explained in Section 3.2.3, the high-gain and saturable absorber sections form the basic passive mode-locking configuration. The low-gain section is included to provide a method for tuning the effective optical cavity length and

therefore the RF repetition frequency across one or a few axial modes. As explained in Section 2.3, there is a direct relationship between the charge carrier density and the real part of the susceptibility of the gain medium. The real part of the susceptibility is related to the effective index of refraction of the gain medium. As the pump current is increased, the charge carrier density increases. This results in a slight increase in the effective index of refraction, which means the optical length of the low gain-section becomes slightly longer. The round trip time of the entire cavity becomes slightly longer, and the laser repetition rate decreases. Therefore, the values of I_{HG} and V_{SA} are chosen to obtain passive mode-locking operation, while I_{LG} is varied to tune the repetition rate. The goal is to achieve linear tuning of the repetition frequency while ensuring passive mode-locking operation.

It should be noted that the charge carrier density is not the only factor that may affect the repetition rate of the laser. The thermo-optic effect, which relates the change in index of refraction to the change in the temperature of the medium, is strictly also a potential factor. However, the previous study explains that the thermo-optic effect predicts an increase in the repetition rate with increasing temperature [24]. An increase in temperature should only occur with increasing pumping current. This contradicts observed results, which show a decrease in repetition rate with increasing pumping current. Therefore, it is concluded that the thermo-optic effect is not a dominant effect in this type of device. In addition, the electro-optic effect predicts a change in the refractive index depending on the change in the reverse bias voltage on the saturable absorber section. However, in the

experiment, the voltage on the absorber section is kept constant. Therefore, the electrooptic effect is not a factor in the experiment.

In order to achieve passive mode-locking, the values of I_{HG} and V_{SA} were varied while the RF spectrum of the laser output was monitored using an HP 70908A RF spectrum analyzer. The high gain section current I_{HG} was varied from 50 mA to 70 mA, and the saturable absorber section voltage V_{SA} was varied from -2.2 V to -3.0 V. For each value of I_{HG} and V_{SA} , the low gain current I_{LG} was also varied across a reasonable range from 185 mA to 240 mA to tune the repetition frequency. The results are shown in several graphs in Figure 3.12. Each graph represents a different value of V_{SA} . The three curves in each graph represent the three different values of I_{HG} that were used. The values of I_{LG} are represented by the independent axis in each graph, and the measured RF frequency is given by the dependent axis.

The results underscore the strong dependence of the monolithic laser operation on the biasing conditions. Fairly linear tuning of the repetition frequency by variation of the low gain current I_{LG} is achieved for saturable absorber voltage values of -2.2 V and -2.4 V. If the value of V_{SA} is made smaller, as in the case of -2.0 V, the tuning relationship has a positive curvature. Similar results have been reported by other researchers [25]. As the value of V_{SA} increased, the tuning relationship also becomes nonlinear, and as the voltage approaches -2.8 V and -3.0 V, the laser begins to leave the mode-locking regime.

For voltages of -2.2 V and -2.4 V, where the tuning is more linear, the high gain section current I_{HG} plays a role. For a current I_{HG} of 50 mA, the tuning

relationship is linear but the tuning range is only 8.51 MHz and 2.76 MHz for V_{SA} voltages of -2.2 V and -2.4 V, respectively. By contrast, a current I_{HG} of 60 mA has a linear tuning range of 18.77 MHz and 12.27 MHz for V_{SA} voltages of -2.2 V and -2.4 V, respectively. For a current I_{HG} of 70 mA, the tuning range is not sufficiently linear to be useful. Therefore, the optimal biasing values for passive mode-locking and linear repetition rate tuning are $V_{SA} = -2.2$ V and $I_{HG} = 60$ mA. A representative result of the RF spectrum is shown in Figure 3.13 for these optimal bias conditions and a low gain section current of $I_{LG} = 220$ mA. The measured RF spectrum indicates that for the given bias conditions, the repetition frequency of the mode-locked pulse train is about 10.848 GHz.

The results of these characterization measurements indicate that the good passive mode-locking is achieved for a saturable absorber section reverse bias of $V_{SA} = -2.2$ V and a high gain section current of $I_{HG} = 60$ mA. A fairly linear tuning of the pulse repetition rate is achieved as the low gain section current I_{LG} is varied from 200 mA to 240 mA. The repetition rate varies from about 10.855 GHz at $I_{LG} = 200$ mA to about 10.836 GHz at $I_{LG} = 240$ mA.

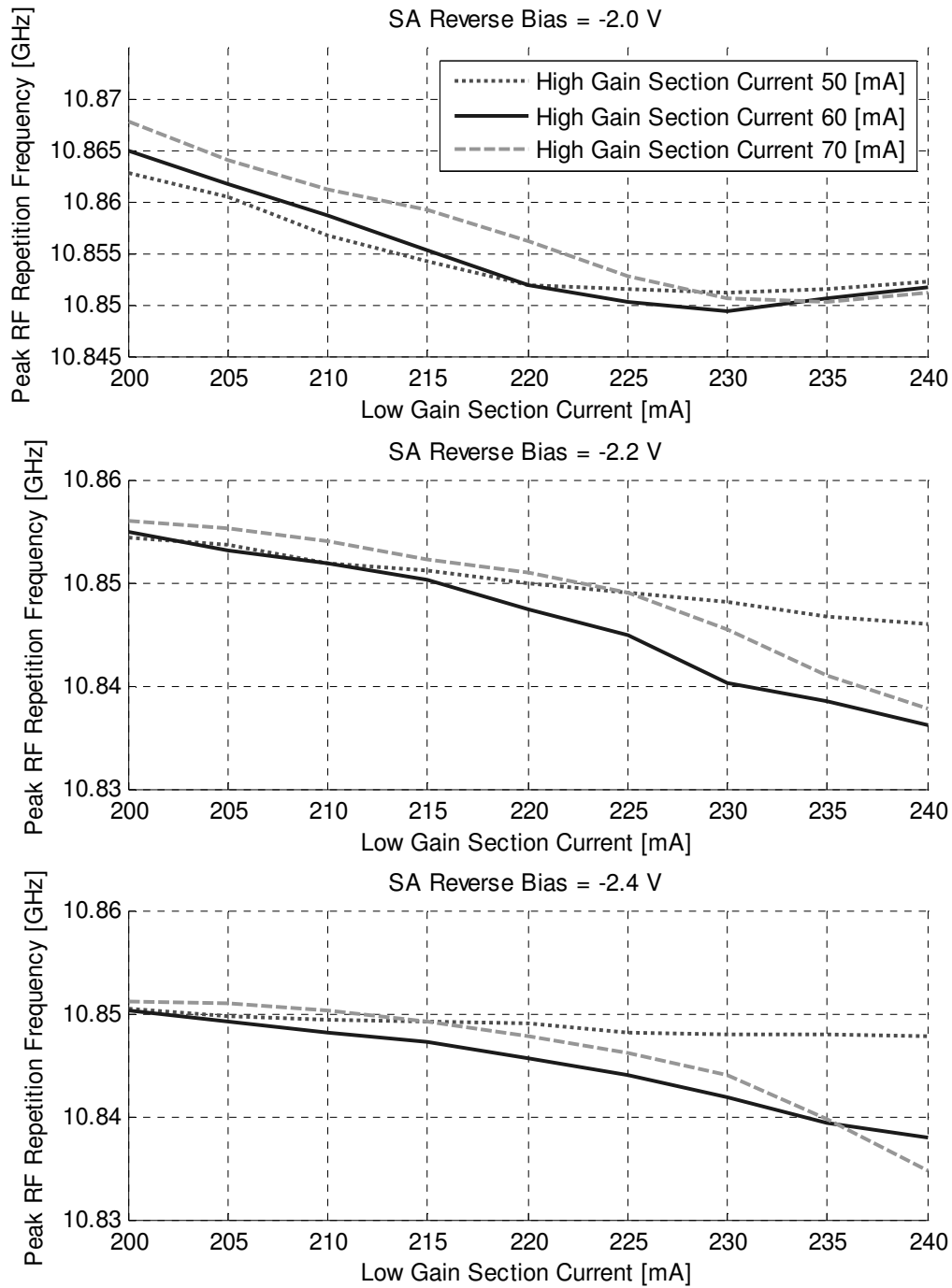


Figure 3.12: Peak RF Repetition Frequency for different values of V_{SA} , I_{HG} , and I_{LG} .

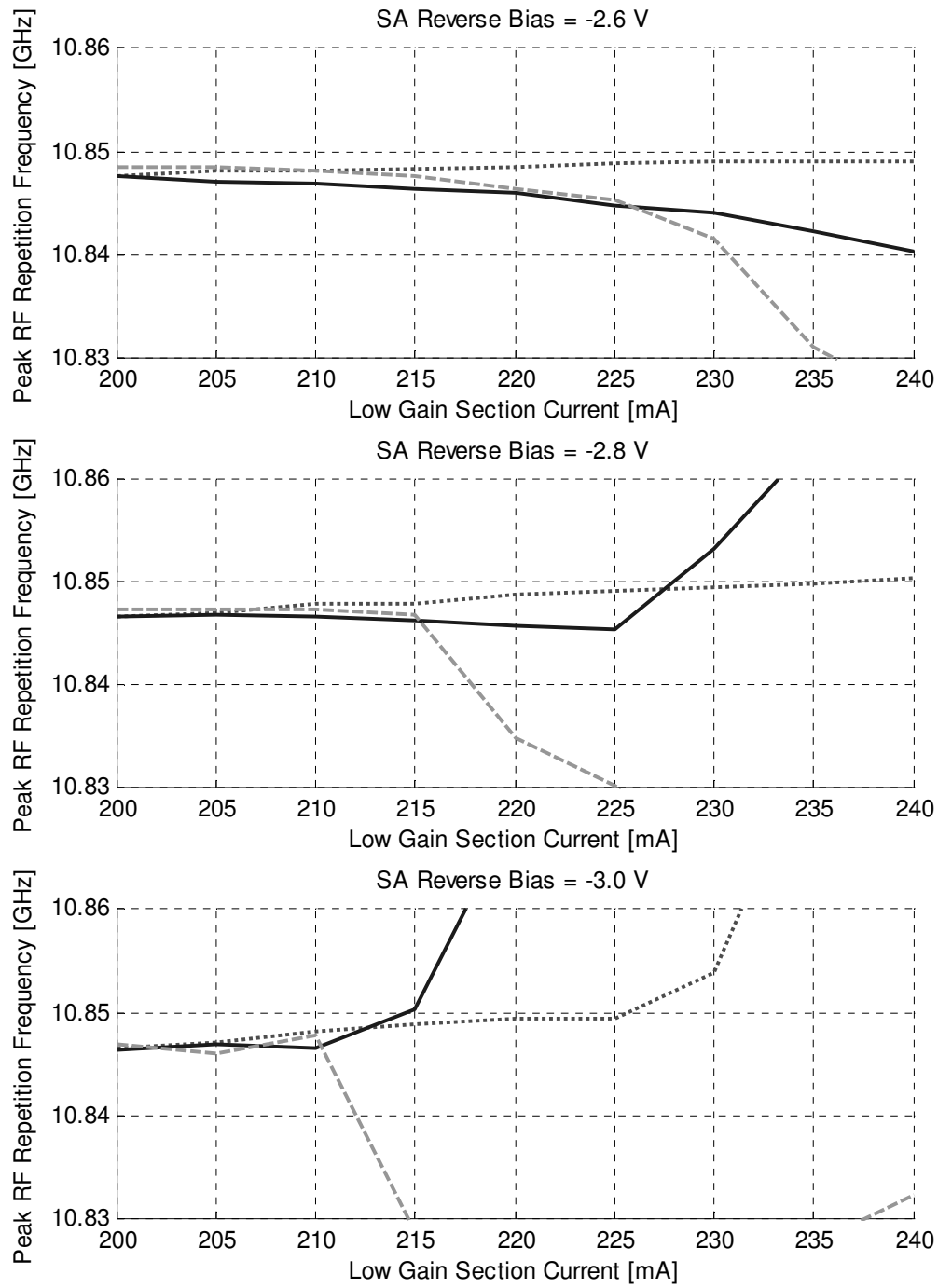


Figure 3.12: Peak RF Repetition Frequency for different values of V_{SA} , I_{HG} , and I_{LG} .

At the optimal biasing values of $I_{HG} = 60 \text{ mA}$ and $V_{SA} = -2.2 \text{ V}$, the optical spectrum was measured using an HP 70951B Optical Spectrum Analyzer (OSA), and results are shown in Figure 3.14 for several values of I_{LG} . The curves represent the amplitude distribution of the axial modes, as discussed in Section 3.2.1. The measured spectrum is similar to results obtained by other researchers [21]. It is important to note that the individual axial modes are not visible because the OSA has a minimum resolution bandwidth of 0.1 nm. The axial modes corresponding to a repetition frequency of about 10.8 GHz have a spacing in wavelength on the order of 0.08 nm. The measured results indicate that the optical spectrum does not change dramatically as the low gain section is tuned across a moderate range of current values.

The auto-correlation of the SCPM laser pulses was measured using the same method described in Section 2.4.2 for measuring the commercial mode-locked laser. The result is shown in Figure 3.15. The SCPM laser was biased at the optimal conditions of $I_{HG} = 60 \text{ mA}$ and $V_{SA} = -2.2 \text{ V}$, with the low gain section current set to 185 mA. The auto-correlation trace consists of a broad pulse shape and a narrow coherence spike. The broad pulse is the actual mode-locked pulse, and has a FWHM pulse width of about 26 ps. The FWHM of the coherence spike is about 2 ps, which corresponds to a bandwidth of $5 \times 10^{11} \text{ Hz}$. With a center wavelength of about $\lambda_0 \approx 1562.5 \text{ nm}$, this bandwidth corresponds to a width in wavelength of $\Delta\lambda = \Delta f \cdot \lambda_0^2 / c \approx 4 \text{ nm}$. Comparing this to the measured spectrum shown Figure 3.14, it is clear that bandwidth of the coherence spike comparable to that of the laser spectrum. This is an indication that the broad measured pulse is actually an envelope

under which there are rapidly fluctuating substructures. The coherence spike is a measure of the coherence time of these substructures.

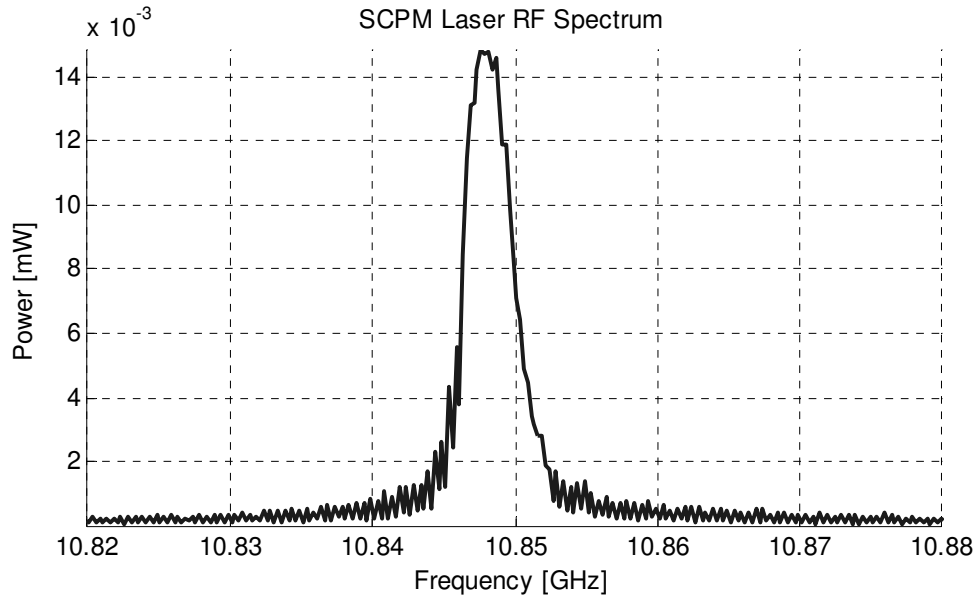


Figure 3.13: Measured RF spectrum of the monolithic laser in passive self colliding pulse mode-locking (SCPM) operation. High gain section is biased at $I_{HG} = 60$ mA , saturable absorber section is biased at $V_{SA} = -2.2$ V , and low gain section is biased at $I_{LG} = 220$ mA .

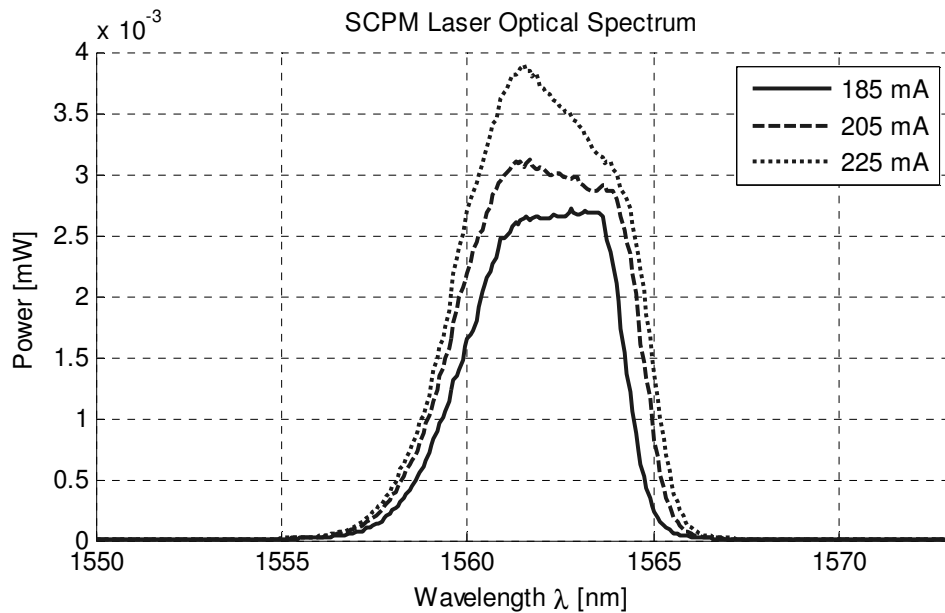


Figure 3.14: Measured optical spectrum of the monolithic laser in passive self colliding pulse mode-locking (SCPM) operation. High gain section is biased at $I_{HG} = 60$ mA, saturable absorber section is biased at $V_{SA} = -2.2$ V, while low gain section biasing is varied with values $I_{LG} = 185$ mA, 205 mA, and 225 mA.

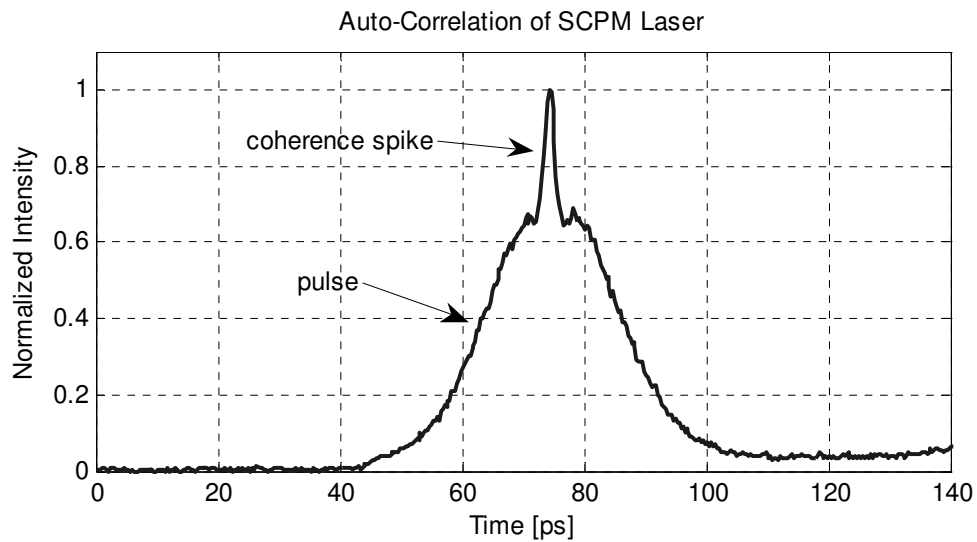


Figure 3.15: Measured auto-correlation trace of the monolithic laser in passive self colliding pulse mode-locking (SCPM) operation. High gain section is biased at $I_{HG} = 60$ mA, saturable absorber section is biased at $V_{SA} = -2.2$ V, and low gain section biasing is biased at $I_{LG} = 185$ mA.

Chapter 4: CW Injection Locking in Monolithic Lasers

4.1 Introduction to CW Injection Locking Theory

As mentioned Chapter 1, CW injection locking is a method of controlling the optical frequency of a CW laser. The technique entails injecting a relatively weak oscillator signal of optical frequency ω_1 from an external source into a laser, which on its own produces a strong oscillating signal at optical frequency ω_0 . Under certain conditions, the laser will produce an oscillating signal at ω_1 , and the phase of this output can be theoretically predicted. In this case, the laser is said to be injection locked by the weaker external CW signal. The theory of CW injection locking is well understood [9], and a brief review of the basic concepts is presented here.

To begin, consider a linear laser cavity with gain and loss factors δ_m and δ_c , respectively, and field reflection and transmission coefficients ρ and τ , respectively, at the cavity facets. Suppose this laser produces a single mode CW output with optical frequency ω_0 . In the absence of injection, this CW output is called the free-running output of the laser. Now, suppose an external CW signal with optical frequency ω_1 is injected into one facet of the laser, as depicted in Figure 4.1. Let \tilde{E}_{circ} be the phasor representation of the total optical wave traveling around the cavity, measured at a plane just inside the input facet and traveling into the laser. Then, \tilde{E}_{circ} is the sum of two different sources of optical waves. Let \tilde{E}_{refl} be the portion of the circulating wave which comes from the optical signal inside the laser cavity reflecting

off the input facet. Let \tilde{E}_{inj} be the portion of the circulating wave which comes from the injected signal. The signal \tilde{E}_{inj} is, in turn, the portion of the external incident wave \tilde{E}_{inc} which is transmitted through the input facet of the laser. A portion of \tilde{E}_{inc} is also reflected from the input facet. The importance of this portion will be discussed in Section 4.3.

In general, the phasor representations of the waves are defined with respect to some optical frequency. Here, we define them with respect to the frequency of the incident wave, ω_l . In this convention, a wave oscillating at ω_l is represented by a phasor with a fixed angle in the complex phasor coordinate plane. A wave which is oscillating at a frequency other than ω_l will simply have its frequency expressed as a time-varying phase difference. This means that its phasor will rotate in the complex plane. In this convention, each of the phasors represents a real field of the form

$$E_x(t) = \text{Re} \left[\tilde{E}_x(t) e^{j\omega_l t} \right] \quad (4.1)$$

where the subscript x may refer to the incident, injected, circulating, or reflecting waves. Note, this equation describes the locked state where all the considered fields are oscillating at the same frequency. By definition, the waves defined in the system must satisfy the equation

$$\tilde{E}_{circ}(t) = \tilde{E}_{refl}(t) + \tilde{E}_{inj}(t) \quad (4.2)$$

at any given moment in time. For self consistency, the reflected wave must be equal to the circulating wave that left the reference plane one round trip time T_{RT} earlier, after it has experienced the gain, loss, and phase shift associated with the laser cavity. This self consistency requirement can be approximated by the equation [3]

$$\tilde{E}_{refl}(t) = \tilde{E}_{circ}(t - T_{RT}) \times e^{\frac{\delta_m - \delta_c}{2} - jT_{RT}(\omega_1 - \omega_0)} \quad (4.3)$$

where T_{RT} is the round trip time of the laser cavity, and the factor $\omega_1 - \omega_0$ represents the fact that the circulating and reflected waves oscillate at an optical frequency ω_0 .

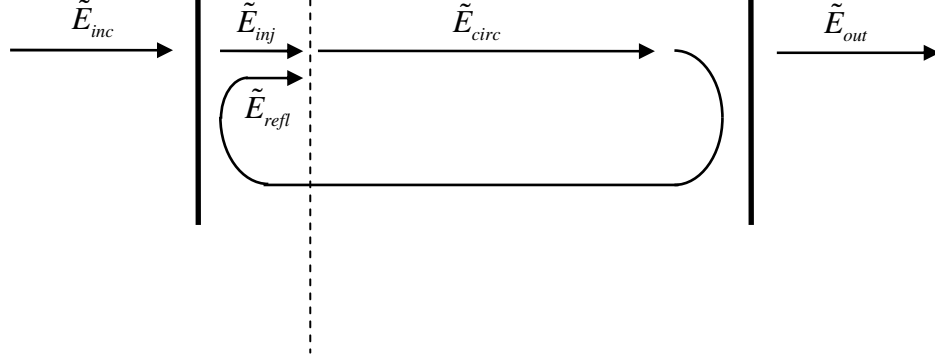


Figure 4.1: Schematic of model for CW injection locking.

The condition expressed in Eq. (4.3) is technically only true if the loss and gain factors δ_m and δ_c do not change rapidly during the course of a round trip. In this work we are concerned mainly with the steady state solution to injection locking, and we also restrict our analysis to the case of a weak injected signal. Therefore, Eq. (4.3) is valid for the cases of interest.

Recall that the phasors in Eq. (4.3) are referenced to the optical frequency ω_1 of the injected signal. The difference between this frequency and the free-running laser frequency of ω_0 is relegated to a phase term. It will be shown that this detuning only affects the phase, while the signals in the cavity will oscillate at ω_1 , thereby achieving injection locking. The expression given in Eq. (4.3) can be converted to a fairly accurate differential equation, assuming that the frequency detuning between

ω_1 and ω_0 is small compared to the axial mode spacing $\Delta\omega_{ax}$, and that the circulating wave does not change severely from one round trip to the next. The expression can then be rewritten as

$$\tilde{E}_{refl}(t) \approx \left[1 + \frac{\delta_m - \delta_c}{2} - jT_{RT}(\omega_1 - \omega_0) \right] \tilde{E}_{circ}(t) - T_{RT} \frac{d\tilde{E}_{circ}(t)}{dt} \quad (4.4)$$

It is convenient to introduce a cavity decay time

$$\tau_c = \frac{T_{RT}}{\delta_c} \quad (4.5)$$

and a normalized gain-to-loss ratio

$$r = \frac{\delta_m}{\delta_c} \quad (4.6)$$

Substituting these definitions along with the condition of Eq. (4.2) into the differential equation of Eq. (4.4), we can eliminate \tilde{E}_{refl} from the equation and rearrange terms to obtain

$$\frac{\tilde{E}_{inj}}{T_{RT}} \approx - \left[\frac{r-1}{2\tau_c} - j(\omega_1 - \omega_0) \right] \tilde{E}_{circ} + \frac{d\tilde{E}_{circ}}{dt} \quad (4.7)$$

It is also convenient to express the phasors for the circulating and injected waves in terms of their respective amplitudes and phases, which we define as

$$\begin{aligned} \tilde{E}_{circ}(t) &= E(t) e^{j\phi(t)} \\ \tilde{E}_{inj}(t) &= E_1(t) e^{j\phi_1(t)} \end{aligned} \quad (4.8)$$

Substituting these definitions into Eq. (4.7), we obtain

$$\frac{E_1(t) e^{j\phi_1(t)}}{T_{RT}} = - \left[\frac{r-1}{2\tau_c} - j(\omega_1 - \omega_0) \right] E(t) e^{j\phi(t)} + j E(t) e^{j\phi(t)} \frac{d\phi(t)}{dt} + e^{j\phi(t)} \frac{dE(t)}{dt} \quad (4.9)$$

The $\exp(j\phi(t))$ factor in each term on the right hand side can be divided out and combined with the $\exp(j\phi_1(t))$ factor on the left hand side. Eq. (4.9) can then be separated into two equations by collecting and equating the real and imaginary parts of each side of the equation. The real parts give

$$\frac{E_1}{E} \frac{1}{T_{RT}} \cos(\phi_1 - \phi) = -\frac{r-1}{2\tau_c} + \frac{1}{E} \frac{dE}{dt} \quad (4.10)$$

and the imaginary parts give

$$\frac{E_1}{T_{RT}} \sin(\phi_1 - \phi) = (\omega_1 - \omega_0) E + E \frac{d\phi}{dt} \quad (4.11)$$

In the steady state, the time derivative terms are equal to zero. Eq. (4.10) essentially goes to zero on both sides of the equation, assuming the injected signal is weak so that $E_1 \ll E$ on the left hand side, and assuming $r \approx 1$ on the left hand side because in steady state, the gain of the laser saturates down to a level very close to the loss of the cavity. Eq. (4.11), however, is very important because it provides a formula that relates the frequency detuning to the injected wave amplitude and the phase difference between the injected and circulating waves, as given by

$$(\omega_1 - \omega_0) = \frac{E_1}{E} \frac{1}{T_{RT}} \sin(\phi_1 - \phi) \quad (4.12)$$

The maximum allowed amplitude of the sine function is 1. Therefore, the maximum detuning is given by

$$\omega_m = \frac{1}{T_{RT}} \frac{E_1}{E} \quad (4.13)$$

This expression gives the maximum allowed detuning between the free-running frequency ω_0 of the laser and the injected frequency ω_1 of the external signal. If the

injected frequency is detuned by an amount equal to or less than ω_m , it is said to be within the locking range of the laser. If the amount of detuning is larger than ω_m , injection locking will not occur.

Solutions outside the locking range are more complicated. It can be shown that if the injected signal is well outside the locking range, such that $|\omega_1 - \omega_0| \gg \omega_m$, the signal that builds up inside the laser cavity will be close to the free-running frequency ω_0 , but pulled slightly towards the injected frequency [3]. The new oscillation frequency of the laser is given by the approximate expression

$$\omega_{osc} = \omega_1 - \omega_b \approx \omega_0 + \frac{\omega_m^2}{2(\omega_1 - \omega_0)} \quad (4.14)$$

where ω_b is the beat frequency, which is given by

$$\omega_b = \sqrt{(\omega_1 - \omega_0)^2 - \omega_m^2} \quad (4.15)$$

However, the laser signal in this case will not be a pure sine wave at this pulled frequency. Its dominant spectral component will be at ω_{osc} , but it will also have sidebands at other frequencies displaced by integer multiples of ω_b away from ω_1 , as in $\omega_1 \pm n\omega_b$. Solutions outside the locking range will not be treated in this work.

The regime of interest is those injected frequencies which are within the locking range. Eq. (4.12) indicates that the phase difference between the injected signal and the circulating signal is fixed to a specific value. The phase difference depends on the relative amplitudes of the injected and circulating waves, as well as the amount of the frequency detuning. Rearranging Eq. (4.12), the phase difference is given by

$$\phi_1 - \phi = \sin^{-1} \left[\frac{(\omega_1 - \omega_0)}{\omega_m} \right] \quad (4.16)$$

From Eq. (4.16), it is clear that as the injected frequency is tuned across the locking range, the phase difference between the injected and circulating waves varies monotonically over a range of π radians, spanning values from $\pi/2$ to $-\pi/2$.

From Eq. (4.13), the maximum detuning ω_m depends on the round trip time and the ratio of the injected and free-running field amplitudes. The field amplitude units can be normalized such that the square of the magnitude of the amplitude represents the power of the wave. The normalization factor is the same for all fields in a given medium. Therefore, the ratio of field amplitudes is equivalent to the square root of the ratio of signal power, as long as the considered fields are either both inside or both outside the cavity. The definition of ω_m in Eq. (4.16) is given in terms of the ratio of injected and circulating field amplitudes E_1/E . In terms of power, this is simply the ratio $\sqrt{P_{inj}/P_{circ}}$. This can be translated to a ratio of the incident power and free-running output power, both of which are waves outside the cavity. The injected power is simply the incident power multiplied by the power transmission coefficient $T = |\tau|^2$ of the input facet. Assuming that the injected power is very weak compared to the free-running laser power, the output power from the laser is simply the circulating wave power multiplied by the power transmission coefficient T of the input facet. Technically this is the output power from the other laser facet, but in steady state the laser emits the same output at both facets. Therefore, the ratio of

injected and circulating field amplitudes is related to the ratio of incident and free-running output power by

$$\frac{E_1}{E} = \sqrt{\frac{P_{inj}}{P_{circ}}} = \sqrt{\frac{P_{inc} T}{P_{out}/T}} = T \sqrt{\frac{P_{inc}}{P_{out}}} \quad (4.17)$$

Experimentally, it is easier to work with the reflected portion of the incident power rather than the total incident power itself. Therefore the ratio can be further translated and written in terms of the reflected portion of the incident power, $P_{inc,refl}$, which is simply the total incident power multiplied by the power reflection coefficient $R = |\rho|^2$ of the facet. This ratio is related to the original field amplitude ratio by

$$\frac{E_1}{E} = T \sqrt{\frac{P_{inc}}{P_{out}}} = T \sqrt{\frac{P_{inc,refl}/R}{P_{out}}} = \frac{T}{\sqrt{R}} \sqrt{\frac{P_{inc,refl}}{P_{out}}} \quad (4.18)$$

The phase difference between the incident wave and the injection locked laser output is given by Eq. (4.16), which is expressed in terms of the ratio between the reflected incident power and the free-running laser power. The phase difference $\phi_1 - \phi$ is plotted in Figure 4.2 as a function of frequency detuning $\omega_0 - \omega_l$ for power ratios $P_{inc,refl}/P_{out}$ equal to 1/100, 1/50, and 1/10. In each case, the phase difference varies monotonically from $\pi/2$ to $-\pi/2$. For the case of zero detuning, the phase difference is always zero. For each value of the power ratio, the locking range is the range of frequency detuning spanned by the phase difference values. The value of the locking range is equal to $2\omega_m$ because the injected frequency can be detuned both below and above the free-running frequency. The calculated values of the locking

range are 2.3175 GHz for a power ratio of 1/100 , 3.2774 GHz for a ratio of 1/50 , and 7.3286 GHz for a ratio of 1/10 .

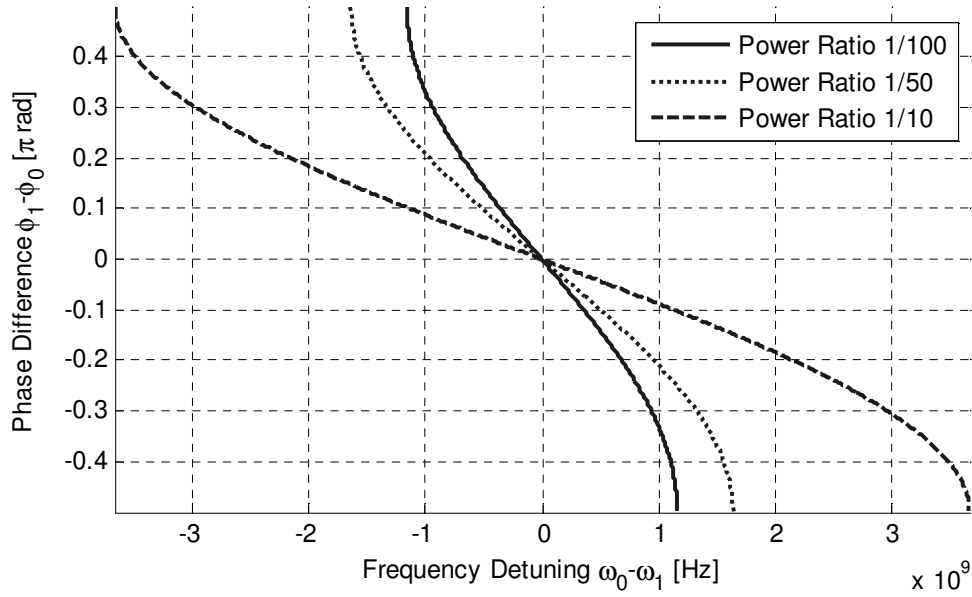


Figure 4.2: Phase difference $\phi_1 - \phi_0$ between the injected wave and the injection locked laser output wave, for several values of the power ratio $P_{inc,refl}/P_{out}$.

To visualize the physical meaning of the frequency detuning and phase difference, it is instructive to return to the phasor picture in which all the fields \tilde{E}_{inj} , \tilde{E}_{inc} , \tilde{E}_{circ} , \tilde{E}_{refl} , and \tilde{E}_{out} are defined. As explained, each of these phasors are defined with respect to the injected frequency ω_1 . In the steady state, the free-running laser gain will saturate down a level approximately equal to the total cavity loss, such that $r \approx 1$. That means \tilde{E}_{circ} and \tilde{E}_{refl} will have roughly the same amplitude, \tilde{E}_0 , which is usually much larger than the amplitude of \tilde{E}_{inj} . However, even though the magnitude of \tilde{E}_{circ} does not change as it makes a round trip through

the cavity to become \tilde{E}_{refl} , the phase shift associated with a round trip transit still applies. In the plane referred to ω_1 , this round-trip phase shift is $(\omega_1 - \omega_0)T_{RT}$. In the complex plane, this means that \tilde{E}_{circ} will rotate by an angle on each round trip. Therefore, there is an angle between \tilde{E}_{circ} and \tilde{E}_{refl} . In steady state operation, this gap must be bridged by \tilde{E}_{inj} in order to satisfy self consistency. This is depicted in Figure 4.3.

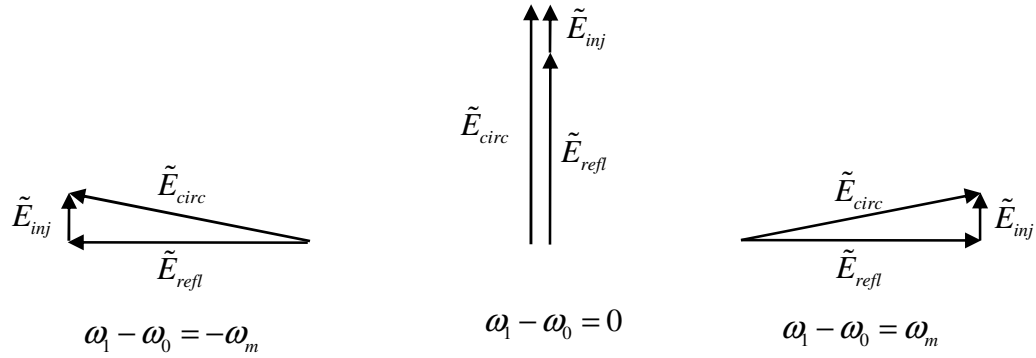


Figure 4.3: Phasor diagrams for injection locked laser, at center and at edges of locking range.

From Figure 4.3, it can be observed that if the angle between \tilde{E}_{circ} and \tilde{E}_{refl} is too large, which corresponds to a large detuning between ω_1 and ω_0 , then the injected wave \tilde{E}_{inj} will not be able to bridge the gap and form a self consistent solution. The edges of the locking range occur when \tilde{E}_{circ} and \tilde{E}_{inj} have a $\pm\pi/2$ phase difference. The phasor diagrams illustrate the relationship between the frequency detuning $\omega_1 - \omega_0$ and the phase difference $\phi - \phi_1$. Incidentally, the cases shown in Figure 4.3 correspond to a round-trip gain that is very slightly less than the round-trip loss. Analogous phasor diagrams corresponding to a round-trip gain

slightly greater than loss can also be drawn. The diagrams would look identical to the ones in Figure 4.3, except with \tilde{E}_{circ} and \tilde{E}_{refl} interchanged. However, that situation is unstable to perturbations [9].

4.2 Experiment on CW Injection Locking in Monolithic Lasers

To demonstrate CW injection locking, the same SCPM laser described in Section 3.4 is operated as a CW laser. A commercial CW laser is used for the external injection signal. First, the operation of the fabricated SCPM laser in CW mode is described. A simple theoretical model known as the Rigrod analysis [9] is used to calculate the CW output power of a laser as a function of pumping current. The theory is verified by measured data of the free-running fabricated laser. Then, CW injection locking of the laser is performed and results are presented. The CW injection locking of the laser is characterized by measuring the optical spectrum.

To operate the fabricated SCPM laser in CW regime, the three sections of the laser are forward biased with the same current density. This biasing condition creates a uniform gain medium throughout the laser cavity. This type of device can be modeled as a regenerative amplifier [9]. The laser can be characterized by such parameters as the saturable gain coefficient $\alpha_m(z)$, unsaturable cavity loss coefficient α_0 , cavity facet power reflection and transmission coefficients R and T , and cavity length L . This is essentially the same type of device used to describe CW injection locking in Section 4.1. If the laser gain response is homogeneously

broadened, and assuming the unsaturated gain is pumped above a threshold level, this type of device is expected to oscillate in single-mode CW operation.

The Rigrod analysis derives a formula which gives the output intensity of a CW laser as a function of the gain-to-loss ratio r . This equation is [9]

$$I_{out} = (r - 1) \delta_e \frac{I_{sat}}{4} \quad (4.19)$$

This equation indicates that the output intensity increases linearly with increasing gain-to-loss ratio r . In semiconductor lasers, the gain is linearly proportional to the pumping current [9]. Therefore, the ratio r is a measure of how much the laser is pumped above threshold. The condition of $r = 1$ corresponds to the laser threshold point. It is important to note, however, that Eq. (4.19) is only valid for $r > 1$. For $r < 1$, the laser is below threshold and does not produce any CW output. A plot of the calculated output intensity as a function of r is shown in Figure 4.4. The plotted intensity is normalized as I_{out} / I_{sat} , and assumes $R = 0.36$.

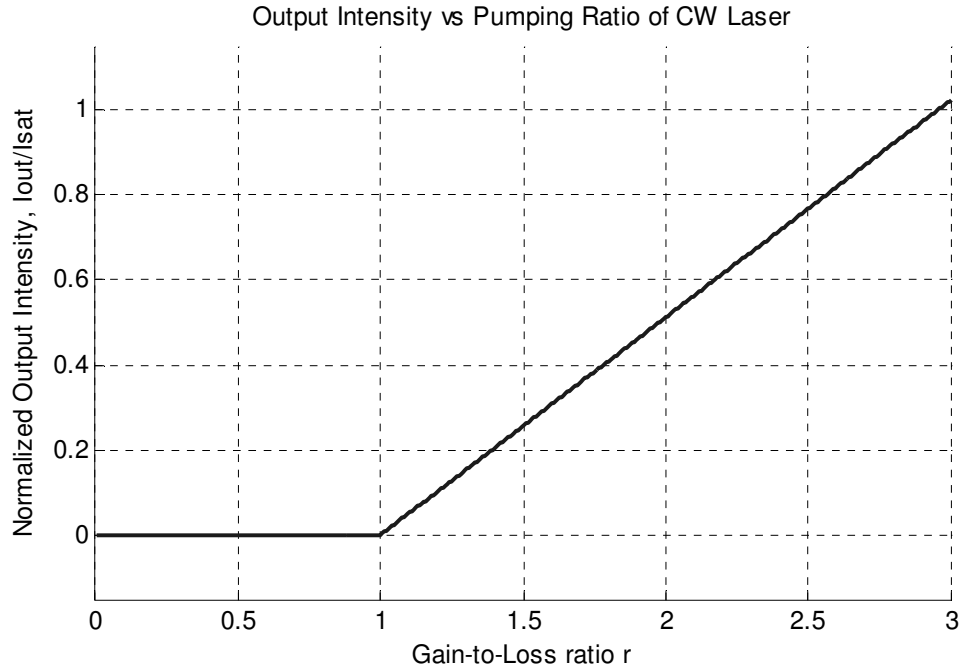


Figure 4.4: Calculated output intensity of a CW laser as a function of pumping ratio. The condition $r = 1$ corresponds to laser threshold.

In the experiment, the light power output from the fabricated laser is measured as a function of the uniform pumping current. The experimental setup is much like the setup depicted in Figure 3.11 for the passive mode-locking measurements, except all three segments of the laser are now connected to the same DC electrical current power supply. The optical power output from the laser is measured by connecting one of the optical fibers aligned with a laser facet to an optical power meter. The measured data is shown in Figure 4.5. The laser threshold occurs at a pumping current of approximately 140 mA. The experimental result agrees qualitatively with the theory. The slope of the curve above threshold depends on the saturation intensity I_{sat} of the laser. A qualitative comparison with the theory would require a model for the relationship between pumping current and unsaturated gain of the laser, as well as an accurate method for measuring cavity losses.

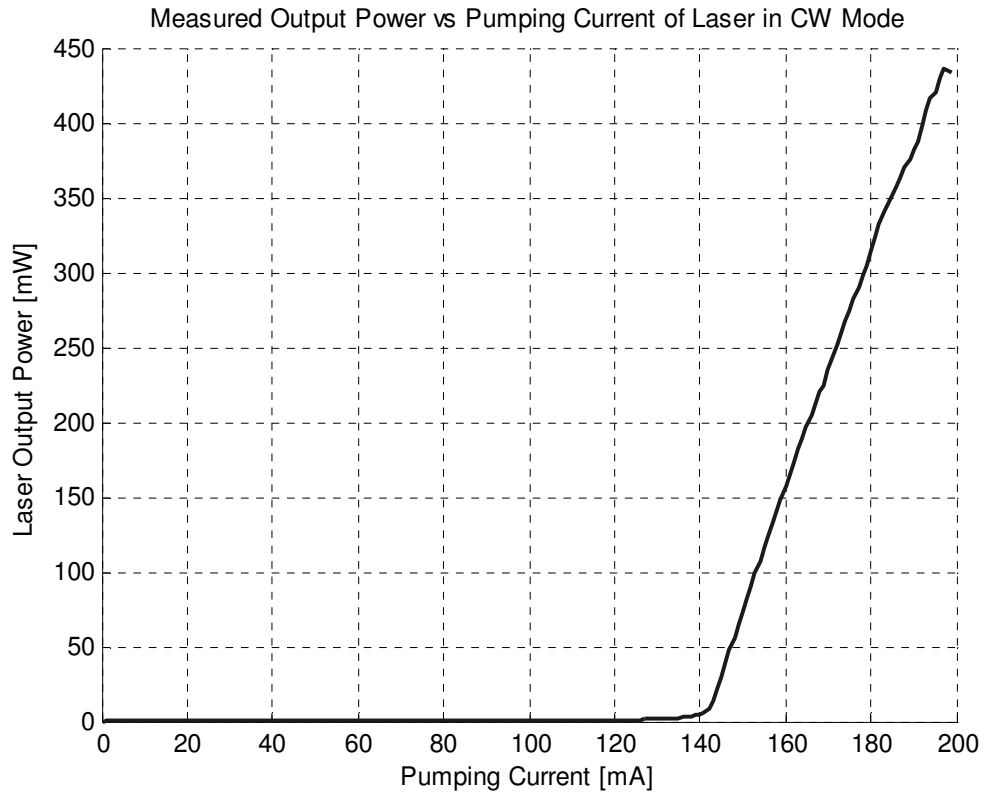


Figure 4.5: Measured optical output power of fabricated laser in CW mode as a function of uniform pumping current.

Measurement of the laser output power as a function of pumping current is an easy way to determine the threshold current of the device. Once the threshold is known, the laser can be biased to CW operation by setting the current to a level well above the threshold. In the experiment, the pumping current was varied from 180 mA to 220 mA. The CW operation was characterized by measuring the optical spectrum of the laser output. Figure 4.6 shows the optical spectrum of the laser biased with a pumping current of 208 mA. The spectrum shows a several strong spectral components, with additional weaker components. This indicates that the laser is not in single-mode operation. In general, many axial modes of the laser cavity compete

for gain. As the pumping current is varied, the measured spectrum has different peak spectral components, but the same general character.

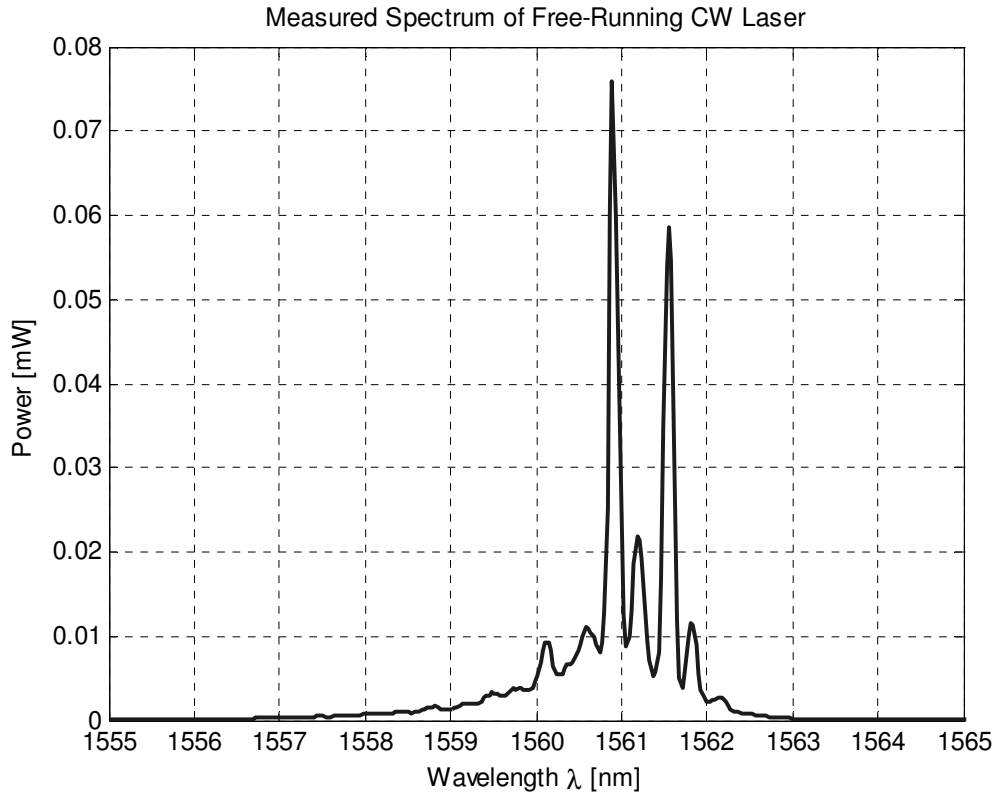


Figure 4.6: Measured optical spectrum of free-running CW laser.

To demonstrate CW injection locking, an external CW laser signal is launched into one facet of the fabricated laser. The external CW signal is generated by a Photonics Tunics 1550 laser source. The Photonics CW signal is measured directly by the optical spectrum analyzer (OSA), as shown in Figure 4.7. As expected, it has a very clean CW signal. To perform injection locking, the Photonics CW laser signal is connected to the optical fiber which is aligned with the right facet of the fabricated laser. The optical fiber aligned with the left facet of the laser is connected to the OSA.

It is important to note that earlier attempts at this experiment yielded irregular and irreproducible results. It was observed by Arun Mampazhy that this was caused by feedback from the optical fiber tips. The air gap between each laser facet and the optical fiber aligned to that facet creates an unintended additional cavity. The problem was fixed by slightly backing the fiber tips away from the laser facets. Although this resulted in less light being coupled from the laser to the fibers, and vice versa, it dramatically reduced the feedback problem.

Successful cases of CW injection locking were achieved, and the measured spectrum corresponding to one such case is shown in Figure 4.8. This was achieved with a pumping current of 207.75 mA, and is almost identical to that of the Photonetics CW laser itself. As explained earlier, CW injection locking requires that the frequency detuning between the injected laser and the free-running laser be less than some maximum locking range ω_m . Typically, the frequency ω_1 of the injected signal may be tuned until it is within the locking range. However, the Photonetics CW laser frequency was kept fixed in the experiment. Instead, the free-running frequency ω_0 of the fabricated laser was tuned by varying the effective optical length of the laser cavity. This tuning is achieved by varying the pumping current. The relationship between the pumping current and the effective cavity length was explained in Section 3.4, and is assumed to be a linear relationship [9].

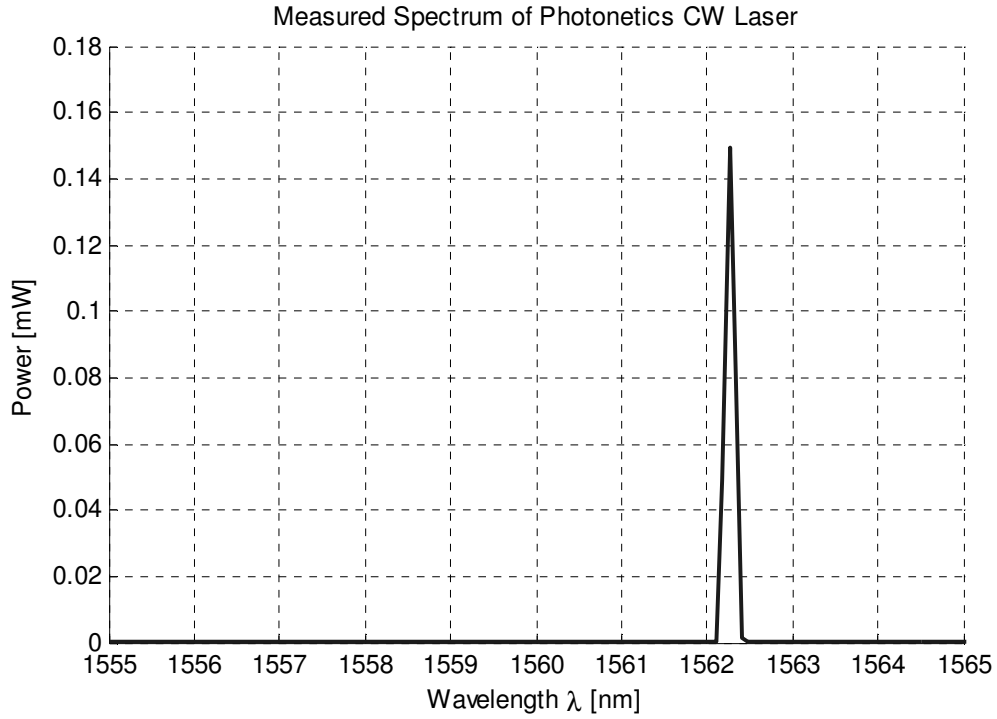


Figure 4.7: Measured optical spectrum of Photonetics CW laser signal.

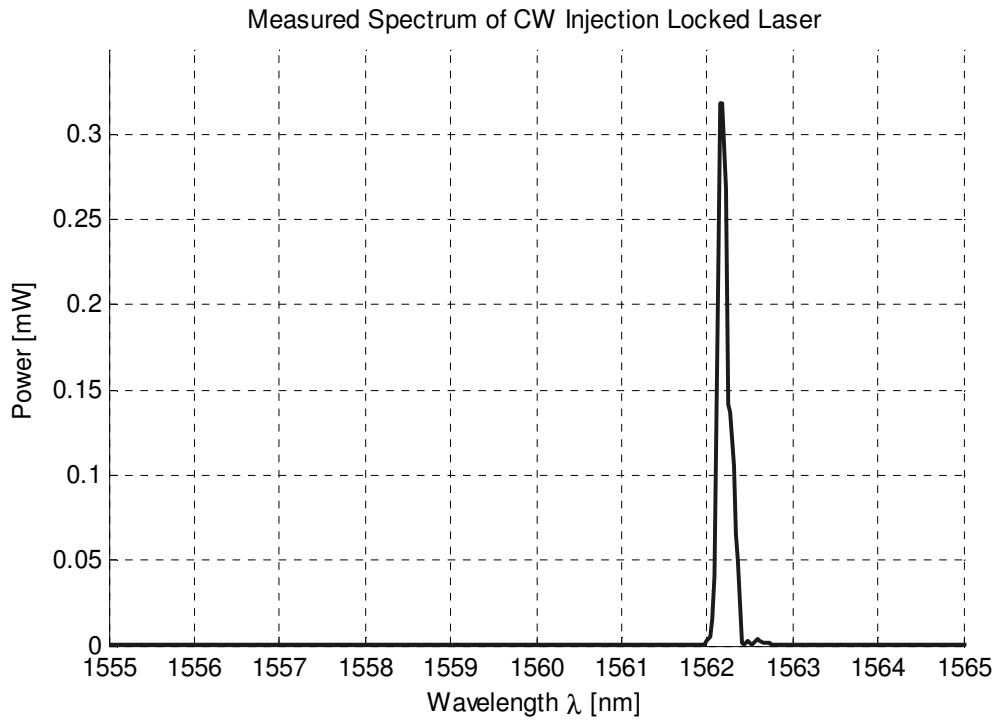


Figure 4.8: Measured optical spectrum of CW injection locked laser.

4.3 Reflected Power as a Diagnostic for CW Injection Locking

In Section 4.2, CW injection locking was achieved with the fabricated laser injection locked by an external commercial laser. Experimentally, the effective cavity length of the fabricated laser was tuned to adjust the free-running operating frequency. This varied the frequency detuning across the locking range. The optical spectrum was monitored until a clean, very narrow spectral shape was observed. This state of operation was then assumed to be CW injection locking. In practice, it is difficult to know the exact change in effective cavity length, because the quantitative relationship between the pumping current and the effective index of refraction is not directly measurable.

We propose a diagnostic for determining whether the laser is injection locked at a given pumping current. An updated version of the schematic for CW injection locking in Figure 4.1 is shown in Figure 4.9. It specifically illustrates that on the injection side of the laser, there will be two signals traveling away from the laser facet. One of the signals is the output of the fabricated laser. This output may or may not be injection locked, depending on the injected power and the frequency detuning. It was mentioned Section 4.1 that the reflected portion of the incident external CW signal would be of interest. This is the second signal which is traveling away from the laser facet on the injection side. The total optical power traveling away from the laser facet can be measured by coupling the optical fiber that carries the injected signal to a power meter. This total optical signal is a sum of the electric fields \tilde{E}_{out} of the laser and $\tilde{E}_{inc,refl}$ of the reflected incident signal.

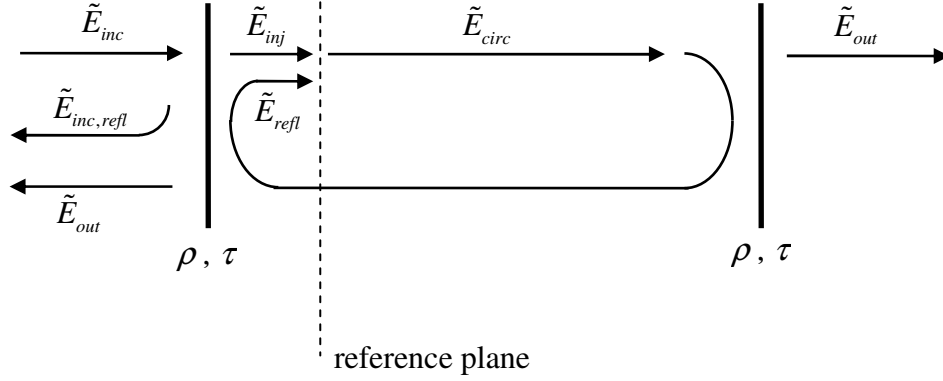


Figure 4.9: Modified schematic of model of CW injection locking.

The total electric field of the signal is simply the sum of \tilde{E}_{out} and $\tilde{E}_{inc,refl}$, so the power may be written as

$$P_{tot} = \left| \tilde{E}_{out} + \tilde{E}_{inc,refl} \right|^2 \quad (4.20)$$

The signals \tilde{E}_{out} and $\tilde{E}_{inc,refl}$ can be expressed in phasor notation as

$$\begin{aligned} \tilde{E}_{out} &= E_{out} e^{i\phi_{out}} \\ \tilde{E}_{inc,refl} &= E_{inc,refl} e^{i\phi_{inc,refl}} \end{aligned} \quad (4.21)$$

The expression for the total power can then be written as

$$P_{tot} = \left(E_{out} e^{i\phi_{out}} + E_{inc,refl} e^{i\phi_{inc,refl}} \right) \left(E_{out} e^{i\phi_{out}} + E_{inc,refl} e^{i\phi_{inc,refl}} \right)^* \quad (4.22)$$

Distributing terms,

$$P_{tot} = E_{out}^2 + E_{out} E_{inc,refl} e^{i(\phi_{out} - \phi_{inc,refl})} + E_{out} E_{inc,refl} e^{-i(\phi_{out} - \phi_{inc,refl})} + E_{inc,refl}^2 \quad (4.23)$$

The cross-terms in Eq. (4.23) simply represent a cosine of the phase difference, so the expression can be rewritten as

$$P_{tot} = E_{out}^2 + E_{inc,refl}^2 + 2E_{out} E_{inc,refl} \cos(\phi_{out} - \phi_{inc,refl}) \quad (4.24)$$

The cosine term in Eq. (4.24) indicates that the total power of the signal from the facet strongly on the phases of \tilde{E}_{out} and $\tilde{E}_{inc,refl}$. Recall that implicit in this expression is the fact that both \tilde{E}_{out} and $\tilde{E}_{inc,refl}$ are oscillating at the injected frequency ω_1 . By definition, $\tilde{E}_{inc,refl}$ is always at ω_1 . However, \tilde{E}_{out} will only be at ω_1 if the laser is injection locked. If it is not injection locked, \tilde{E}_{out} will oscillate at a frequency close to ω_0 , as explained earlier. This frequency difference would have to be included as a time variation in ϕ_{out} . In this case, the cosine term in Eq. (4.24) would be modulated at the beat frequency $|\omega_1 - \omega_0|$. If this output signal is measured on an optical power meter, the contribution from this modulation term averages out to zero. Therefore, if the laser is not injection locked, the measured total power is simply the sum of the powers of the output and reflected incident waves, as given by

$$P_{tot} = E_{out}^2 + E_{inc,refl}^2 \quad (4.25)$$

In other words, the output and reflected incident waves add incoherently if the laser is not injection locked.

The more interesting case occurs when the laser is injection locked. In this case, \tilde{E}_{out} and $\tilde{E}_{inc,refl}$ are both oscillating at ω_1 , and the cosine term in Eq. (4.24) cannot be ignored. The output and reflected incident waves add coherently. Eq. (4.24) can be expressed in terms of the circulating and injected fields inside the cavity, the same terms used in the derivation of Eq. (4.16) in Section 3.3.1. The output field amplitude E_{out} is simply the circulating field amplitude E multiplied by the amplitude of the facet transmission coefficient $|\tau|$. The amplitude of the reflected

incident wave is, by definition, equal to the incident amplitude E_{inc} multiplied by the facet reflection coefficient $|\rho|$. The injected wave amplitude E_1 is equal to E_{inc} multiplied by the transmission coefficient $|\tau|$. While the various amplitudes are related to each other through $|\rho|$ and $|\tau|$ as they reflect or transmit through the cavity facet, the actual fields also experience a phase shift upon reflection and transmission. The difference between the reflection phase shift and the transmission phase shift is $\pi/2$. By convention, the reflection coefficient is taken to have a zero phase shift, such that $\rho = |\rho|$. Therefore, the transmission coefficient is taken to have a $\pi/2$ phase shift, such that $\tau = |\tau|e^{i\pi/2}$ [9]. As a result, the relationships between the phase of the incident wave ϕ_{inc} and the phase of the injected wave ϕ_1 , as well as between the phase of the output wave ϕ_{out} and the phase of the circulating wave ϕ , are

$$\begin{aligned}\phi_1 &= \phi_{inc} + \pi/2 \\ \phi_{out} &= \phi + \pi/2\end{aligned}\tag{4.26}$$

These amplitude and phase relationships can be used to translate Eq. (4.24) to

$$P_{tot} = T E^2 + \frac{R}{T} E_1^2 - 2\sqrt{R} E E_1 \cos(\phi - \phi_1)\tag{4.27}$$

where we have used the identity $\cos(\phi - \phi_1 + \pi) = -\cos(\phi - \phi_1)$.

Therefore, the coherent interference between the reflected incident wave and the output wave results in a reduction of power compared to the incoherent case. This destructive interference comes from the two $\pi/2$ phase shifts experienced upon transmission from \tilde{E}_{inc} to \tilde{E}_{inj} and from \tilde{E}_{circ} to \tilde{E}_{out} . The amount of interference depends on the phase difference $\phi - \phi_1$, which is known to depend on the frequency

detuning $\omega_0 - \omega_1$ between the injected wave and free-running laser. The total power output as a function of $\omega_0 - \omega_1$ is shown in Figure 4.10 for several values of the power ratio $P_{inc,refl} / P_{out}$, where $P_{inc,refl}$ is the power of the reflected incident wave and P_{out} is the output power of the free-running laser in the absence of injection. In Figure 4.10, the total power output is normalized to the incoherent total power, which is simply the sum of the powers of the reflected incident wave and laser output wave. Therefore, a value of 1 on the normalized power axis corresponds to the full total power if the laser was not injection locked. For each value of the power ratio, the curve is plotted over the full locking range corresponding to that power ratio. As expected, larger power ratios have wider locking ranges. Since the all the equations presented only apply to frequency detunings within the locking range, no values are plotted which correspond to points outside the locking ranges.

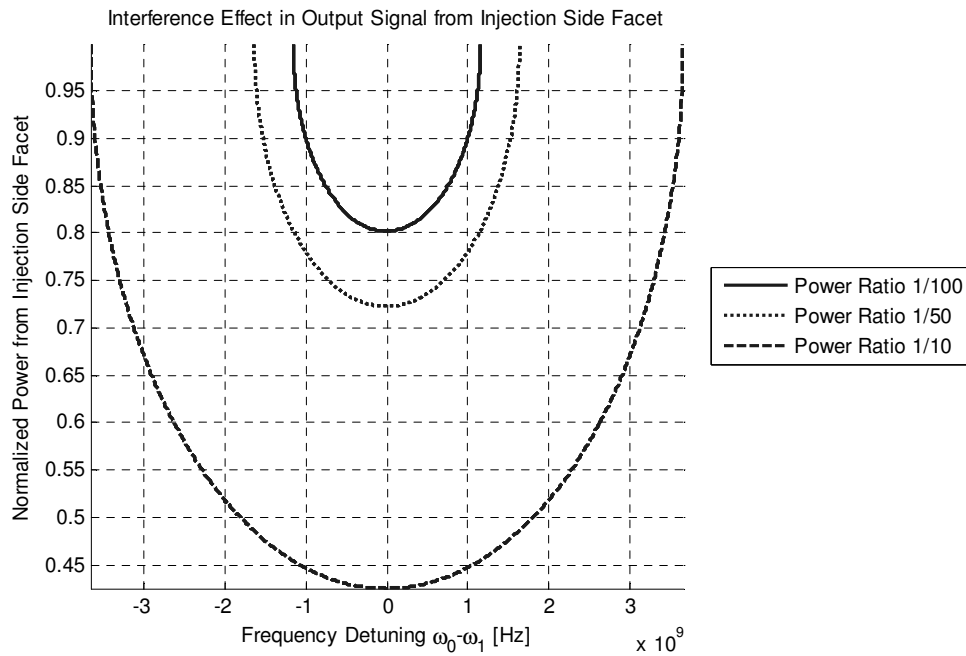


Figure 4.10: Total output power from injection side facet of laser, when injection locking is achieved.

Outside the locking range, the normalized power should equal 1, assuming no interference effects occur for the unlocked laser. However, the theory for the laser outside the locking range is not treated here. The calculated results show that for a power ratio of 1/10, the total power output is reduced to a minimum of 42.5% of the incoherent level at a detuning of zero. For a power ratio of 1/100, the power is reduced to a minimum of 80.2% of the incoherent level.

The destructive interference effect experienced by the output wave on the injection side of the laser is used as a diagnostic for injection locking. As indicated by Eq. (4.27) and Figure 4.10, the strength of the interference depends on the frequency detuning. In particular, the interference is strongest at zero detuning. In the experiment, as explained, the effective cavity length of the laser is tuned by varying the pumping current. This shifts all the axial modes ω_q of the laser cavity. As the current continues to be varied, one of the modes ω_q becomes tuned close enough to ω_l such that the difference between the two becomes less than the locking range ω_m . Therefore, any of the cavity modes has the potential to serve as the frequency ω_0 so long as the cavity length is adjusted to shift the modes.

The power from the injection side of the laser, which travels in the same optical fiber that carries the injection signal, is coupled to a power meter. The total output power is measured for different power ratios $P_{inc,refl} / P_{out}$. The power of the reflected incident wave $P_{inc,refl}$ is measured by turning off the pumping current of the laser. With the laser below threshold, no output is produced and the cavity facet acts as a simple mirror. The output power P_{out} of the laser itself is measured by turning

off the external injection laser. With both the laser and the injection source turned on, the current is varied from 180 mA to 230 mA, and the total power is measured. The result for a power ratio $P_{inc,refl}/P_{out}$ of 1/10 is shown in Figure 4.11, and for a ratio of 1/100 in Figure 4.12.

The measured results have qualitative similarities and differences compared to the theory. The measured output power demonstrates the interference effect predicted by theory, as the power decreases to a minimum each time the free-running laser frequency ω_0 is tuned close enough to the injected frequency ω_1 . The current range from 180 mA to 230 mA is sufficient to tune three axial modes of the laser through ω_1 . For a power ratio of 1/10, the power is reduced to about 32% of the incoherent level, while for a ratio of 1/100, the power is reduced to about 78% of the incoherent level. This is reasonably consistent with the theory, at least such that the depth of the power reduction is much deeper for a higher power ratio. The width of the power reduction dip is much wider for the higher power ratio, which also agrees qualitatively with theory. However, the shape of the power reduction dip is asymmetric. This is especially noticeable in the case of the higher power ratio. This is due to effects not included in the theoretical treatment. A possible cause is the linedwidth enhancement factor α_H , which couples the gain and phase response of the laser medium. Finally, the overall incoherent power level increases as the pumping current is increased. This is simply due to the fact that while increasing the current performs the task of tuning the axial modes, it also has the effect of increasing the unsaturated gain and therefore the gain-to-loss ratio r of the laser. This was illustrated in Figure 4.4 and Figure 4.5.

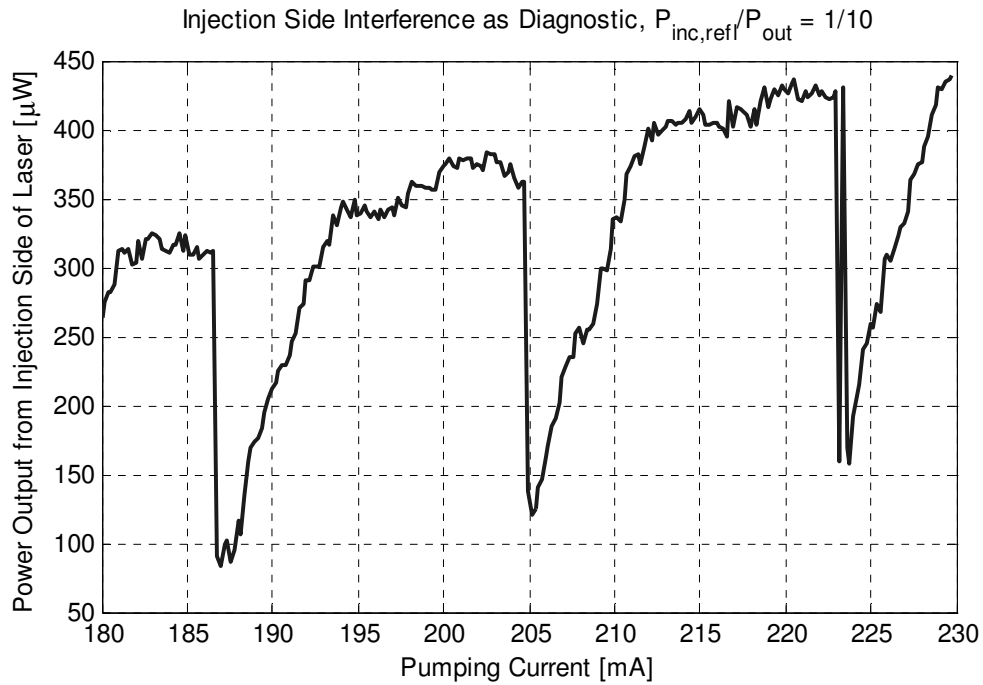


Figure 4.11: Measured total power from injection side of laser, as pumping current is tuned, for power ratio of 1/10.

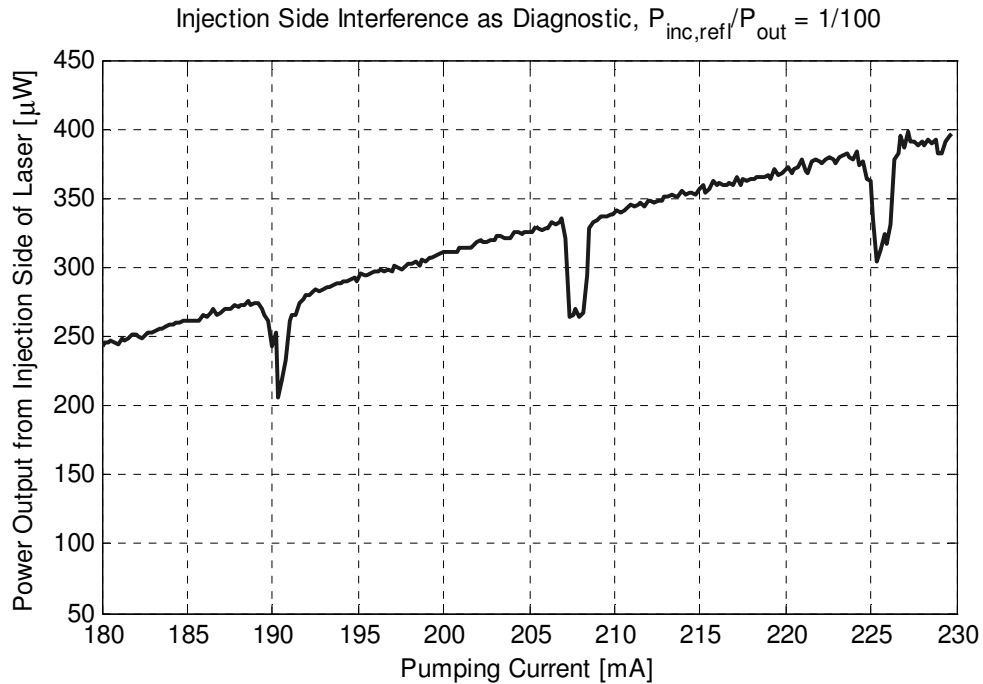


Figure 4.12: Measured total power from injection side of laser, as pumping current is tuned, for power ratio of 1/100.

In summary, this section introduces a useful diagnostic for determining whether a laser system is coherently injection locked. If the circulating laser's signal is coherently locked to the injection signal, the theory predicts that coherent interference must occur between the reflected portion of the incident signal and the output of the laser from the injection side. In the regime of coherent injection locking, this interference is unavoidable because it arises from the natural $\pi/2$ phase shift that a wave experiences as it transmits through a laser facet. The useful, non-interfered output of the laser must be taken from the other facet.

Chapter 5: Pulsed Coherent Injection Locking of a Mode-locked Laser

5.1 Description of Pulsed Coherent Injection Locking of a Mode-locked Laser

The previous chapters described mode-locking and injection locking of lasers. The basic theories for both of these regimes of laser operation are well understood, and a simple review was presented. This chapter describes a different method of laser operation which attempts to combine mode-locking and injection locking. This technique has not been widely studied, and the theory is not well understood. A description of the proposed method is given in terms of the concepts developed for mode-locking and injection locking. Strictly, these concepts apply to lasers with linear gain characteristics. The real laser system under investigation is highly nonlinear. For example, the round trip time depends not only on pulse intensity but also on pulse shape. However, the theoretical framework is nonetheless useful in understanding the laser system. Experimental results are presented and discussed. A rudimentary numerical model was developed in an attempt to explain the experimental results. The model shows qualitative support for some aspects of the experimental results. Recommendations for future work are provided.

In pulsed injection locking of a mode-locked laser, a pulse train produced by an external laser is injected into an already mode-locked laser. This is similar in some aspects to active or hybrid mode-locking schemes which employ optically-driven modulation of the laser. Active mode-locking was briefly described in Section 3.2.

In active mode-locking, because the injection and laser signals take the form of pulse trains, the spectra consist of many equally spaced axial modes. It is important to note that this description of the laser spectra assumes that the laser is a linear device. In such active mode-locking schemes with optically-driven modulation, the spectral range of the injection signal is chosen to lie far from that of the free-running mode-locked laser. Therefore, there is no coherent interaction between the injection and mode-locked signals. The injected signal only functions to lock the axial mode spacing $\Delta\omega_{ax}$, and therefore the repetition rate, of the mode-locked laser. The injected signal, which has a set RF repetition rate ω_m , modulates the gain of the laser at that rate. As mentioned in Section 3.2, this modulation causes the axial modes ω_q of the free-running laser to acquire sidebands at frequencies $\omega_n = \omega_q \pm n\omega_m$. If the modulation frequency ω_m is exactly or very closely equal to the free-running axial mode spacing $\Delta\omega_{ax}$, the sidebands ω_n of a given axial mode will lie exactly on or very closely to the neighboring free-running axial modes ω_{q-n} and ω_{q+n} . If the detuning between ω_m and $\Delta\omega_{ax}$ is small enough, then the modulation-induced sidebands will injection lock the neighboring free-running axial modes, in a process much like CW injection locking. This locks the axial mode spacing $\Delta\omega_{ax}$ of the laser to the RF frequency ω_m of the injection signal. This process is illustrated in Figure 5.1. It is important to note that although the sidebands are induced by the injection signal, their phases do not depend on the injection. In standard active mode-locking, the goal is to produce a pulsed signal with a fixed repetition rate.

Pulsed coherent injection locking differs from optically-driven active mode-locking in that it uses an injection signal whose spectral range is purposefully chosen to overlap with that of the free-running laser. This is illustrated in Figure 5.2. In this case, the modes of the injected signal themselves may, under proper conditions, injection lock the free-running axial modes of the laser. Therefore, not only does the repetition rate of the laser become locked to that of the injection signal, but the phases of the laser axial modes depend directly on the phases of the injected signal modes. Consider an injection signal that possesses modes with a very well-defined phase relationship. The mode-locked laser will obtain this desirable phase relationship through the injection locking process. Thus, the proposed method aims to achieve both mode-locking and coherent injection locking of a free-running laser using a high quality mode-locked injection signal.

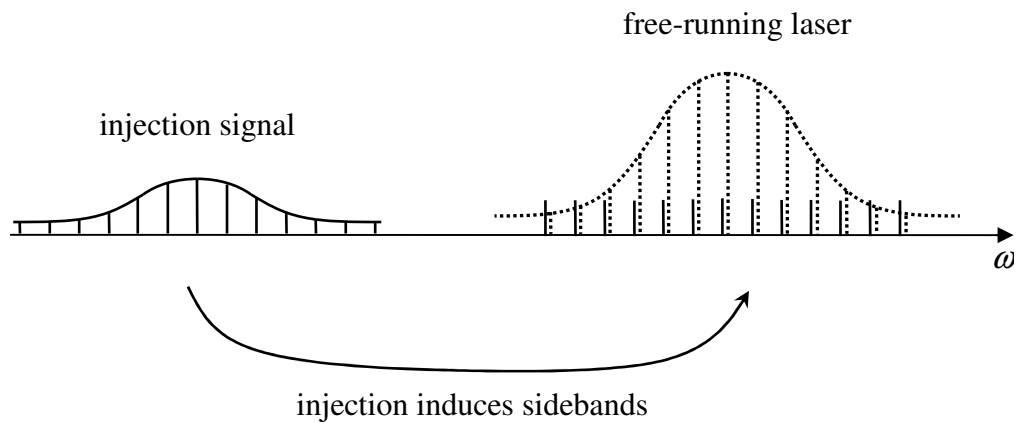


Figure 5.1: Diagram illustrating optically-driven active or hybrid mode-locking.

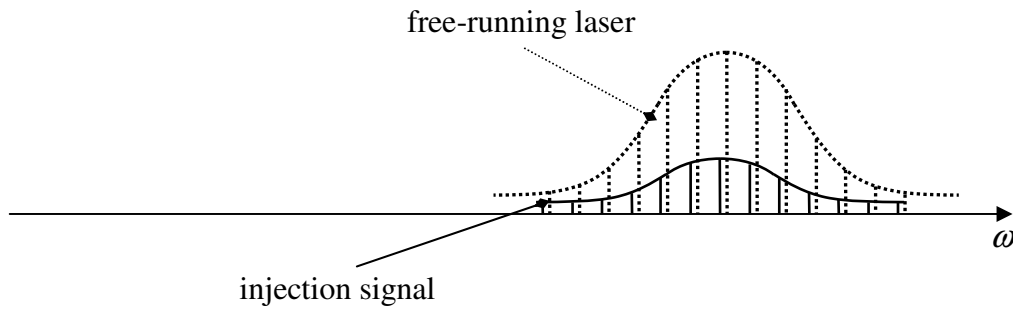


Figure 5.2: Diagram illustrating pulsed coherent injection locking.

Pulsed coherent injection locking of a mode-locked laser requires that two criteria be met. First, the detuning between the injection laser repetition rate and the free-running laser repetition rate must be small enough such that active mode-locking occurs. In other words, the mode spacing ω_m of the injected signal must be close enough to the mode spacing $\Delta\omega_{ax}$ of the free-running laser. This is the same requirement as for standard active mode-locking. Second, the actual locations of the injected modes in frequency must lie very close to the locations of the free-running axial modes. This is the same requirement as for CW injection locking. In order to achieve pulsed injection locking of a mode-locked laser, the characteristics of the injection signal or the free-running laser must be adjusted to meet these criteria.

It is important to note that the pulsed coherent injection locking method involves using a free-running laser which is already mode-locked by passive mode-locking techniques. The passively mode-locked laser utilizes the nonlinearity of the saturable gain and saturable absorber sections. In the presence of the strong nonlinearity, the axial modes of the free-running laser are not as simply defined as in the case of a linear system. The round-trip time T_{RT} of the laser pulse circulating in

the laser does not simply depend on the cavity length and the index of refraction of the medium. The nonlinearities cause the effective refractive index to change rapidly in time. Pulse reshaping due to the saturable gain and absorption changes the effective round-trip time in a way which is difficult to quantify. As a result, the repetition rate also depends on the saturation dynamics in a complicated way [15]. Therefore, the so-called axial modes of the free-running laser exist only in steady state operation, and are determined by a complicated process.

5.2 Experimental Setup

The pulsed injection locking concept is experimentally investigated using the monolithic passively mode-locked SCPM laser described in Section 3.4 and the commercial mode-locked (ML) laser used in the optical switching experiment described in Chapter 2. The experiment is designed to satisfy the two criteria for pulsed injection locking of a mode-locked laser, as described in Section 5.1. A detailed description of the experimental setup is provided in this section.

Essentially, the experiment attempts to produce the situation depicted in Figure 5.2. The same commercial ML laser described in Chapter 2 is used as the injection signal. It is assumed that this laser has a well-defined mode spacing and a constant phase relationship across its modes. The ML laser signal is injected into the passively mode-locked SCPM laser described in Chapter 3. In the experiment, the operating conditions of the ML laser are kept unchanging. The injection signal therefore has a constant repetition rate and a constant axial mode placement. Rather, the SCPM laser cavity is tuned by varying the pumping current. This shifts the axial

The experimental setup is depicted in Figure 5.3. The commercial mode-locked laser is set to produce a pulse train with a repetition frequency of 10.84 GHz, with pulses centered in spectrum around 1562 nm and pulse widths of about 2.77 ps FWHM. The pulse train is sent through an optical isolator (not shown in the schematic) to prevent unintended reflections from damaging the commercial ML laser. The pulse train is then amplified with an Erbium doped fiber amplifier (EDFA, #1), and the amplified signal is filtered with a 3.0 nm FWHM band-pass filter (BPF) to remove amplified spontaneous emission (ASE) due to the EDFA. The amplified pulse train is split with a 50/50 splitter. One branch is used as the reference signal for the cross correlator (CORR), in the same manner described in Section 2.4.2. The other branch serves as the injection signal for the injection locking experiment. The injection signal is launched into an HP 8156A variable optical attenuator (ATT). The attenuator is used to control the power level of the injection signal. The signal is then passed through a polarization controller (PC) which allows the state of polarization of the injection signal to be adjusted. The attenuated, polarization-controlled injection signal is then launched into port 1 of the 50/50 coupler, as shown in Figure 5.3.

The SCPM laser is set up in the same manner as for the passive mode-locking experiment, which is depicted in Figure 3.11. The saturable absorber side of the SCPM laser was chosen as the input side, because preliminary work performed by Arun Mampazhy showed that this choice yielded more stable operation. Therefore, the injection signal from port 3 of the 50/50 coupler is connected to the optical fiber that is aligned with the absorber side of the SCPM laser. In Figure 3.11, this is the right side of the laser. The signal from port 3 is simply the injection signal launched

into port 1 attenuated by 3 dB. The optical fiber aligned to the absorber side of the laser also captures the portion of the injection signal that is reflected by the laser facet. This reflection signal necessarily launches back into port 3 of the 50/50 coupler, and is attenuated by 3 dB as it is coupled to port 2 of the coupler. Port 4 of the coupler is terminated by connecting to a fiber jumper with an angled end connector. This prevents unintended reflections from the unused port of the coupler. The resulting reflection signal out of port 2 is used to monitor the injection signal in two ways. First, it may be launched into an HP 8153A lightwave multimeter, or optical power meter (POW), to measure the power of the interfered reflection signal. This is the reflected power diagnostic described in Section 4.3. Second, it may be sent to an Agilent 8509B Lightwave Polarization Analyzer (POL) to monitor the state of polarization of the injection signal. In the absence of an injection signal, the POW and POL can be used to measure the power and state of polarization of the free-running SCPM laser itself.

It is important to note that earlier experiments yielded unreliable results. The cause was discovered by Arun Mampazhy to be unintended reflections experienced at the optical fiber tips. The air gap formed between each optical fiber and the laser facet to which it is aligned acts as a cavity. To minimize this undesirable effect, we slightly back the optical fibers away from the laser facets. This results in less power being coupled between the fibers and the laser. However, it is necessary to prevent the unintended reflections from disrupting the coherent locking process.

The facet at the gain side of the SCPM laser is used as the output side. The output signal from the SCPM is monitored in three ways. In Figure 3.11, this is the

right side of the laser. This output is launched through a 50/50 splitter, with one branch sent to the CORR so that the signal may be cross correlated with the ML reference signal. This branch is amplified by EDFA #2 to provide a signal strong enough for the CORR to use. The second branch of the output signal is sent through another 50/50 splitter, so the resulting branches can be simultaneously monitored by an optical spectrum analyzer (OSA) and a radio frequency (RF) spectrum analyzer (RFSA).

The pulsed injection locking experiment is performed at two power levels of the injection signal. For high power injection, the reflected injection signal measured at the power meter (POW) was $15.5 \mu\text{W}$, and required an attenuator (ATT) setting of 3 dB attenuation. For low power injection, the reflected injection signal was measured to be $1.6 \mu\text{W}$, and required an ATT setting of 12 dB attenuation. For these measurements, the SCPM laser was turned off. In this case, the measured power comes only from the reflected injection signal. The reflected injection power is then compared to that of the free-running SCPM laser, which was measured to be about $150 \mu\text{W}$ at a low gain section current of $I_{LG} = 200\text{mA}$. This was measured by biasing the SCPM laser at optimal conditions of $I_{HG} = 60\text{mA}$ and $V_{SA} = -2.2\text{V}$ and disabling the attenuator (ATT), which completely blocks the injection signal from launching into the 50/50 coupler. Therefore, the high power injection case corresponds to an injection of about 1/10 the free running power, while the low power injection case corresponds to an injection of about 1/100 the free running power. It is important to note that these are estimated power ratios, because as the low gain

section current is increased to tune the cavity, the free running SCPM power also increases up to about 230 μW .

In order to attempt the pulsed injection locking method, the polarization of the injection signal must be matched to that of the free-running laser. In all of the previous discussions on gain and saturation dynamics, mode-locking, and injection locking, it was implied that the interacting signals in the laser were of the same state of polarization. To match the polarizations, the SCPM laser is operated at the optimal bias conditions and $I_{LG} = 200\text{ mA}$. Then, Port 2 of the 50/50 coupler is attached to the polarization analyzer (POL). The polarization of the free-running signal is measured with the injection signal disconnected by disabling the attenuator (ATT). Then, the SCPM laser is turned off by reducing I_{LG} to 0 mA, which ensures that the SCPM laser is unable to produce an output. The ATT is switched on, enabling the POL to detect the polarization of the injection signal. The polarization controller (PC) between the ATT and the coupler is adjusted to match the polarization of the injection signal to that of the free-running SCPM output. Afterwards, Port 2 of the 50/50 coupler is disconnected from the POL and reconnected to the power meter (POW). Although the action of connecting Port 2 to the POW requires disturbing the optical fiber connected to Port 2, the fiber between the PC and Port 1 of the coupler is not disturbed. Therefore, the polarization of the injection signal is still matched to that of the free-running laser. The polarization of the signal seen by the POW will not match that which was measured by the POL, but this is of no consequence.

5.3 Experimental Results

With the experimental setup fully described, the measured results are presented. It was noted that the actual laser is highly nonlinear, and therefore the theoretical description involving mode-locking and injection locking is not strictly applicable. Nonetheless, the measured results show several qualitative similarities with the theory. The reflected power diagnostic described in Section 4.3 is attempted with the pulsed injection locked laser, and remarkably, reduced power dips are indeed observed. We assume this to be an indication that coherent injection locking is occurring. In addition, the pulsed injection locked laser output is characterized by measuring its RF spectrum, optical spectrum, and cross-correlation trace. The measured optical spectrum in particular is noted for its unexpected behavior. The spectrum appears to shift its peak frequency across the free-running laser spectral range as the cavity length is tuned across the coherent injection locking range. The measured RF spectrum is used as an indication of whether the SCPM laser is actively mode-locked by the injection. The RF locking range is wider than the injection locking range, which indicates that, as expected, active mode-locking is easier to achieve than coherent injection locking. However, the laser is not actively mode-locked across the entire cavity tuning range. Finally, cross-correlation traces of the output were measured. Although no theory is available to predict the characteristics of the injection locked pulses in time, the measurements provide a useful examination of the system.

Following the setup described in Section 5.2, including verification of the power ratio and polarization matching, the pumping current of the low-gain section

I_{LG} is varied from 200 mA to 240 mA. At each value of I_{LG} , the optical spectrum, RF spectrum, and the reflected power value are measured. These data are recorded automatically with the aid of LabView software. The cross-correlation measurements are made after the first sweep across the pumping current range is completed. Unfortunately, the cross-correlation must be measured separately, under manual control, because the CORR requires a long averaging time and does not lend itself easily to automated control.

The results for the reflected power are shown in Figure 5.4 for a power ratio of 1/10 and in Figure 5.5 for a power ratio of 1/100. The reflected power behaves similarly to the case of CW injection locking discussed in Section 4.3. As the pumping current is varied, the axial modes of the SCPM laser are shifted. When the modes of the SCPM laser are tuned across the modes of the injection laser, destructive interference occurs and the total power is reduced. The power is reduced to about 68% of the incoherent level for a power ratio of 1/10. However, for a power ratio of 1/100, the power is only reduced to about 93% of the incoherent level. The relatively weak interference indicates that it would be difficult to use the reduced power diagnostic for low injection powers.

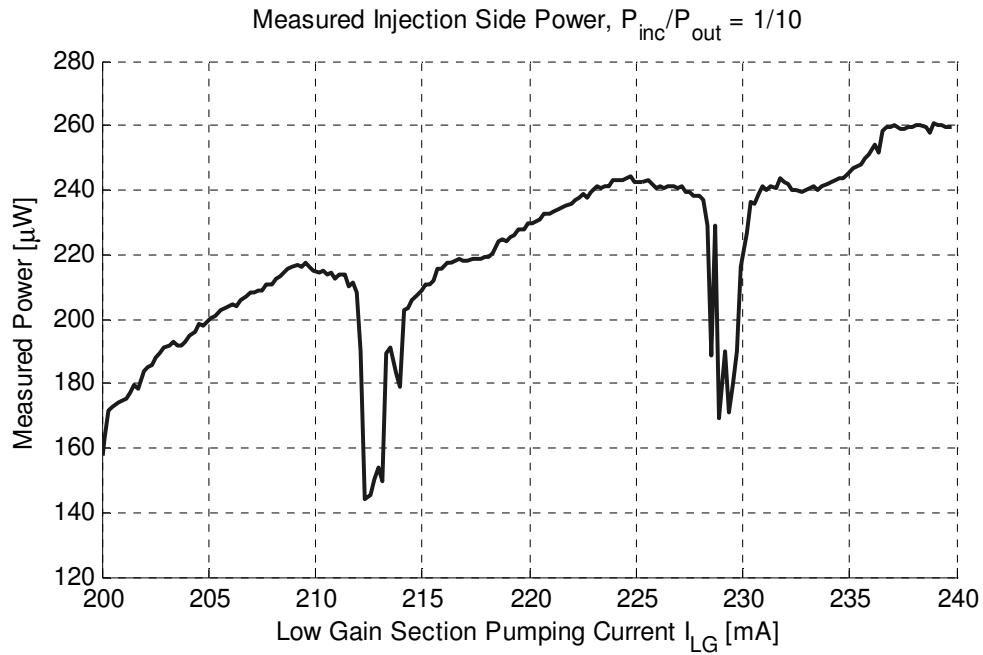


Figure 5.4: Measured injection side interfered power as a function of low-gain section current I_{LG} , for a power ratio of $P_{inc}/P_{out} = 1/10$.

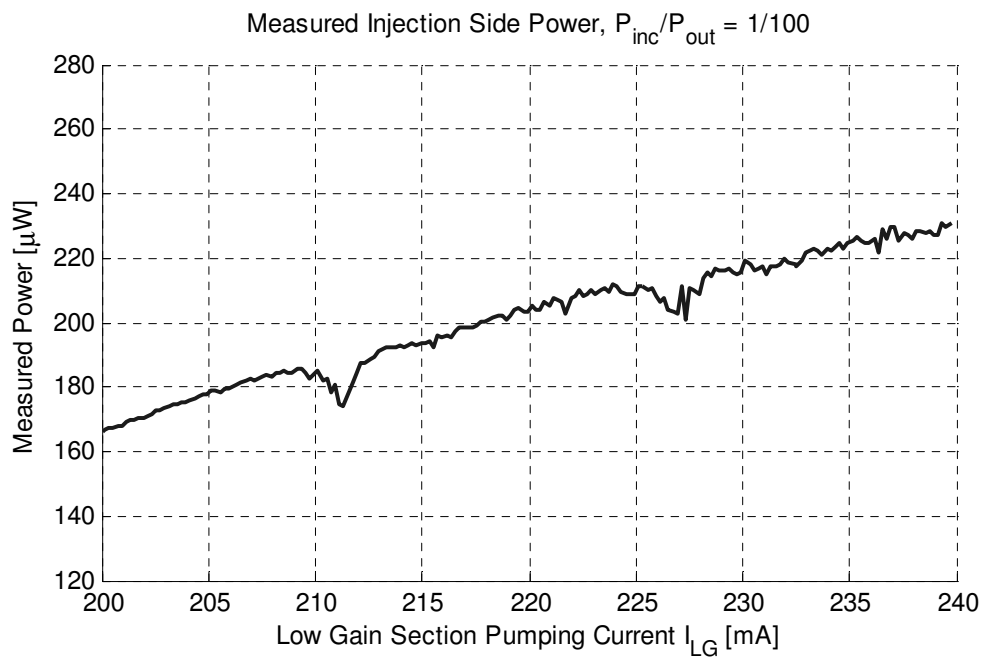


Figure 5.5: Measured injection side interfered power as a function of low-gain section current I_{LG} , for a power ratio of $P_{inc}/P_{out} = 1/10$.

The pulsed injection locking operation is characterized by measuring the RF spectrum, optical spectrum, and cross-correlation of the laser output. Here, the output of interest is the signal emitted from the low-gain side of the laser. This output signal does not experience any interference because there is no injection signal on this side of the laser. First, the RF spectrum is examined to determine the region in which the laser is RF locked. It is found that RF locking is relatively easy to obtain. Examples of locked and unlocked RF spectra are shown. For the RF spectra, the high power and low power data are essentially identical. Then, the behavior of coherent injection locking is investigated by examining the optical spectrum and cross-correlation traces. The output is especially examined for pumping currents that correspond to the reduction in power on the injection side, because these are the currents for which we assume coherent injection occurs. As in the CW injection locking case, we assume the coherent locking range of the laser corresponds to the region of currents for which there is a reduction in power. The optical spectrum and cross-correlation measurements for the case of high power injection are examined first. Then, the measurements for low power injection are presented.

In general, the RF spectrum describes the repetition rate of the signal. The typical RF spectrum of the free-running SCPM laser was discussed in Section 3.4 and shown in Figure 3.13. It was demonstrated that the repetition frequency of the free-running laser tuned with pumping current I_{LG} , and varied from about 10.855 GHz at $I_{LG} = 200$ mA to about 10.836 GHz at $I_{LG} = 240$ mA. The repetition frequency of the injection signal is chosen to be 10.84 GHz. Therefore, the repetition rate of the

free-running laser was greater than that of the injection signal, at least for most of the current range.

In the pulsed injection locking operation, the repetition rate of the SCPM laser is observed to lock to that of the injection signal over a range of currents which includes, and exceeds, the range of the reflected power dips. The dependence of the RF locking on the optical detuning, just like the power reduction diagnostic, is a complicated process. Essentially, it is an optically-driven active mode-locking process. However, it is complicated in this case by the possible coherent interaction between the injected signal and the circulating laser pulses. The reflected power curves are reproduced in Figure 5.6 and Figure 5.7, for power ratios of 1/10 and 1/100, respectively. In these new plots, the curves are marked to show the range over which RF locking occurs. In the high power injection case, this range is actually wider than the range of the reflected power dips, which we assume corresponds to optical injection locking. Note that for the chosen current ranges, the corresponding free-running repetition frequency was greater than 10.846 GHz. Therefore, for the plotted current ranges, the free-running SCPM repetition rate was always greater than that of the injection signal.

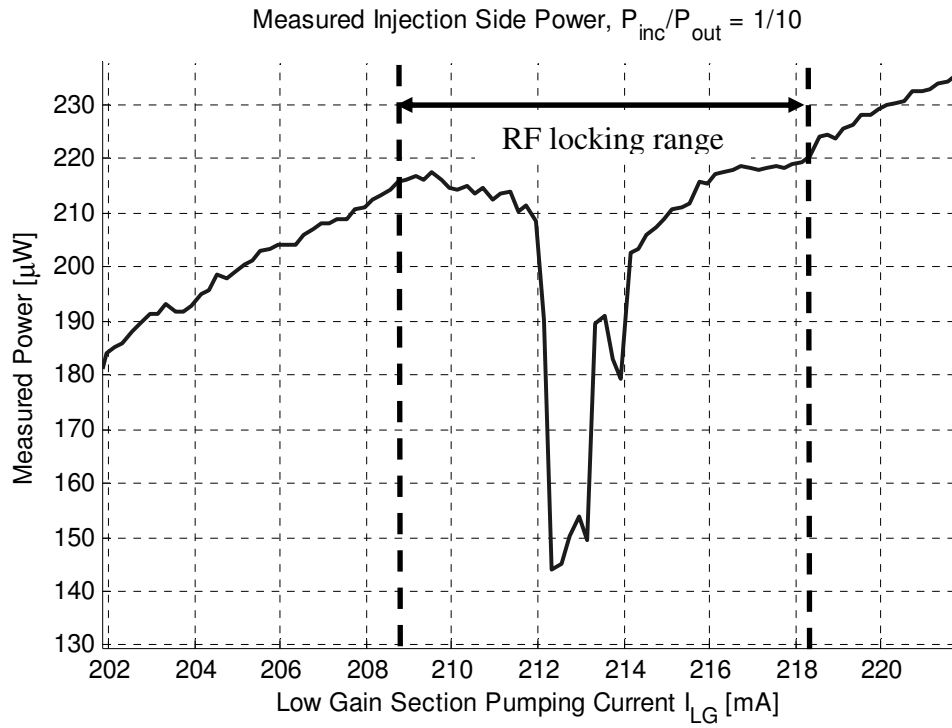


Figure 5.6: Reflected power curve for a power ratio of 1/10. The range over which RF locking occurs is marked.

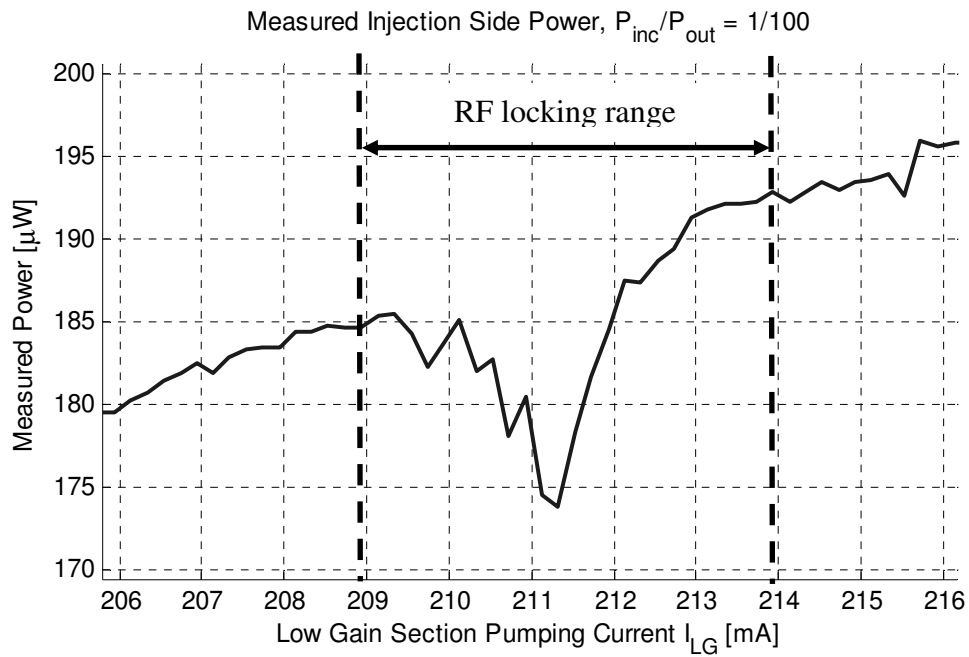


Figure 5.7: Reflected power curve for a power ratio of 1/100. The range over which RF locking occurs is marked.

An example of the RF spectrum of the pulsed injection locked laser is shown in Figure 5.8 when the laser is RF locked. The locked spectrum has a clean, sharp structure and is clearly locked to the injection repetition rate of 10.84 GHz. The RF spectrum of the injection laser itself is also plotted for comparison. An example of the RF spectrum when the laser is not RF locked is shown in Figure 5.9. The unlocked RF spectrum exhibits weak sidebands, one of which coincides with the injected repetition rate of 10.84 GHz. This indicates that even when unlocked, the injected signal is still present to some degree in the output of the SCPM laser. The measured spectra in both Figure 5.8 and Figure 5.9 correspond to the case of low injection power. However, the case of high injection power is quite similar.

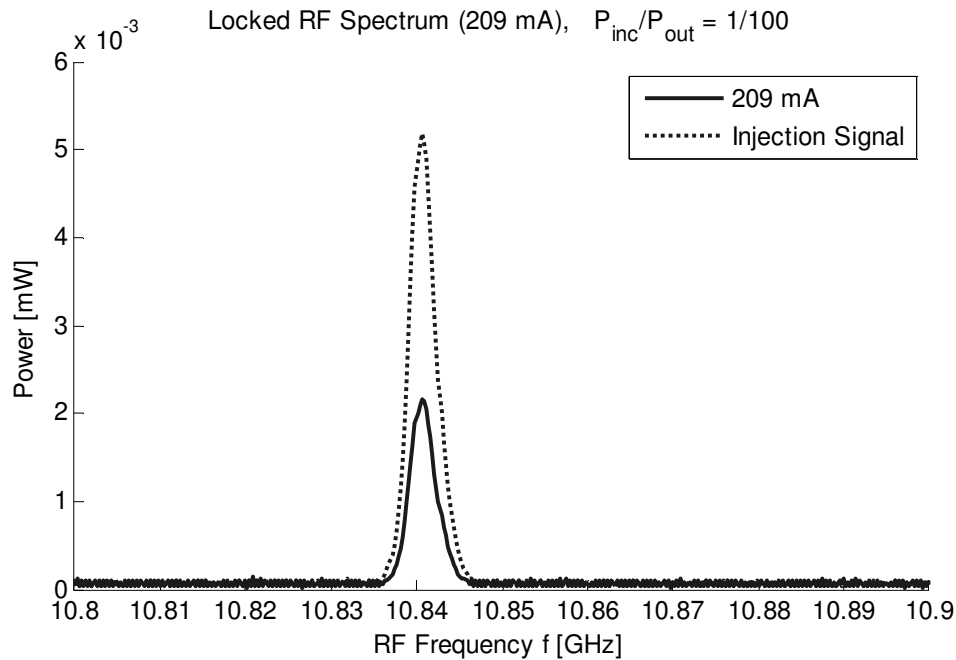


Figure 5.8: RF spectrum of pulsed injection locked SCPM laser, under bias condition such that it is RF locked to the injection laser.

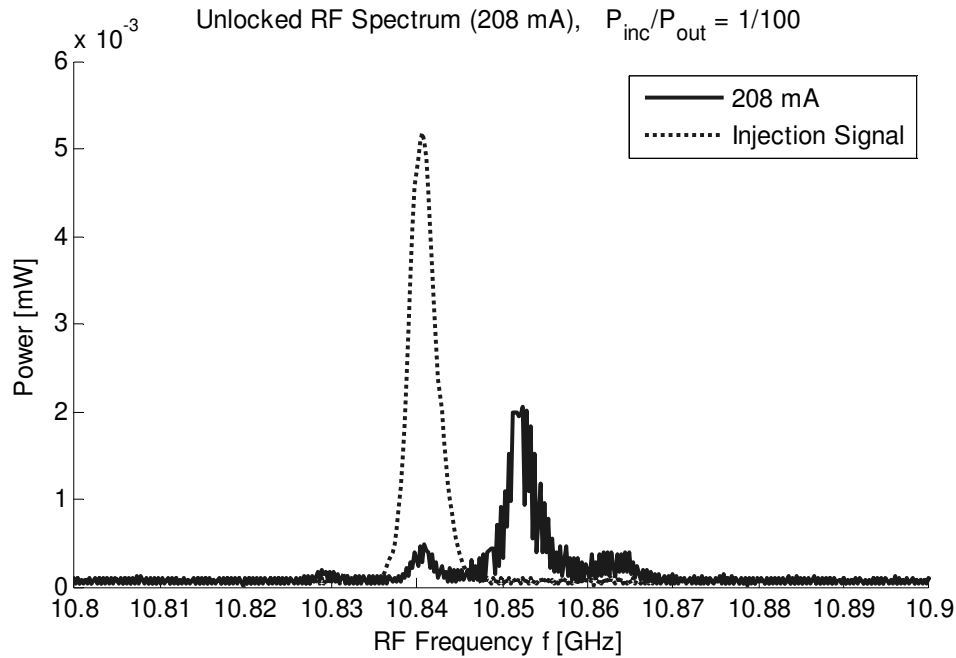


Figure 5.9: RF spectrum of pulsed injection locked SCPM laser, under bias condition such that it is not RF locked to the injection laser.

To investigate the pulsed coherent injection locking process, the optical spectrum is examined as the pumping current is varied. In the case of high power injection, the optical spectrum exhibits a clear shifting behavior. As the axial modes of the SCPM laser are swept across the coherent locking range, the output optical spectrum shifts first to higher wavelengths, then enters an unstable region of operation, then shifts to lower wavelengths. Outside of the locking range, the optical spectrum is essentially the same as that of the free-running SCPM laser in the absence of an injection signal.

To demonstrate this behavior, several instances of the optical spectrum are presented. To illustrate the behavior of the spectra in relation to the locking range, the first coherent locking region of the reflected power curve from Figure 5.4 is plotted again in Figure 5.10, with labels to indicate the currents at which the selected

spectra were measured. In Figure 5.11, the optical spectrum is plotted for a current of 211 mA, which corresponds to a point outside the coherent locking range. It is labeled point A in Figure 5.10. The spectrum is plotted along with the free-running SCPM spectrum to illustrate the similarity between the two. The optical spectrum of the injection signal is also plotted.

As the current is increased to 213 mA, the optical spectrum has shifted and exhibits significant higher wavelength components. This corresponds to the point of strongest power reduction, and is shown in Figure 5.12. It is labeled point B in Figure 5.10. The laser spectrum contains a strong peak which resembles the narrow injected spectrum, as well as significant higher-wavelength components. The higher-wavelength portion peaks at about 1566 nm.

At a current of 214 mA, the optical spectrum exhibits unstable behavior with a noticeable substructure. This is shown in Figure 5.13. This corresponds to a point of moderate power reduction, and is labeled point C in Figure 5.10.

At a current of 215 mA, optical spectrum shifts instead to lower wavelengths. This is shown in Figure 5.14, and corresponds to a point of minimal power reduction. It is labeled point D in Figure 5.10. Here, the laser spectrum consists of a strong peak at about 1562 nm. Therefore, a change of about 4 nm has occurred as the cavity tuning is varied across the coherent injection locking range.

As the current is further increased, the optical spectrum returns to that of the free-running SCPM laser. This is also labeled point A in Figure 5.10, and corresponds to a current of about 217 mA. A separate figure is not given because this spectrum is nearly identical to that of 211 mA.

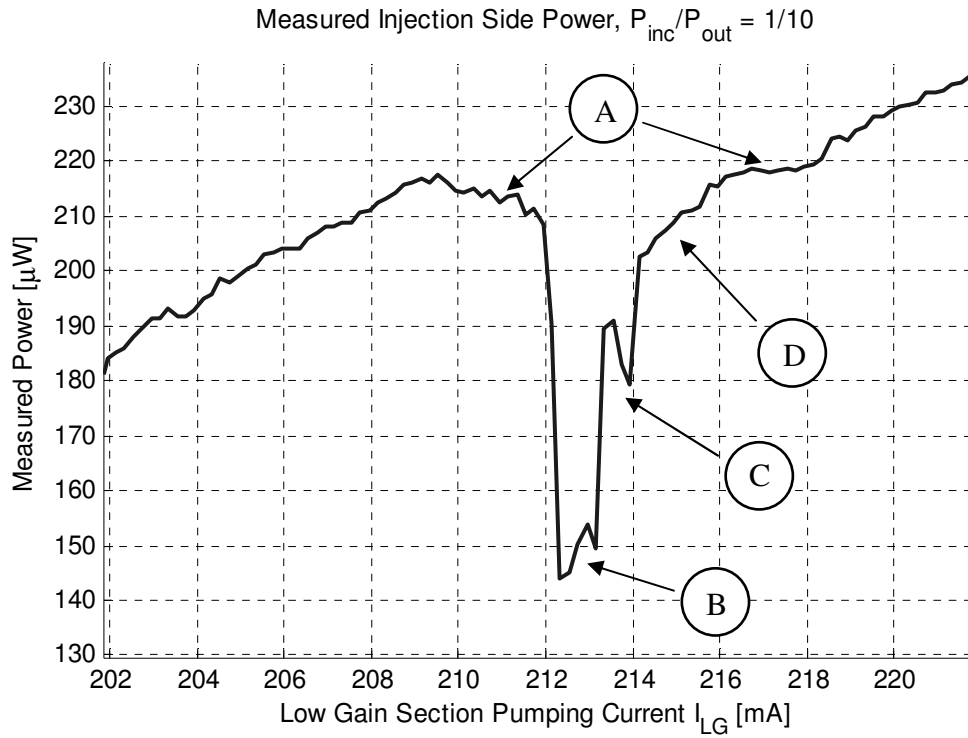


Figure 5.10: Reflected power curve for a power ratio of 1/10. Labels A, B, C, and D correspond to the selected spectra at 204 mA, 213 mA, 214 mA, and 215 mA.

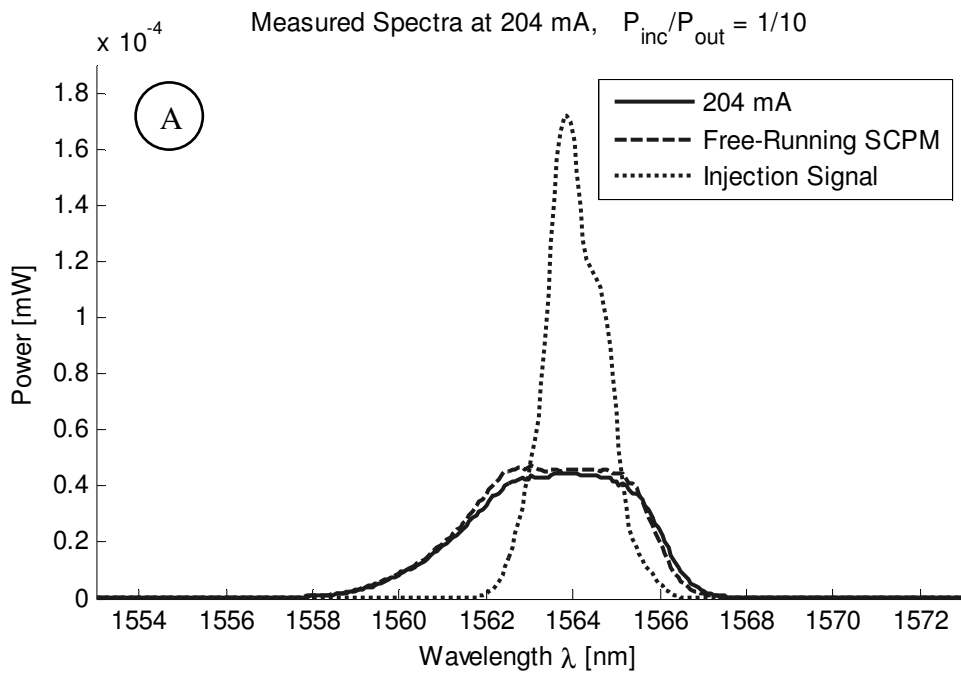


Figure 5.11: Measured output spectra of laser at 211 mA. Representative of the spectra outside the locking range. Spectra essentially same as free-running case.

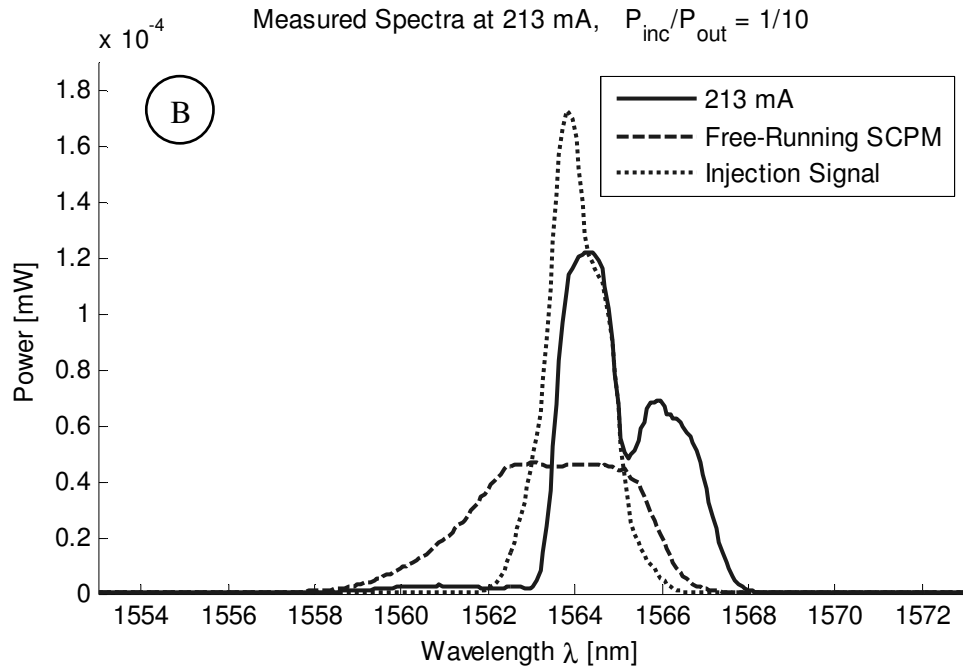


Figure 5.12: Measured output spectra of laser at 213 mA. Representative of the spectra at the point of maximum power reduction. Shift to higher wavelengths.

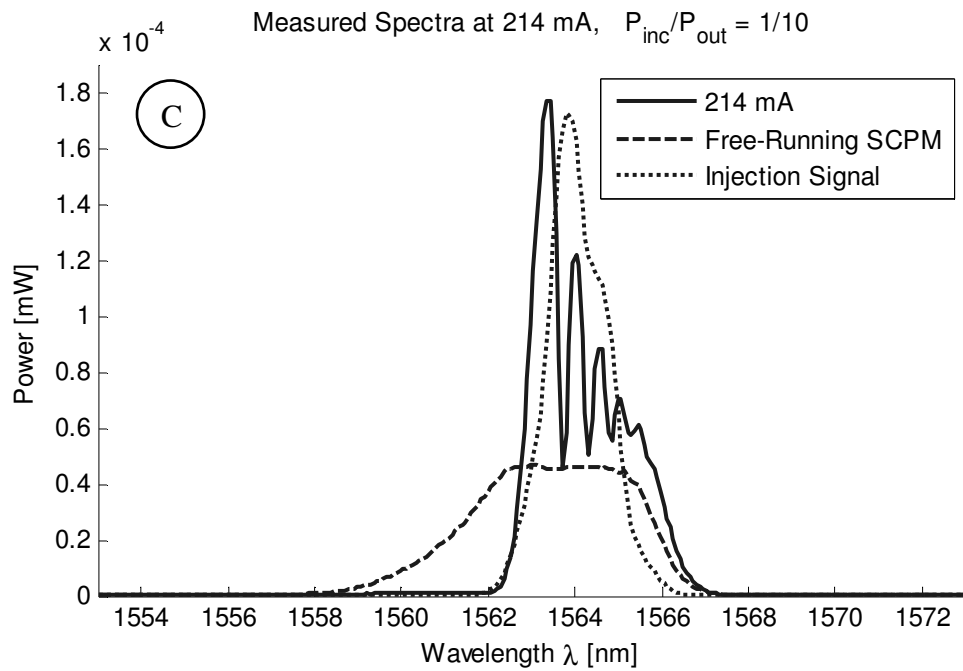


Figure 5.13: Measured output spectra of laser at 214 mA. Representative of unstable condition at a point of moderate power reduction.

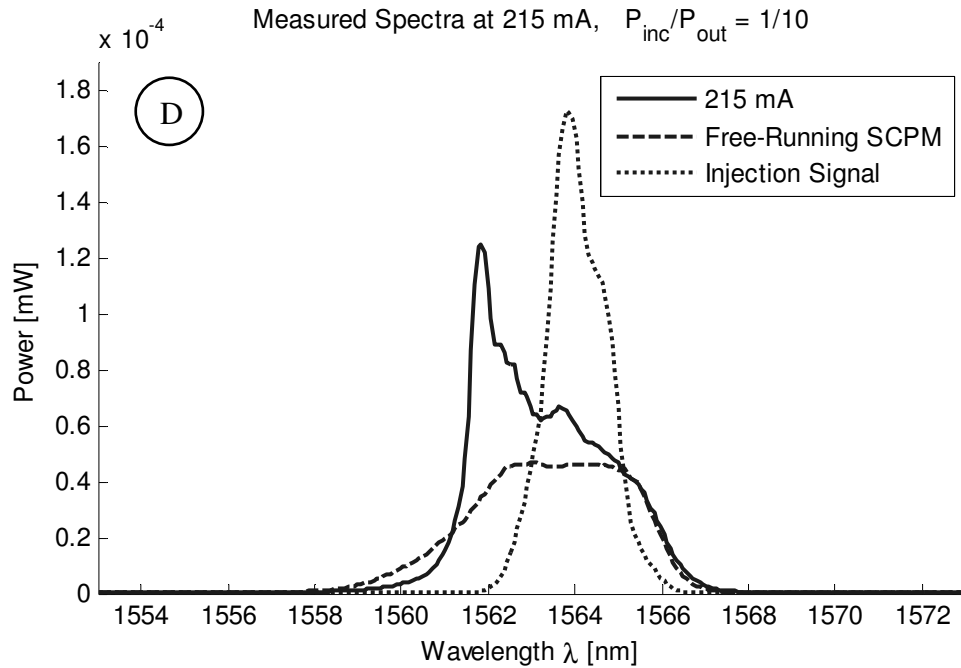


Figure 5.14: Measured output spectra of laser at 215 mA. Representative of spectra at a point of minimal power reduction. Shift to lower wavelengths.

Now that the behavior of the optical spectrum has been examined, it makes sense to observe the corresponding pulse shapes in time. The principle of cross-correlation was explained in Chapter 2. Here, as illustrated in Figure 5.3, the reference signal is the same signal that is used as the injection source. The cross-correlator (CORR) functions by sweeping the path delay of one signal through a window of about 100 ps, while keeping the path of the other signal constant. The correlation signal is averaged over many of these 100 ps sweeps. Due to this mechanism, the CORR will only yield a measurable correlation trace if the two signals being correlated have components at the same RF repetition frequency. If the two signals have different repetition frequencies, the pulses will meet and correlate at a different position in the 100 ps window on each sweep. In that case, the measured trace will quickly average out to a baseline pedestal. Since the injection source itself

is used as the reference for the CORR, the cross-correlation trace will not yield a measured signal unless the SCPM laser is RF locked to the injection signal.

Therefore, the cross-correlation traces also function as a check on the RF locking status of the laser.

The cross-correlation traces for the case of high power injection are now presented. The measurements reveal that the laser pulse shape changes dramatically as pumping current is varied through the range of the power reduction dip. Measured cross-correlation traces are taken at the same currents at which the selected optical spectra were taken.

The cross-correlation trace corresponding to points A in Figure 5.10 is shown in Figure 5.15. Recall that these points, at 211 mA and 217 mA, correspond to cases for which the laser is not coherently injection locked. However, since the correlation trace clearly shows a measured pulse, the laser is RF locked. This agrees with the results of the RF spectra measurements, which are depicted in Figure 5.6. There, it is confirmed that the RF locking range encompasses the points labeled A in Figure 5.10. The correlation traces for 211 mA and 217 mA are essentially the same. The pulse has a sharp leading edge, or foot, and a gradually tapering trailing edge, or tail. The FWHM of the pulse is about 23 ps.

The second point examined corresponds to maximum power reduction. Again, it is taken at a pumping current of 213 mA, and is labeled point B in Figure 5.10. The pulse here is narrow with slightly tapering foot and a very sharply falling tail, and is shown in Figure 5.16. The FWHM of the pulse is about 10 ps.

The third trace is taken at the point of moderate power reduction, labeled point C in Figure 5.10. This trace consists of a significant and broad foot structure, followed by the narrower pulse with a very sharply falling tail. It is taken at 214 mA, and is shown in Figure 5.17. The FWHM of the signal at this point is not a useful measure because the signal consists of two pulse-like structures.

The last trace is taken at a point of minimal power reduction, labeled point D in Figure 5.10. Here, the foot structure has become the dominant pulse, with the narrower pulse diminished in amplitude. It is taken at 215 mA, and is shown in Figure 5.18. Again, the FWHM is not a useful measure for this trace. At this point, the foot of the pulse has advanced by about 23 ps compared to the non-injection-locked case at 211 mA. Compared to the case at 213 mA, the foot of the pulse has advanced by about 15 ps.

In summary, the pulsed coherent injection locking behavior, for the case of high power injection, exhibits clear trends in both optical spectrum and pulse shape. The characteristics are examined as the optical tuning is varied in the direction of increasing pump current. The peak of the optical spectrum shifts from higher wavelengths to lower wavelengths. There is an overall 4 nm shift from the significant shifted component at the point of maximum power reduction to the point of minimal power reduction. At the same time, the pulse shape changes dramatically. It starts from a relatively narrow pulse. As the optical tuning is varied, a broader pulse develops out of the foot of the narrow pulse and advances forward in the time window. Within the coherent injection locking range, the pulse advances forward by about 15 ps.

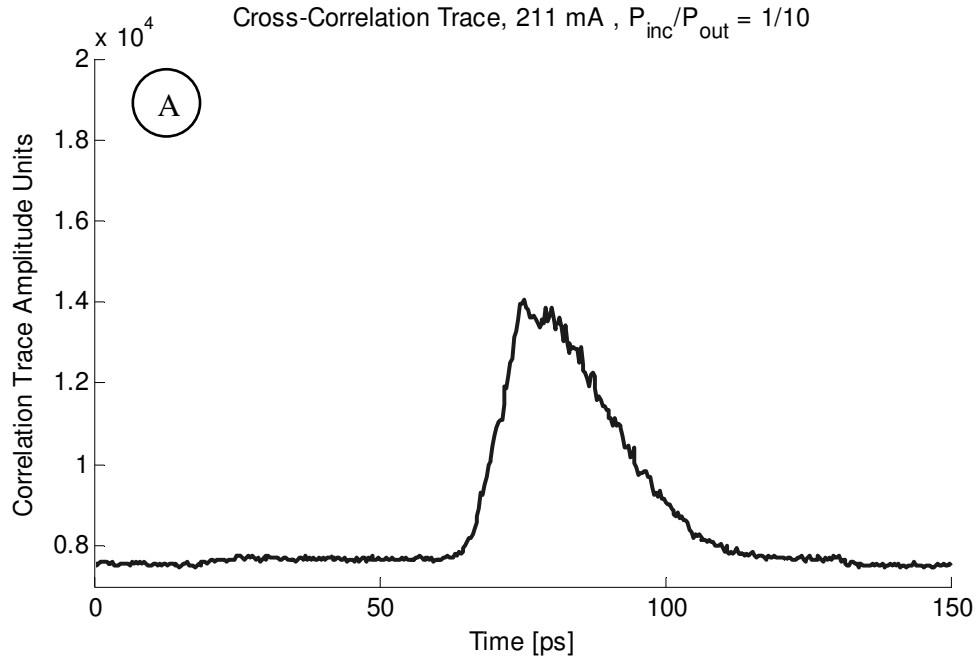


Figure 5.15: Cross-correlation trace at pumping current of 211 mA, corresponding to a point in RF locking range but outside coherent locking range.

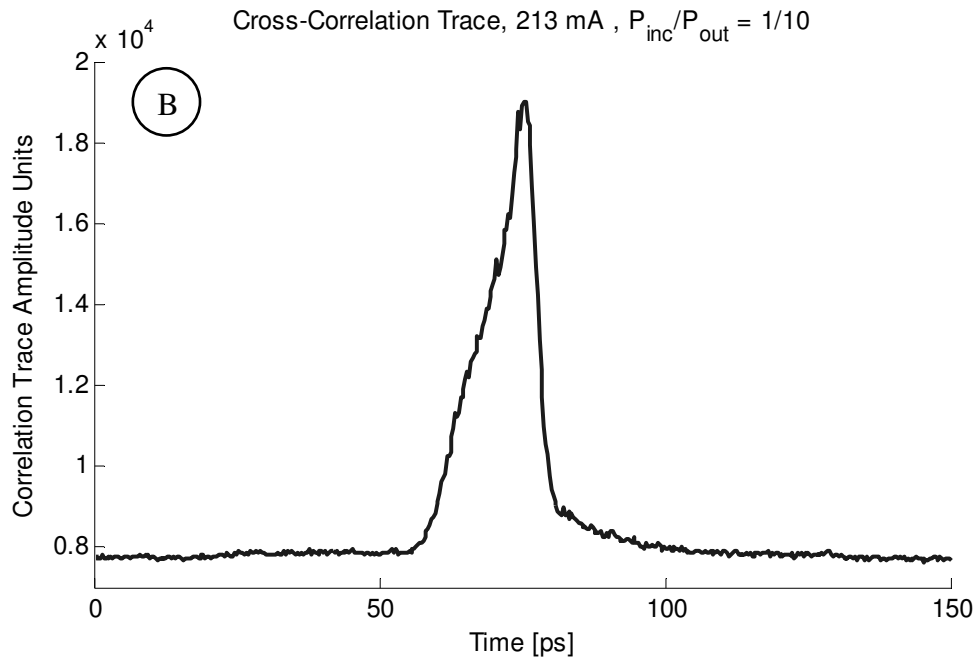


Figure 5.16: Cross-correlation trace at pumping current of 213 mA, corresponding to the point of maximum power reduction.

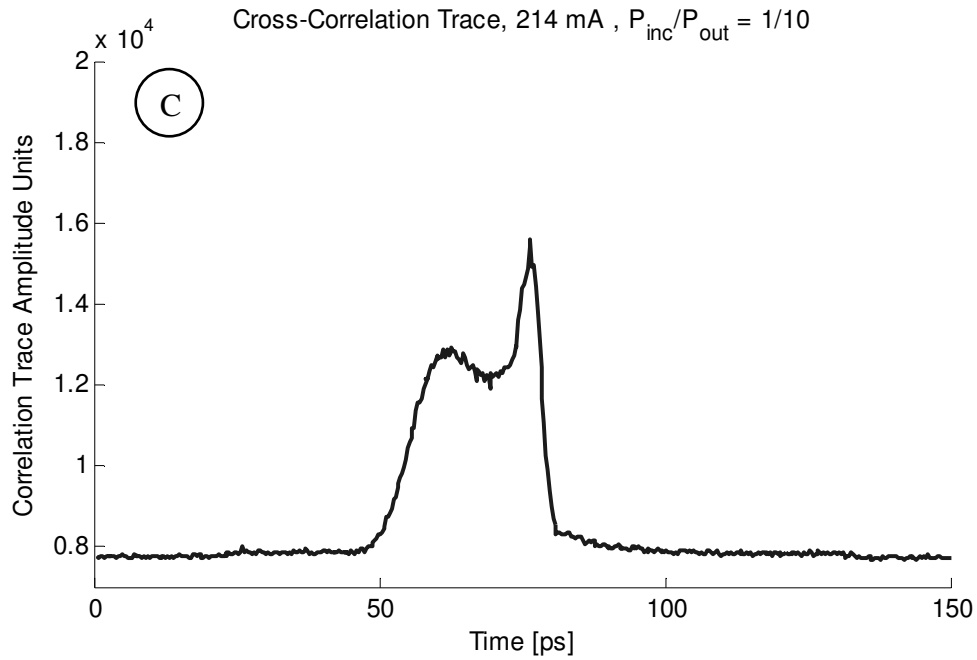


Figure 5.17: Cross-correlation trace at pumping current of 214 mA, corresponding to a point of moderate power reduction.

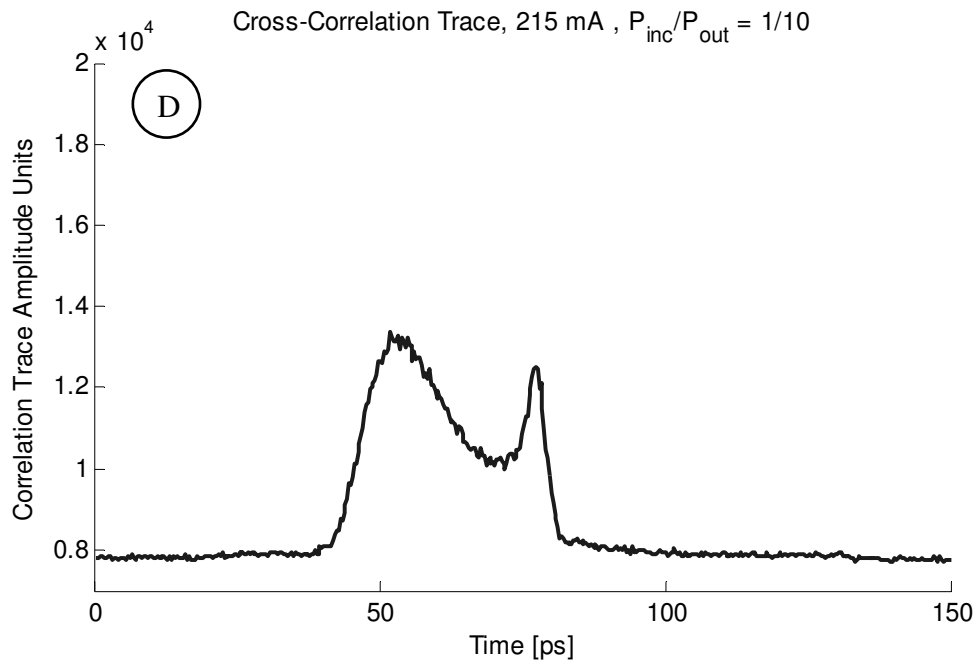


Figure 5.18: Cross-correlation trace at pumping current of 215 mA, corresponding to a point of minimal power reduction.

The behavior of the spectra for the low power injection case, with a power ratio of 1/100, is examined. The behavior is similar to the high power case, except the shift to the higher wavelengths is much less pronounced. However, the point of unstable spectra and the point of shifting to lower wavelengths are both present. The reflected power curve is replotted in Figure 5.19 with labels corresponding to the selected spectra.

At a pumping current of 208 mA, the spectra is the essentially that of the free-running SCPM laser. This is as shown in Figure 5.20, and is labeled point A in Figure 5.19. As with the case of high power injection, this is a point at which the laser is RF locked but not coherently injection locked.

At 211 mA, the spectrum shows a weak shift to higher wavelengths. This is shown in Figure 5.21, and is labeled point B in Figure 5.19. Unlike the high power injection case, the spectra here does not seem to consist of the injected signal spectrum with a significant higher wavelength component. Instead, it merely shows a weak preference for higher wavelengths, while conforming primarily to the free-running spectrum. The spectral peak is at about 1564.5 nm. This indicates that at a power ratio of 1/100, it is difficult to achieve coherent injection locking.

At 212 mA, the spectrum is unstable and exhibits complicated substructure. This is shown in Figure 5.22, and is labeled point C in Figure 5.19. This is quite similar to the high power injection case, which indicates that the unstable point is easily reached even for low power injection.

Finally, at 213 mA, the spectrum exhibits a shift to lower wavelengths. This is shown in Figure 5.23, and is labeled point D in Figure 5.19. Here, the shift to

lower wavelengths is once again not as strong as for high power injection. Still, a preference for lower wavelengths is clear. The spectral peak lies at about 1562 nm. Therefore, the spectral peak shifts by about 3 nm as the cavity is tuned across the coherent injection locking range.

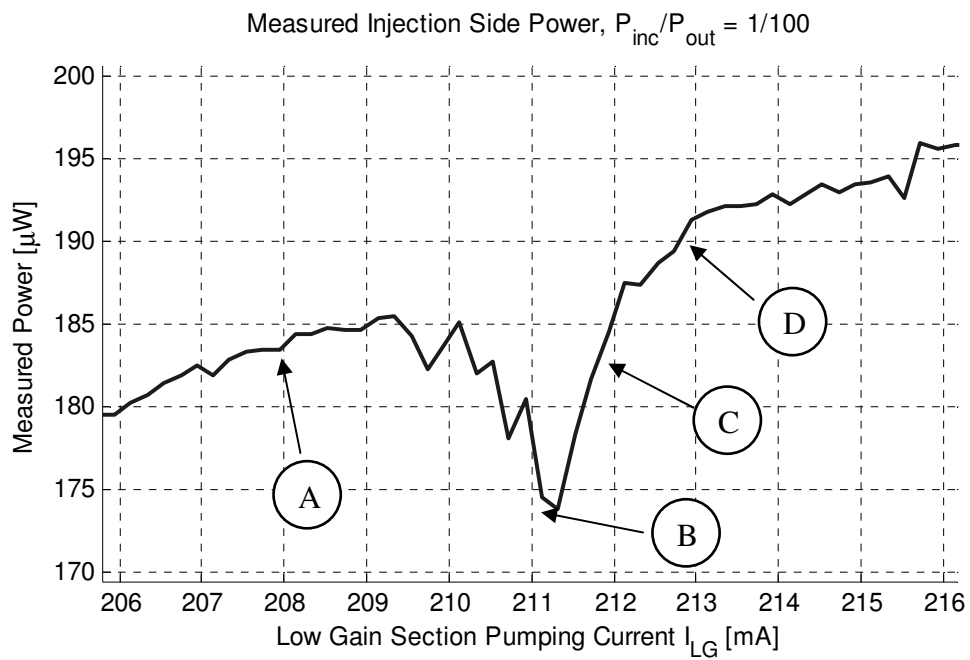


Figure 5.19: Reflected power curve for a power ratio of 1/100. Labels A, B, C, and D correspond to the selected spectra at 208 mA, 211 mA, 212 mA, and 213 mA.

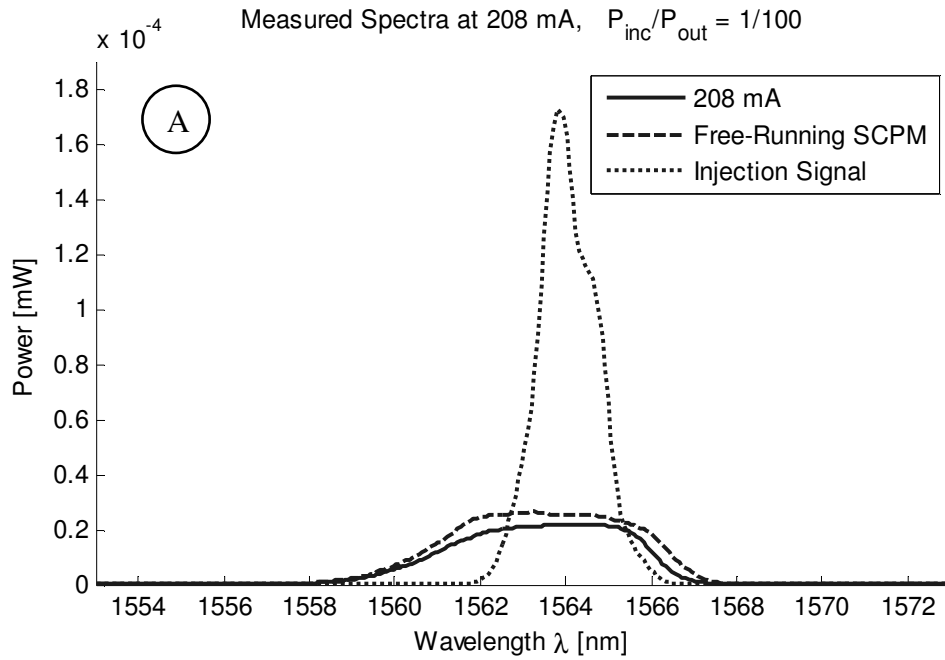


Figure 5.20: Measured output spectra of laser at 208 mA. Representative of spectra outside the locking range. Spectra essentially same as free-running case.

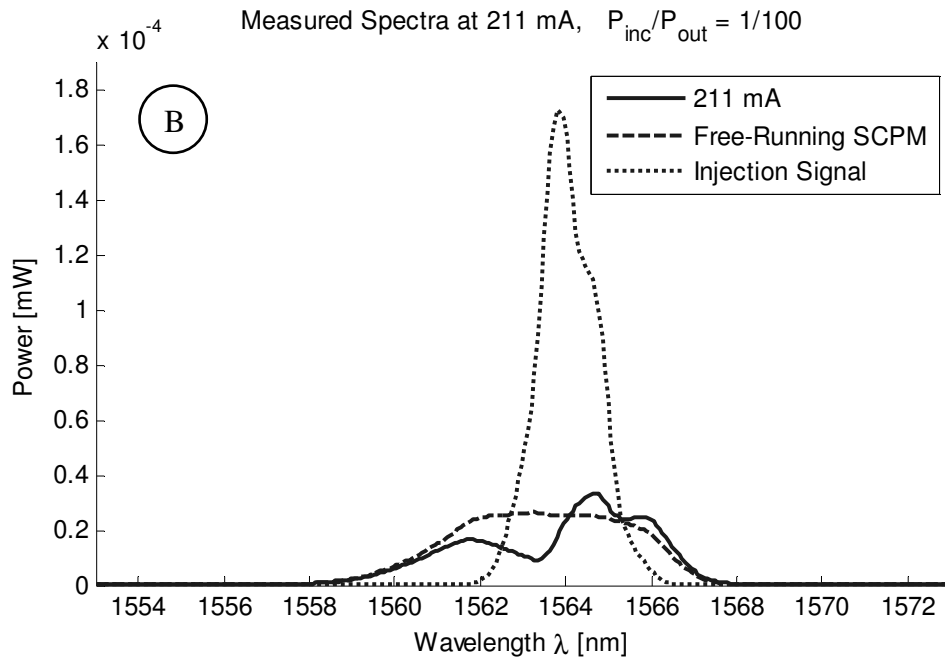


Figure 5.21: Measured output spectra of laser at 211 mA. Representative of spectra at the point of maximum power reduction. Weak shift to higher wavelengths.

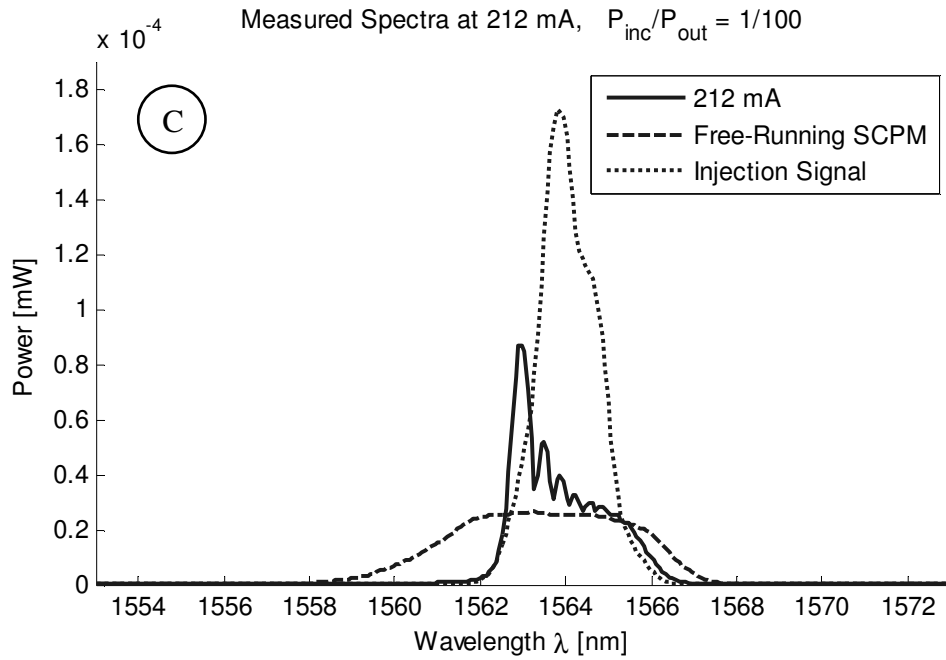


Figure 5.22: Measured output spectra of laser at 212 mA. Representative of unstable condition at a point of moderate power reduction.

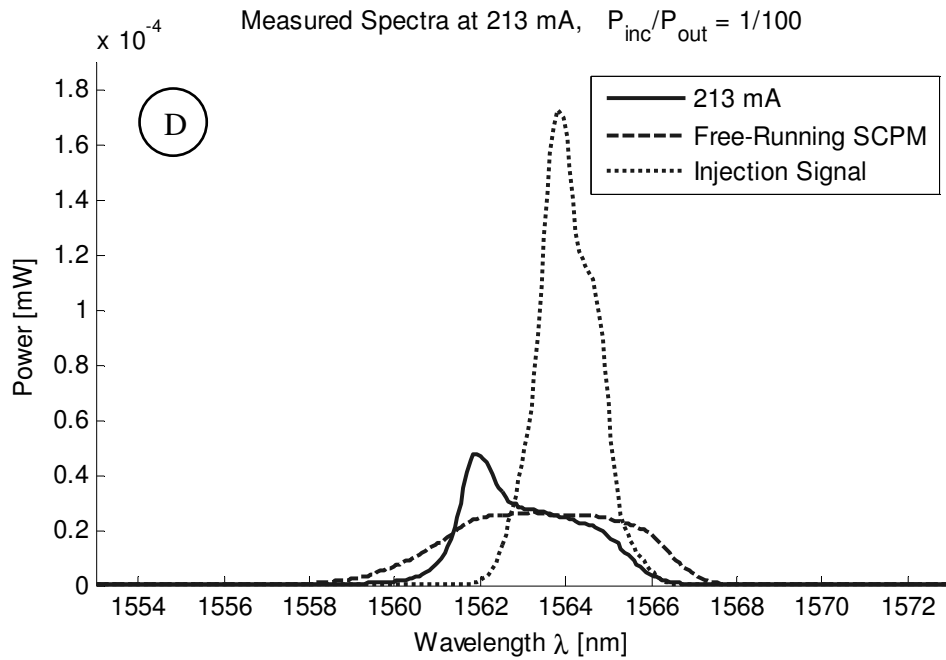


Figure 5.23: Measured output spectra of laser at 213 mA. Representative of spectra at a point of minimal power reduction. Shift to lower wavelengths.

The measured cross-correlation traces for low power injection are similar to the high power results, except the narrow pulse feature is absent. The broad pulse is still present, however, and it experiences the same advancing in time as the pumping current is increased. Another key difference in the low power case is that the pulse is not observed to revert to its original position in time as the current is increased.

The first correlation trace corresponds to a point inside the RF locking range but not in the coherent locking range, and is shown in Figure 5.24. It is taken at a current of 209 mA, and is labeled point A in Figure 5.19. The pulse is broad and has a FWHM of about 25 ps, which is very close to the corresponding high-power case. This indicates that the RF locking mechanism is not as strongly dependent on injection power as the coherent injection locking mechanism.

The next correlation trace corresponds to the point of maximum power reduction, and is shown in Figure 5.25. It is taken at a current of 211 mA, and is labeled point B in Figure 5.19. The signal shape is not a smooth pulse, but it is advanced significantly in time compared to the pulse at 209 mA. It has a long and gradual tail, with the hint of a central smaller pulse like in the high power injection case. At this point, the foot of the pulse has advanced in time by about 23 ps.

The third correlation trace corresponds to a point of moderate power reduction, and is shown in Figure 5.26. It is taken at a current of 212 mA, and is labeled point C in Figure 5.19. It is similar to the pulse at 211 mA, but advanced further forward in time by about 14 ps, which places it about 37 ps ahead of the non-coherent injection locked pulse.

The last correlation trace corresponds to a point of minimal power reduction, and is shown in Figure 5.27. It is taken at a current of 213 mA, and is labeled point D in Figure 5.19. It is similar to the pulse at 212 mA, but advanced even further in time. At this point, the leading edge of the pulse is advanced by about 22 ps ahead of the pulse at the point of maximum power reduction. This places it about 45 ps ahead of the non-coherent injection locked pulse.

The behavior of this last correlation trace does not match the corresponding trace of the high power case. With high power injection, the last correlation trace reverted back to the position of the other non-injection-locked case. It may be that at 213 mA, the laser was still operating in the coherent injection locked regime. Although the pumping current was increased slowly and the CORR output monitored carefully, the transition point from the coherent injection locked regime to the RF locking regime was not found. When the pumping current was increased to 215.5 mA, the correlation signal ceased to produce a pulse shape, and instead yielded the background pedestal. This indicated that the laser had left the RF locking regime as well as the coherent injection locked regime.

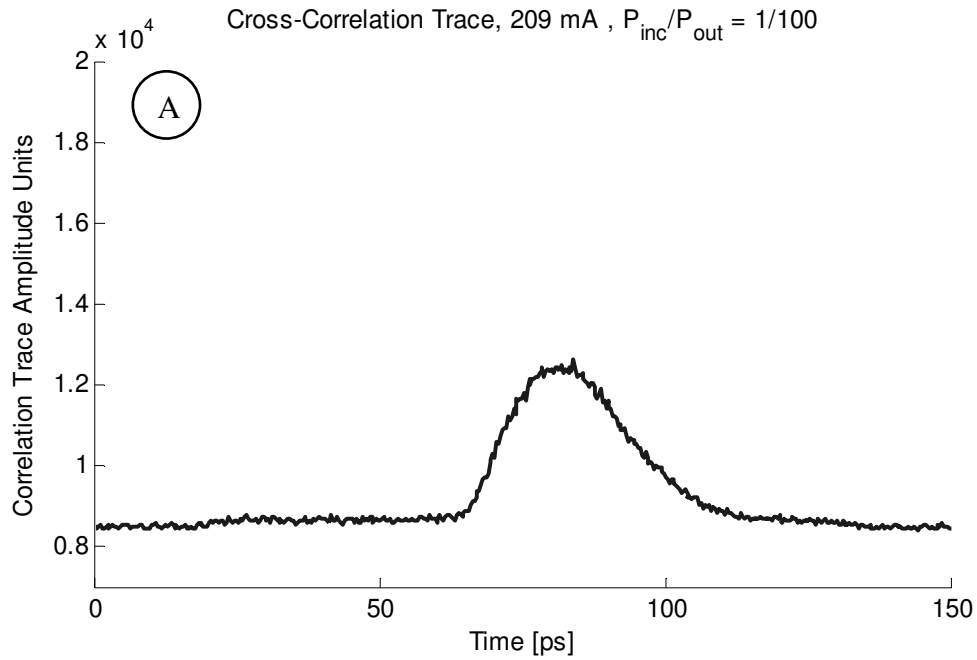


Figure 5.24: Cross-correlation trace at pumping current of 209 mA, corresponding to a point in RF locking range but outside coherent locking range.

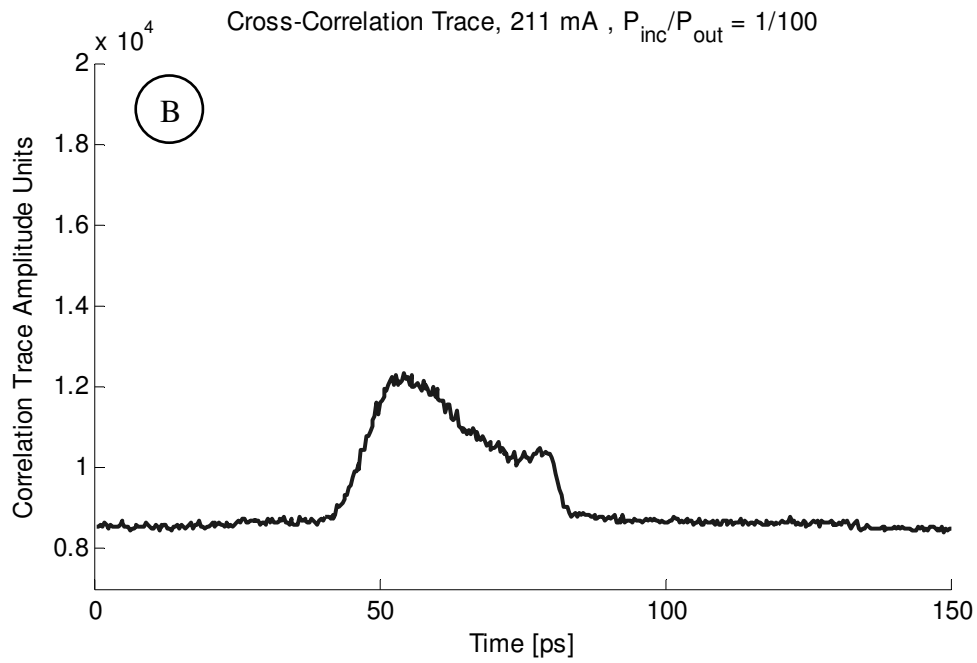


Figure 5.25: Cross-correlation trace at pumping current of 211 mA, corresponding to the point of maximum power reduction.

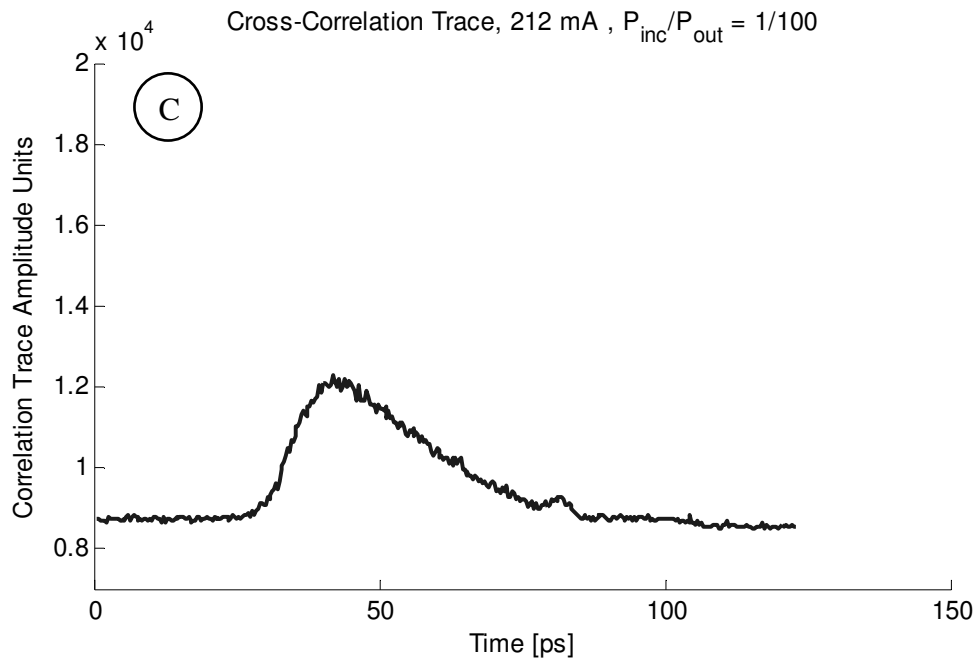


Figure 5.26: Cross-correlation trace at pumping current of 212 mA, corresponding to a point of moderate power reduction.

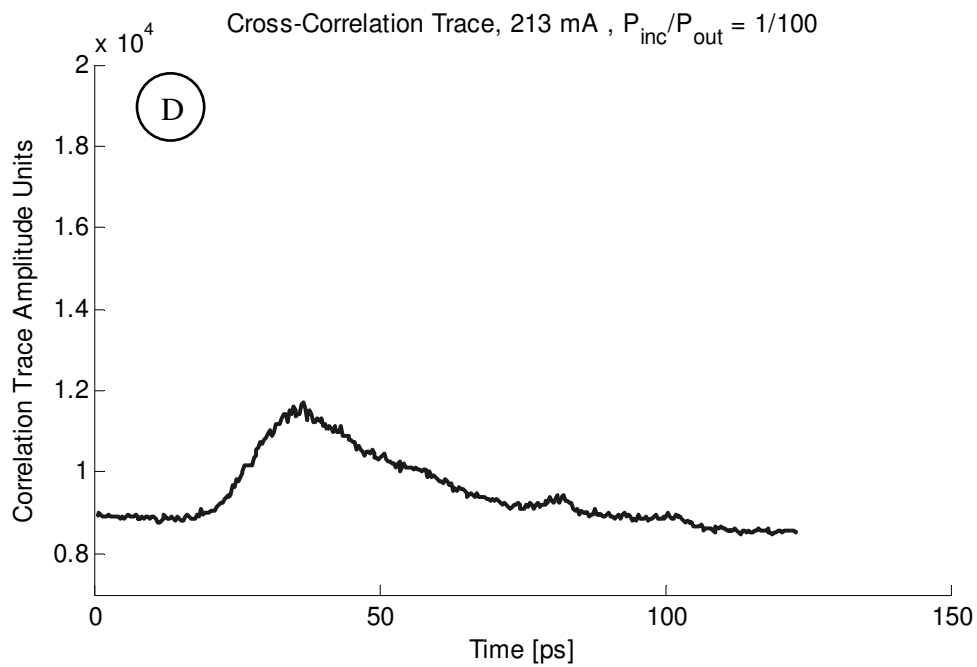


Figure 5.27: Cross-correlation trace at pumping current of 213 mA, corresponding to a point of minimal power reduction.

A technical issue in the experiment is worth mentioning here. The particular points of interest, labeled A, B, C, and D in the various reflected power plots, corresponded to very specific pumping currents. For example, point B in Figure 5.19 corresponded to an optical spectrum and a cross-correlation trace taken at a pumping current of 211 mA. However, the exact values of the pumping currents which yield the selected spectra and correlation traces are observed to shift over time. For example, the same spectrum and correlation trace corresponding to point B in Figure 5.19 may require a current of 213 mA if the measurement was repeated on a different occasion. In other words, the pumping current ranges over which the reflected power dip occurs changes over time. This indicates that the measurement setup is subject to drift in one or more of its critical parameters. One possible cause is temperature drift in either the commercial injected laser or the SCPM laser. It is also possible that the modes of the commercial injected laser may drift over time. Finally, the alignment of the optical fibers may also slightly drift over time.

In summary, the method of coherent pulsed injection locking of a mode-locked laser is characterized by examining RF spectra, optical spectra, and cross-correlation traces. Both high power (1/10) and low power (1/100) injection cases are investigated. The results are clearer for high power injection, which indicates that this method requires a significant injection power. As the optical cavity tuning is varied across the coherent injection locking range, the optical spectrum of the laser signal is observed to shift by about 3 nm to 4 nm from higher to lower wavelengths. The pulse shape is observed to advance forward in time by 15 ps to 22 ps as the cavity is tuned across the coherent injection locking range.

Chapter 6: Theoretical Model

A simple numerical model was developed in an attempt to explain the experimental results of the pulsed injection locking method. The model treats the SCPM laser as the combination of a saturable gain section, a saturable absorber section, an unsaturable absorption factor, and a bandwidth limiting element. It includes the key effect of tuning of the SCPM laser cavity. In addition, it takes into account the fact that the true repetition rate of the laser output does not correspond to the physical length of the laser cavity. A schematic of the model is shown in Figure 6.1. The model is exceedingly rudimentary, and requires much more development. However, it is capable of qualitatively confirming two of the measured experimental effects. First, the reflected power diagnostic introduced in Section 4.3 is generated by the model. Second, the shifting behavior of the output optical spectrum is also exhibited in the numerical results.

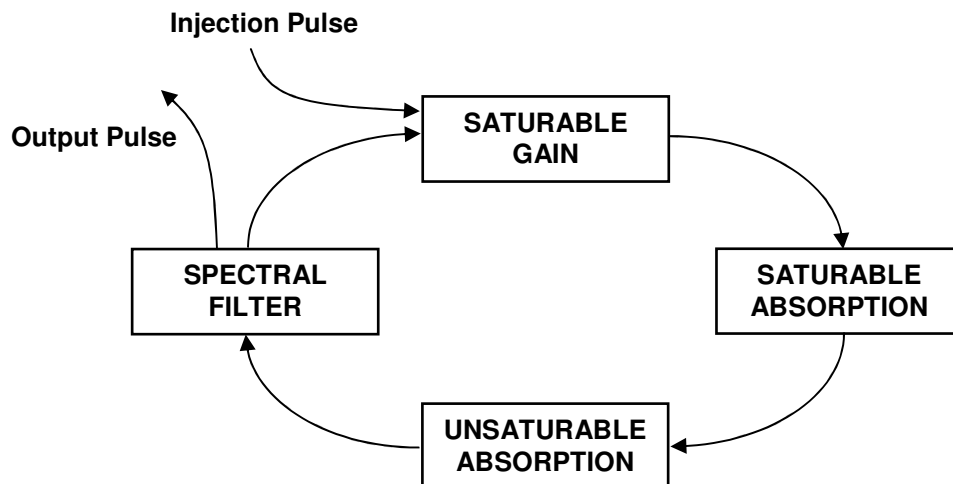


Figure 6.1: Schematic of numerical model for pulsed injection locking of a mode-locked laser.

The structure of the model follows a loop which is repeated until the calculated laser signal reaches a steady state. On each round trip, the model starts with an electric field phasor $E_1[t]$ which is defined over a time array t . The time array spans a period of 100 ps, which corresponds to a cavity round trip time of 10 GHz. This is a nominal period chosen to represent the actual round trip time of about 10.8 GHz in the experiment. The time step dt of the time array is 0.1 ps. The Frantz-Nodvik equation is used to calculate the time-varying gain that the saturable gain element applies to $E_1[t]$. The equation is given by Eq. (2.48) from Section 2.3,

$$G[t] = \frac{G_0}{G_0 - (G_0 - 1)e^{-U_1[t]/E_{sat,G}}} \quad (5.1)$$

where $E_{sat,G}$ is the saturation energy of the saturable gain element, and G_0 is the unsaturated value of the gain. By using the same constant value for the unsaturated gain on every round trip, the model assumes that the gain recovers fully after each round trip. Here, $U_1[t]$ is the integrated cumulative energy in $E_1[t]$, and is given by Eq. (2.46) from Section 2.3 to be

$$U_1[t] = \frac{1}{2} \left\{ I_1[1] + I_1[t] + 2 \times \sum_{m=2}^{t-1} I_1[m] \right\} \times dt \quad (5.2)$$

Here, $I_1[t] = |E_1[t]|^2$ is the intensity associated with $E_1[t]$. The integration of the intensity in Eq. (5.2) is numerically calculated using the trapezoid rule. Once the integrated energy and gain are calculated, the gain is applied to $E_1[t]$, and the result is named $E_2[t]$. The resulting field is calculated by using Eqs. (2.39) and (2.41), and is given by

$$E_2[t] = e^{g/2} \times^{-j\alpha_G g/2} \times E_1[t] \quad (5.3)$$

Here, $g = \ln(G)$ is the exponential gain coefficient and α_G is the linewidth enhancement factor of the saturable gain section.

Next, the effect of the saturable absorber is calculated in the same way as that of the saturable gain. The saturable absorption is simply

$$A[t] = \frac{A_0}{A_0 - (A_0 - 1)e^{-U_2[t]/E_{sat,A}}} \quad (5.4)$$

where $E_{sat,A}$ is the saturation energy of the saturable absorber, and A_0 is the unsaturated value of the absorption. As with the saturable gain, the model assumes that the saturable absorber recovers fully after each round trip. The cumulative energy $U_2[t]$ is calculated in the same way as for $U_1[t]$ in Eq. (5.2). The resulting field $E_3[t]$ after the saturable absorber is given by

$$E_3[t] = e^{a/2} \times^{-j\alpha_A a/2} \times E_2[t] \quad (5.5)$$

The unsaturable absorption is simply modeled by a constant power loss coefficient K . It takes into consideration the cavity losses due to the portions of the circulating laser energy which transmit out of the cavity on each round trip, as well as any intrinsic losses inside the cavity. The field after the unsaturable absorption is

$$E_4[t] = \sqrt{K} \times E_3[t] \quad (5.6)$$

where the square root is due to the fact that K represents the power loss.

Next, a bandwidth limiting element is included to account for the fact that the actual laser gain has a finite spectral width. Indeed, this spectral filter component is critical for the model to function properly. Without the spectral filter, the saturable

gain and absorption dynamics work to narrow the circulating laser pulse on each round trip. The finite bandwidth of the laser limits the ultimate pulse narrowing that can be achieved. The effect of the spectral filter is calculated by first taking the Fourier transform of the field $E_4[t]$, which is denoted $\tilde{E}_4[f]$, and then applying a Gaussian filter in the frequency domain, given by

$$\tilde{E}_5[f] = \tilde{E}_4[f] \times e^{-4\ln(2)(f/w)^2} \quad (5.7)$$

where w is the FWHM of the spectral filter in Hz. The inverse Fourier transform of the resulting spectrum $\tilde{E}_5[f]$ is then taken to yield the circulating signal $E_5[t]$.

Then, the effect of the cavity tuning is calculated. When the laser cavity is tuned by adjusting the pumping current, the axial modes ω_q are shifted by a small amount. This is equivalent to applying a small, constant phase change θ to the circulating laser signal. If the axial modes are shifted by an amount equal to the axial mode spacing $\Delta\omega_{ax}$, which results in the shift of any given mode ω_q to its adjacent neighbor ω_{q+1} , the associated constant phase change experiences a variation from 0 to 2π . Therefore, the effect of cavity tuning is calculated by

$$E_6[t] = E_5[t] \times e^{j\theta} \quad (5.8)$$

The value of θ is varied from 0 to 2π to simulate change in cavity tuning that results in a spectral shift of $\Delta\omega_{ax}$.

On each round trip, the circulating signal is also assumed to shift in time by a constant δt . This takes into consideration the fact that the true repetition rate of the laser does not depend simply on the cavity length and background refractive index. As mentioned in Section 5.1, the nonlinearities of the laser cause the true repetition

rate to settle to a value different from that of the ideal cold cavity. If the time shift δt is not included, the pulse becomes shifted within the time window by a small amount from each round trip to the next. By incorporating the time shift, we are slightly shifting the time window on each round trip. As a result, the repetition rate of the injection signal is different from the cold cavity round trip. This time shift correction is calculated by employing the Fourier transform duality rule which states that a shift in time domain is equivalent to a linearly varying phase in frequency domain. The field $E_6[t]$ is transformed to Fourier domain, then multiplied by a linearly varying phase in frequency, and the resulting field $\tilde{E}_7[f]$ is transformed back to the time domain. The calculation is given by

$$\tilde{E}_7[t] = \tilde{E}_6 \times e^{-j2\pi f \delta t} \quad (5.9)$$

The resulting circulating field $E_7[t]$ is then redefined as $E_1[t]$, and the process is repeated for successive round trips. The inclusion of this time shift factor, combined with the fact that the injected pulse is always placed in the center of the time window, means that the injection signal has an actual repetition rate that is different from the 10 GHz rate that corresponds to the 100 ps time window. Effectively, it is the injection signal that deviates from the 10 GHz rate. Since the inclusion of the time shift factor results in stable solutions for some values of θ , we assume that for these conditions, the injected signal is matched to the natural repetition rate of the free-running laser. This natural repetition rate is difficult to calculate, as it depends in a complicated way on the saturation dynamics of the laser.

On each round trip, the coherent interference effect between the reflected incident signal and the output of the laser from the input facet is calculated. The total interfered signal $E_{reduc}[t]$ is given by

$$E_{reduc}[t] = \tau \times E_1[t] + \rho \times E_{inc}[t] \quad (5.10)$$

where τ is the complex field transmission coefficient of the cavity facet and ρ is the reflection coefficient. The injected signal $E_{inj}[t]$ is simply given by the incident signal $E_{inc}[t]$ multiplied by τ . On each round trip, the new circulating signal $E_1[t]$ is augmented by adding $E_{inj}[t]$. A running average of the total energy of $E_{reduc}[t]$ is calculated on each round trip. For a given value of the cavity tuning θ , this average energy represents the amount of interference on the injection side of the laser. This is the coherent injection diagnostic described in Section 4.3.

The model is run for different values of cavity tuning θ , over a range of 2π radians to represent shifting of the laser axial modes over an amount equal to the axial mode spacing. For each value of θ , the model is run until either the circulating pulse stabilizes to an unchanging shape, or until an arbitrary maximum number of round trips has been reached. In order to keep the runtime of the program manageable, the model is allowed to run up to 50 round trips before the system is deemed unstable for the particular value of θ . Using this criteria, it is found that the system is only stable over a narrow range of cavity detuning θ . We assume that a stable output corresponds to the case of coherent injection locking. In this aspect, the model qualitatively agrees with the experimental results presented in Section 4.3.

It is assumed that the model is only valid for values of cavity tuning within the injection locking range, which occurs in the region of reduced power. Outside this range, we expect from the measured experimental results that the laser will not be injection locked. Indeed, the model only yields stable solutions for values of θ between $-0.44 \times 2\pi$ and $-0.29 \times 2\pi$. This is due to the fact that outside the injection locking range, the laser essentially operates in its free-running SCPM regime or in the active mode-locked regime. Unfortunately, the model does not incorporate the effects necessary to simulate this regime of operation.

The model uses reasonable values for the various constants in the equations. The cavity facet field reflection and transmission coefficients are set to $\rho = 0.6$ and $\tau = j \times 0.8$. These are chosen based on the typical refractive index difference at an air-to-semiconductor interface. Also, ρ and τ are offset by a constant phase of $\pi/2$, by making ρ purely real and τ purely imaginary, to account for the transmission effect discussed in Section 4.3. The unsaturated gain and absorption values are set to $G_0 = e^3$ and $A_0 = e^{-0.1}$, respectively. The linewidth enhancement factors α_G and α_A for the saturable gain and absorber sections are both set to 3. The saturation energy of the gain section is $E_{sat,G} = 1$ pJ, while the saturation energy of the absorber section is $E_{sat,A} = 0.2$ pJ. The ratio of the saturation energies, $E_{sat,G}/E_{sat,A} = 5$, is typical for semiconductor mode-locked lasers [19]. The bandwidth of the Gaussian spectral filter is $w = 5 \times 10^{11}$ Hz. The unsaturable loss factor is $K = 0.1$. The incident wave energy is $E_{inc} = 0.5$ pJ. The repetition rate

correction time is $\delta t = 1.5$ ps, which corresponds to a deviation of about 152 MHz from the 10 GHz cavity repetition rate.

The value of the reflected power is calculated as a function of the cavity tuning, expressed in terms of θ , and is shown in Figure 6.2. The calculated curve exhibits the reduced power due to coherent injection. This agrees qualitatively with the measured reduced power curves.

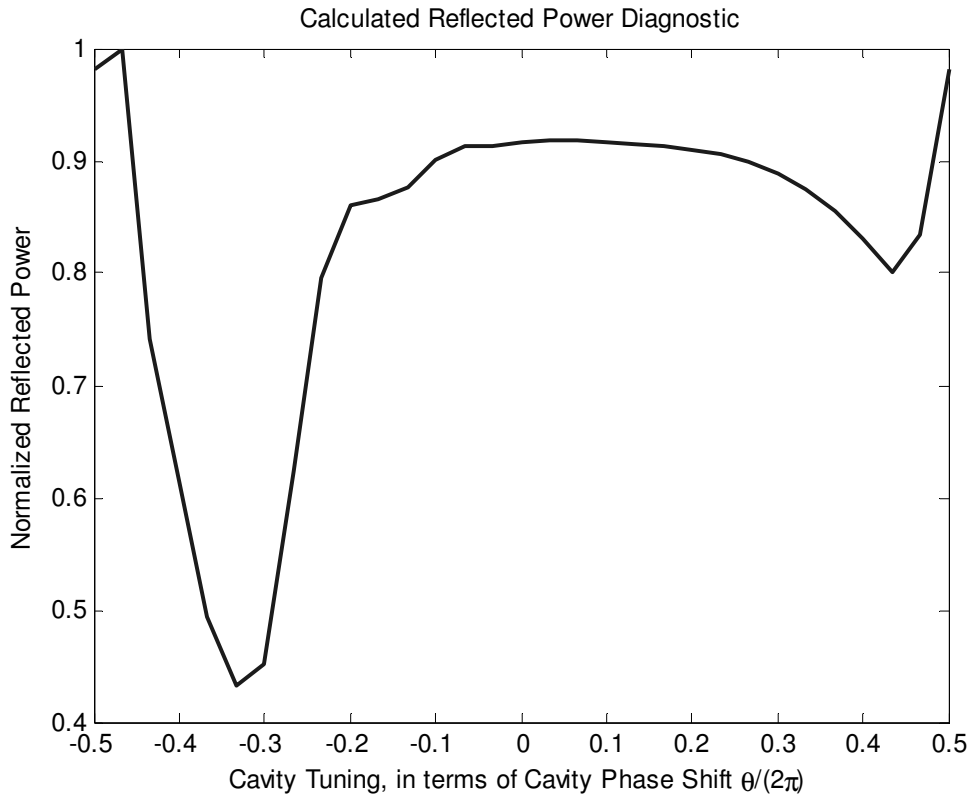


Figure 6.2: Calculated reflected power diagnostic.

This limitation of the model is illustrated in Figure 6.3. The calculated laser output spectra is plotted for various values of the cavity round trip phase detuning θ . According to the model, only the narrow range of values from $-0.44 \times 2\pi$ to

$-0.29 \times 2\pi$ yield stable solutions. These solutions reach a steady state after less than 50 round trips, and are plotted as solid, bold curves. The plotted spectra in the range of unstable solutions continue to fluctuate even as the number of round trips is increased. The unstable spectra are not an accurate depiction of the real laser system outside the locking range. Therefore, they are plotted as dashed, thin curves to represent the fact that significantly more work is needed to accurately model this regime.

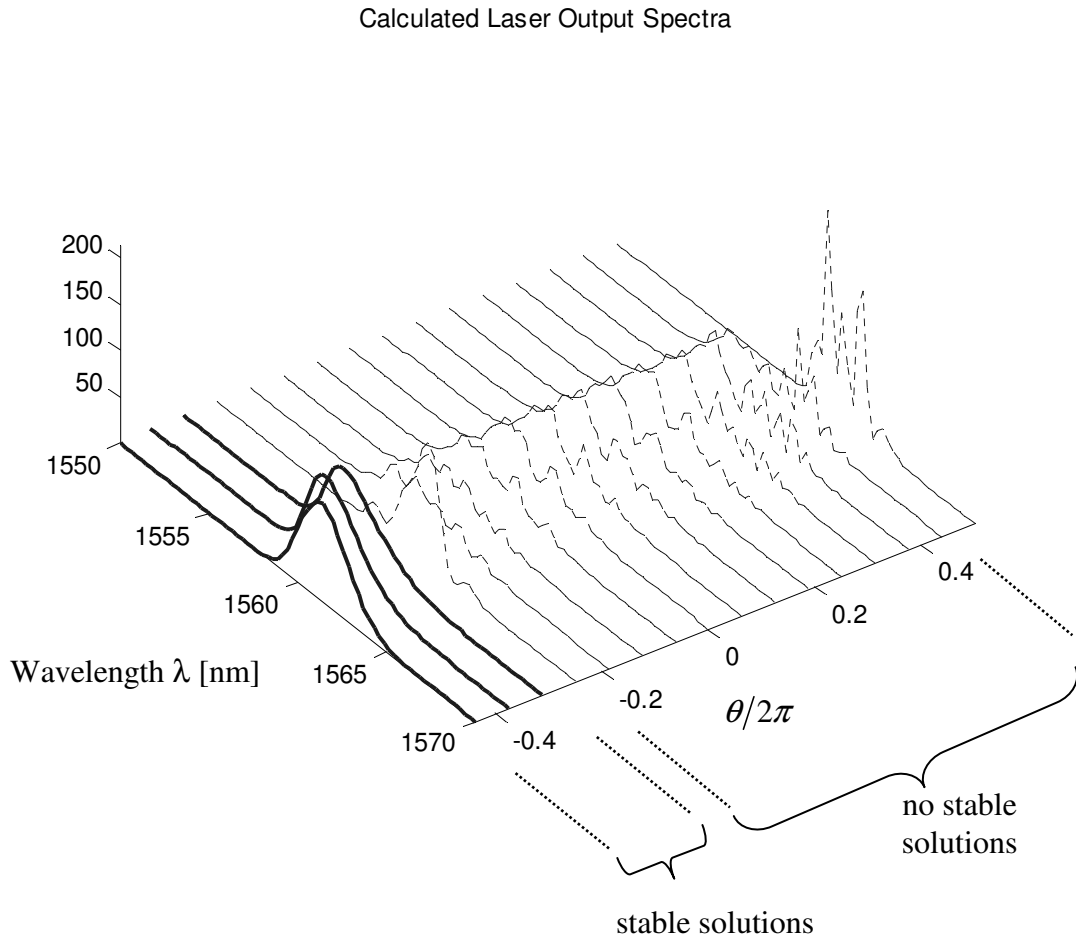


Figure 6.3: Calculated laser spectra for various values of θ .

Several selected laser spectra, for values of θ equal to $-0.44/2\pi$, $-0.36/2\pi$, and $-0.29/2\pi$, are shown in Figure 6.4. As the cavity round trip phase is tuned across the coherent injection locking range, in the direction of increasing pumping current, the peak of the spectrum shifts from higher wavelengths to lower wavelengths. This qualitatively confirms the behavior of the measured spectra, as presented in Section 5.3. In the measured spectra, the spectral peak shifted by about 4 nm in the high power case and by about 3 nm in the lower power case. Here, the calculated spectral peak shifts from 1561.6 nm at $\theta = -0.44/2\pi$ to 1558.6 nm at $\theta = -0.29/2\pi$, which is a 3 nm shift. Therefore, the model confirms the spectral shift behavior of the measured data. The shape of the calculated spectra is quite different from the measured data. This is due to the fact that the model neglects a number of effects which determine the spectrum of the free-running laser, such as amplified spontaneous emission. In the actual laser, the characteristics of the free-running SCPM laser are not completely suppressed, even when RF locking and coherent injection are both achieved. Therefore, the measured spectra will retain features of the free-running spectra regardless of the cavity tuning.

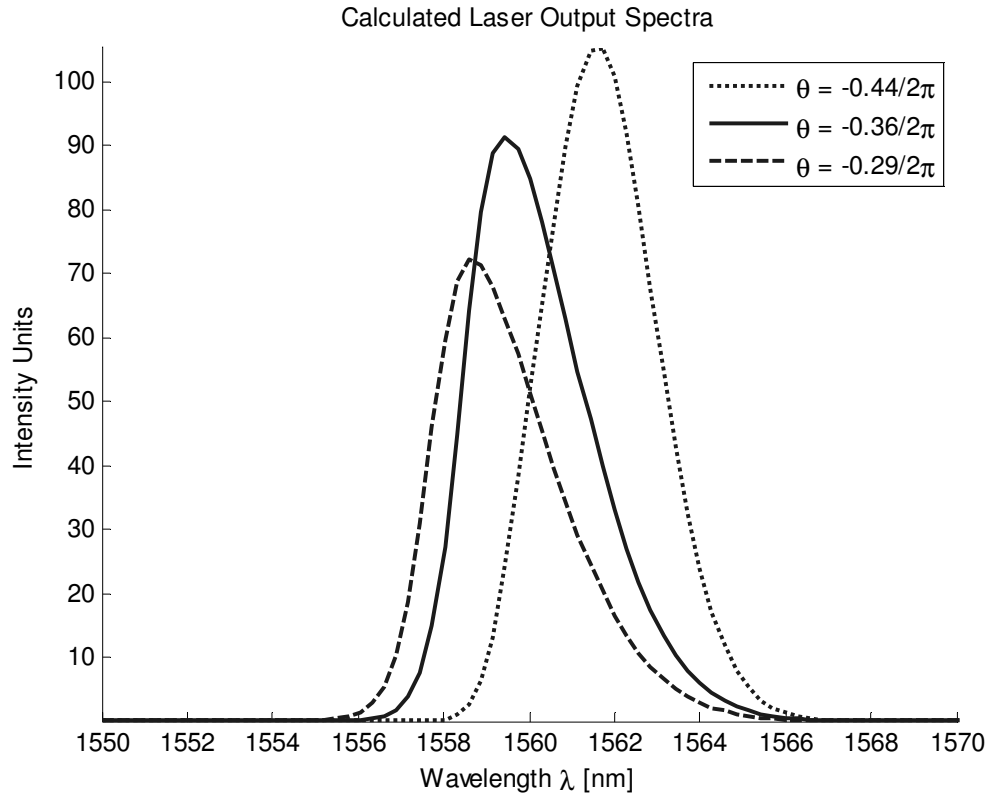


Figure 6.4: Selected calculated laser output spectra, for values of θ within the coherent locking range. A shift in the peak of the spectrum occurs as θ is tuned.

The calculated laser pulses for various values of θ across a full range of 2π are presented in Figure 6.5. In the model, the injected pulse that is added on each round trip is centered around 50 ps. This is the center of the time window used in the model. The few pulses which are shown within the coherent injection locking range are centered near 50 ps, which is expected for coherent locking. The pulse-like solutions which are plotted for θ outside the coherent locking range are unstable solutions. The simulation was arbitrarily run for 50 round trips. If the simulation is continued for more round trips, the pulses in the unstable region will continue to shift in position in the time window, as well as undergo dramatic changes in pulse shape.

However, the pulses in the coherent locking range remain unchanged if the simulation is continued for more round trips.

Several selected laser pulses, for values of θ equal to $-0.44/2\pi$, $-0.36/2\pi$, and $-0.29/2\pi$, are shown in Figure 6.6. Pulse-like solutions are obtained, with FWHM ranging from 8.8 ps at $\theta = -0.44/2\pi$ to 4.6 ps at $\theta = -0.29/2\pi$. The peak of the pulse shifts from about 56.4 ps at $\theta = -0.44/2\pi$ to about 53.1 ps at $\theta = -0.29/2\pi$. Therefore, the pulse seems to advance in time by about 3.3 ps as the cavity round trip phase θ is tuned across the coherent injection locking range, in the direction of increasing pumping current. This is qualitatively similar to the measured results, although the measured data shows a much stronger shift in time.

In summary, the simple model provides qualitative support for the spectral shift that was observed in experiment. However, the model in its current state cannot quantitatively explain the laser system. The pulsed injection locked laser works by the interaction between the free-running laser signal and an injection signal. The model merely attempts to simulate the effects of the laser on a circulating signal. In steady state coherently locked operation, this circulating signal is assumed to primarily depend on the injection signal. The model does not simulate the free-running laser, and therefore the critical interaction is not included.

The simulation is calculated using MATLAB software, and the code is included in Appendix.

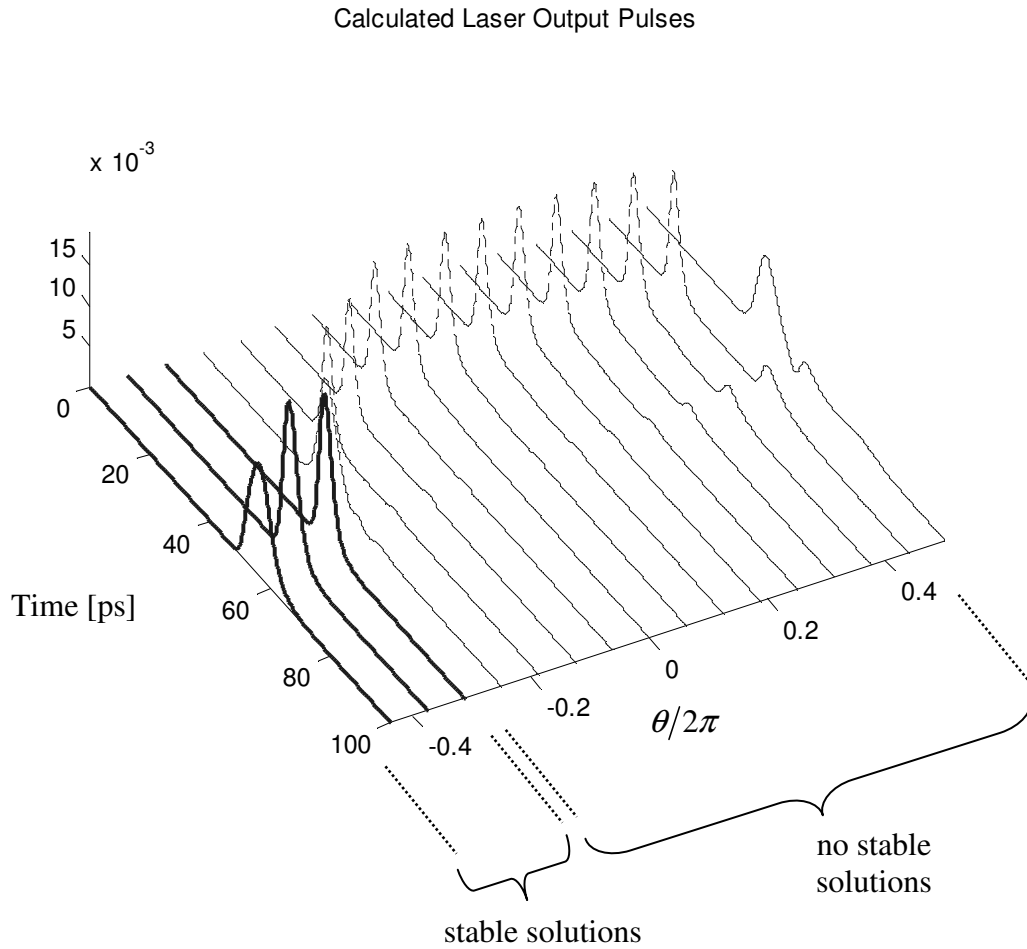


Figure 6.5: Calculated laser pulses for various values of θ .

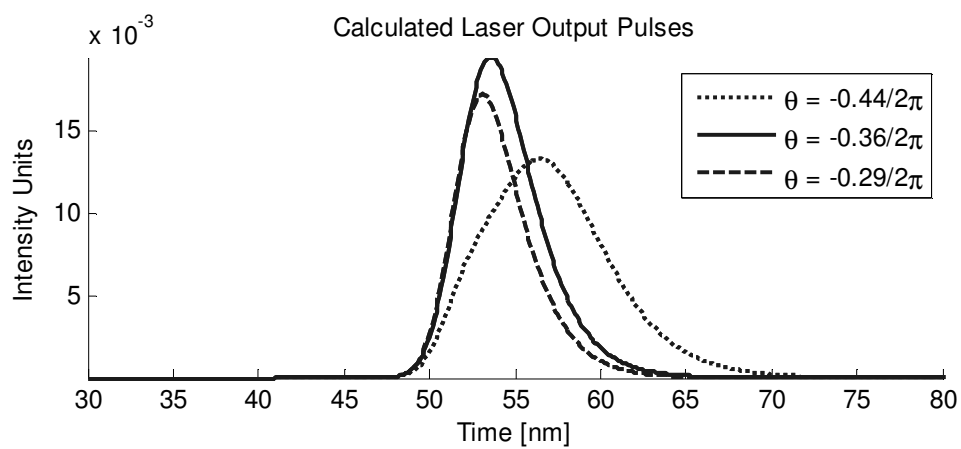


Figure 6.6: Selected calculated laser pulses for values of θ within the coherent injection locking range.

The simple theoretical model presented in this section requires much more work to accurately describe the proposed method of pulsed coherent injection locking of a mode-locked laser. As presented, the model assumes reasonable values for the unsaturated gain and absorption, linewidth enhancement factors, gain and absorption saturation energies, laser facet reflectivity and transmission, unsaturable loss, and the bandwidth of the spectral limiting element. Additional work must be performed to determine the actual values of these parameters.

In addition, the model neglects or inadequately addresses several potentially important effects. Most obviously, the model does not simulate the free-running laser. It merely examines the situation that results when a period pulse train is injected into the system. This neglects the complicated interaction between the injected and free-running signals. In addition, group velocity dispersion is not taken into account. Also, in using the Frantz-Nodvik relation, it is assumed that the saturable gain and absorption fully recover on each round trip. A more precise treatment would consider the effects of gain and saturation recovery.

Chapter 7: Conclusion

This thesis investigated a method for controlling the repetition rate and optical spectrum of a monolithic laser. The method is pulsed coherent injection locking of a mode-locked laser. In order to explain the operation of this laser system, theories of pulse propagation in a semiconductor amplifier, active and passive mode-locking of a monolithic laser, and CW coherent injection locking of a laser were presented.

A passively mode-locked laser is used as the basic device for generating an optical pulse train. This laser is injected by a clean, weak pulse train from an external source. The injected signal affects the passively mode-locked laser in two ways. First, it actively modulates the gain of the laser in order to lock its repetition rate. The passively mode-locked laser is biased in a regime such that its free-running repetition rate can be linearly tuned over a range of about 20 MHz. This allows it to be RF locked to a range of potential injection signals. The process of RF locking by active modulation is well understood and has been achieved by many researchers [1], [2], [3], [4].

Second, the injection signal coherently locks the optical spectrum of the laser signal. This effect distinguishes the proposed method from existing schemes. The coherent injection locking is achieved by matching the axial modes of the injected signal to those of the free-running laser. It is important to note that the free-running laser is a highly nonlinear device, and as such, its axial modes are not as clearly defined as those of a simple linear cavity. The precise axial modes of the free-running laser can only be defined when the laser is operated in the passively mode-

locked regime. In this regime, the laser produces a periodic train of pulses.

Regardless of the quality of these pulses, the periodicity demands that its optical spectra consist of discrete modes. If these modes are aligned to the modes of the injected signal, a process similar to CW injection locking occurs for each of the aligned modes.

A novel diagnostic was presented for determining the coherent injection locking status of the monolithic laser. The diagnostic relies on examining the total optical signal traveling away from the monolithic laser on the injection side. This total optical signal consists of the reflected portion of the injection signal and the output of the monolithic laser. If the laser is coherently locked, its output will experience destructive interference with the reflected injection signal. If it is not coherently locked, the destructive interference will not occur. This diagnostic method was successfully demonstrated for CW coherent injection locking. Although the situation of pulsed coherent locking is more complicated, the destructive interference effect was indeed observed and documented. However, it requires a substantial injection power. The power reduction effect was much less pronounced for a power ratio of 1/100 than for 1/10.

The experiments were performed using a self colliding pulse mode-locked laser fabricated by Arun Mampazhy, using a design by Dr. Christopher J. K. Richardson. The device was then jointly characterized by Arun Mampazhy and the author. The experiment indicates that while active mode-locking, or RF synchronization, is easy to achieve, the original goal of coherent injection locking is difficult to obtain. The experimental results show that the injection locked laser

signal is characterized by a shifting and distortion in spectrum, as well as a significant shifting in time. The spectral shift was qualitatively observed in a simple theoretical model. However, the model did not predict as big a temporal shift as was experimentally observed.

The results of this thesis showed that coherent injection locking of a monolithic mode-locked laser does not produce transform limited pulses. In order to achieve the original goal of a synchronized and coherent clock signal, further work is needed. The possibility of compressing the chirped pulses should be explored. In addition, distributed Bragg reflectors (DBR) should be considered as a candidate for spectral filtering and dispersion control. These features can be easily incorporated into the theoretical model to determine whether they may improve the operation of the system.

Appendix

```
clear all;

rho = 0.6; % field reflection coefficient
tau = sqrt( rho^2 - 1 ); % field transmission coefficient ( i*0.8
)

tmax = 100e-12; % the time window will go from 0 ps to
100 ps
dt = 0.1*(1e-12); % size of time steps ( 0.2 ps )
center = 50e-12; % the center of the time window ( 50 ps
)

t = 0:dt:tmax; % array of time values
N = length(t);

DT = max(t) - min(t); % total span of time window ( 100 ps )

df = 1/DT; % size of freq steps
DF = 1/dt; % total span of freq window

f = -(N-1)/2*df : df : (N-1)/2*df; % array of freq values (
centered at 0 Hz )

Esatg = 1*1e-12; % Saturation Energy of saturable amplifier
Esata = 0.2*1e-12; % Saturation Energy of saturable absorber

wP = 2.7*1e-12; % FWHM of the Injected Pulse (Intensity)
wE = wP*sqrt(2); % FWHM of the Injected Pulse (Field)
t0 = wP/sqrt(4*log(2)); % Gaussian parameter based on FWHM

Ein = 0.5*1e-12; % Energy in a single Injected Pulse
Ein0 = sqrt( Ein/( t0*sqrt(pi) ) ); % Maximum Field value of
Injected Pulse
Einj = Ein0*exp( -( (t-center)/wE ).^2)*4*log(2) ); % Injected
Pulse array
Einj_spec = fftshift(fft(Einj)); % spectrum of Injected Pulse

period = 100e-12; % Round Trip Time of laser cavity
n0 = 3.5; % effective group velocity in cavity
c = 3e8; % speed of light in vacuum
xtot = c/n0*period/2; % length of cavity (based on Round Trip
Time)

% To plot the spectrum in a familiar way,
% create an array of wavelength values corresponding to freq values
lambda0 = 1562e-9; % center wavelength of laser signal
f0 = c/n0/lambda0; % corresponding center frequency
f2 = f+f0; % shifted frequency scale, centered around
f0
```

```

lambda = c/n0./f2;          % array containing wavelength values

alphag = 3;                % Linewidth enhancement factor for Saturable
Amplifier
alphaa = 3;                % Linewidth enhancement factor for Saturable
Absorber

A0 = exp(-0.1);           % Unsaturated Absorption
G0 = exp(3);              % Unsaturated Gain

a0 = log(A0);
g0 = log(G0);

K = 0.1;                  % Unsaturable Absorption factor
Inj_frac = 0.1;

w = 5*1e11;               % FWHM of Frequency filter (Bandwidth
Limiting Element)
filter = exp( -4*log(2)*(f/w).^2 );      % Gaussian filter

% Cavity Phase Detuning "theta":
% Use only Option 1 or Option 2 for a given run

%%% Option 1: Full Range of theta from 0 to 2*pi
% n_theta = 31;
% theta = linspace(-0.5*2*pi , 0.5*2*pi , n_theta);

%%% Option 2: Restricted Range of theta for the coherent injection
locking range only
n_theta = 13;
dip0 = -0.36;
theta = linspace( (dip0-0.1)*2*pi , (dip0+0.1)*2*pi , n_theta );

% if set to 0, program will not generate intra-run plots (faster
runtime)
plot_toggle = 0;

% number of theta values
qmax = length( theta );

E1_all = zeros( qmax , N );
E1_spec_all = zeros( qmax , N );
Eout_spec_all = zeros( qmax , N );
Eout_all = zeros( qmax , N );

n_stop = zeros( 1 , qmax );
Error_stop = zeros( 1 , qmax );
Utot = zeros( 1 , qmax );
Uavg = zeros( 1 , qmax );

```

```

for q = 1:1:length(theta)

    (q-1)/length(theta)

    A = A0*ones( 1 , N );
    G = G0*ones( 1 , N );
    a = a0*ones( 1 , N );
    g = g0*ones( 1 , N );

    E1 = zeros( 1 , N );
    E2 = zeros( 1 , N );
    E3 = zeros( 1 , N );
    E4 = zeros( 1 , N );
    E5 = zeros( 1 , N );
    E6 = zeros( 1 , N );
    E7 = zeros( 1 , N );

    U1 = zeros( 1 , N );
    U2 = zeros( 1 , N );
    U3 = zeros( 1 , N );
    U4 = zeros( 1 , N );
    U5 = zeros( 1 , N );
    U6 = zeros( 1 , N );
    U7 = zeros( 1 , N );

    I1 = zeros( 1 , N );
    I2 = zeros( 1 , N );
    I3 = zeros( 1 , N );
    I4 = zeros( 1 , N );
    I5 = zeros( 1 , N );
    I6 = zeros( 1 , N );
    I7 = zeros( 1 , N );

    nmax = 60;
    U1N = zeros( 1 , nmax );
    U2N = zeros( 1 , nmax );
    U3N = zeros( 1 , nmax );
    U4N = zeros( 1 , nmax );
    U5N = zeros( 1 , nmax );
    U6N = zeros( 1 , nmax );
    U7N = zeros( 1 , nmax );

    cg = zeros( 1 , nmax );
    deltat = zeros( 1 , nmax );
    maxI1 = zeros( 1 , nmax );
    maxIout = zeros( 1 , nmax );
    Error = ones( 1 , nmax ); % Used to determine how much
    circulating pulse changes from one interation to the next
    Error_cur = 1;

```

```

Eout = zeros( 1 , N );
Iout = zeros( 1 , N );

I1_old = zeros( 1 , N );

A0new = A0;
a0new = a0;
G0new = G0;
g0new = g0;

Uout = 0;

n = 0;          % Counter for number of iteration

while n < nmax && Error_cur > 1e-6;
    n = n + 1;

    E1 = E1 + tau*Einj*Inj_frac;          % Injected pulse is added
    each round trip

    Eout = rho*Einj + tau*E1;
    Iout = abs(Eout).^2;

    Uout = (1/2)*( Iout(1) + Iout(N) + 2*sum(Iout(2:N-1)) )*dt;
    Uavg(q) = 0.95*Uavg(q) + 0.05*Uout;

%%% Saturable Gain
%%% Integrate cumulative input energy (Uin)
I1 = abs(E1).^2;
for cnt = 1:1:N
    U1(cnt) = (1/2)*( I1(1) + I1(cnt) + 2*sum(I1(2:cnt-1)) )*dt;
end

%%% Frantz Nodvik equation
G = G0new./(G0new - (G0new-1).*exp(-U1/Esatg));
g = log(G);

%%% Apply calculated gain to signal
E2 = exp(g/2).*exp( -i*alphag*g/2 ).*E1;
%%%

%%% Saturable Absorption
%%% Integrate cumulative input energy (Uin)
I2 = abs(E2).^2;
for cnt = 1:1:N
    U2(cnt) = (1/2)*( I2(1) + I2(cnt) + 2*sum(I2(2:cnt-1)) )*dt;
end

```

```

%%% Frantz Nodvik equation
A = A0new./(A0new - (A0new-1).*exp(-U2/Esata));
a = log(A);

%%% Apply calculated absorption to signal
E3 = exp(a/2).*exp( -i*alphaa*a/2 ).*E2;
%%%

I3 = abs(E3).^2;
for cnt = 1:1:N
    U3(cnt) = (1/2)*( I3(1) + I3(cnt) + 2*sum(I3(2:cnt-1)) )*dt;
end

E4 = sqrt(K)*E3;
I4 = abs(E4).^2;
for cnt = 1:1:N
    U4(cnt) = (1/2)*( I4(1) + I4(cnt) + 2*sum(I4(2:cnt-1)) )*dt;
end

%%% Spectral Filter (Bandwidth Limiting Element)
E4_spec = fftshift(fft(E4));
E5_spec = E4_spec.*filter;
E5 = ifft(ifftshift(E5_spec));
%%%

I5 = abs(E5).^2;
for cnt = 1:1:N
    U5(cnt) = (1/2)*( I5(1) + I5(cnt) + 2*sum(I5(2:cnt-1)) )*dt;
end

%%% Cavity Phase Tuning
E6 = E5*exp(i*theta(q));
%%%

I6 = abs(E6).^2;
for cnt = 1:1:N
    U6(cnt) = (1/2)*( I6(1) + I6(cnt) + 2*sum(I6(2:cnt-1)) )*dt;
end

U1N(n) = U1(N);
U2N(n) = U2(N);
U3N(n) = U3(N);
U4N(n) = U4(N);
U5N(n) = U5(N);
U6N(n) = U6(N);

```

```

    if plot_toggle == 1
        figure(1)
        hold off
        plot( t*1e12 , I1 , 'b' , ...
              t*1e12 , I2 , 'r' , ...
              t*1e12 , I3 , 'g' , ...
              t*1e12 , I4 , 'm' , ...
              t*1e12 , I5 , 'c' , ...
              t*1e12 , I6 , 'b:' )
        axis([42 58 0 0.3])

        figure(3)
        hold off
        plot( lambda*1e9 , abs(E4_spec).^2 , 'b' , ...
              lambda*1e9 , 100*abs(filter).^2 , 'g' )
        axis([1550 1575 -inf inf])
        grid;

        figure(5);
        if n == 1
            clf
        end
        hold on
        plot( U1N(n)*1e12 , U6N(n)*1e12 , 'b.' )
        plot( [0 1] , [0 1] , 'r' )
        axis([0 1 0 1])
        grid
        pause(0.2)
    end

    E1 = E6;

    %%% Window Shift

    deltat(n) = 1.5e-12;

    %%% Perform shifting of time window by
    %%% a phase shift that varies linearly with frequency
    E1_spec = fftshift(fft(E1));
    E1_spec = E1_spec.*exp(-i*2*pi*f*deltat(n));
    E1 = ifft(ifftshift(E1_spec));
    %%%

    %%% Check how much circulating pulse has changed from previous
    iteration
    Error(n) = sum( abs( I1 - I1_old ) );
    Error_cur = Error(n);
    %%%
    I1_old = I1;

```

```

        maxIout(n) = max(Iout);

end

n_stop(q) = n;
Error_stop(q) = Error(n);
Eout_spec_all(q,:) = fftshift(fft(Eout));
Eout_all(q,:) = Eout;
E1_all(q,:) = E1;
E1_spec_all(q,:) = fftshift(fft(E1));

pause(0.1)
end

figure(6)
plot( theta/(2*pi) , Uavg/max(Uavg) , 'LineWidth' , 2)
xlabel('Cavity Tuning, in terms of Cavity Phase Shift \theta/(2\pi)
')
ylabel('Normalized Reflected Power')
title('Calculated Reflected Power Diagnostic')

figure(7)
plot( theta/(2*pi) , n_stop )

lb = 544;
la = 473;

%% Plots calculated spectra for all theta values specified
figure(8)
for m = 2:1:4
    plot3( lambda(la:lb)*1e9 , theta(m)*ones(1,lb-la+1)/(2*pi) ,
abs(E1_spec_all(m,la:lb)).^2 , 'b' , 'LineWidth', 2)
    hold on
end
for m = 5:1:length(theta)
    plot3( lambda(la:lb)*1e9 , theta(m)*ones(1,lb-la+1)/(2*pi) ,
abs(E1_spec_all(m,la:lb)).^2 , 'b:' , 'LineWidth', 1 )
    hold on
end
axis([1550 1570 -inf inf -inf inf])
hold off
title('Calculated Laser Output Spectra')

%% Use figure(9) only for Option 2 of theta values
figure(9)
hold on
plot( lambda*1e9 , abs(E1_spec_all(2,:)).^2 , 'b:' , 'LineWidth',2 )
plot( lambda*1e9 , abs(E1_spec_all(7,:)).^2 , 'b' , 'LineWidth',2 )

```

```

plot( lambda*1e9 , abs(E1_spec_all(11,:)).^2 , 'b--' , 'LineWidth',2
)
axis([1550 1570 -inf inf])
legend( '\theta = -0.44/2\pi' , ...
        '\theta = -0.36/2\pi' , ...
        '\theta = -0.29/2\pi' )
xlabel('Wavelength \lambda [nm]')
ylabel('Intensity Units')
title('Calculated Laser Output Spectra')

%%% Plots calculated pulses for all theta values specified
figure(10)
for m = 2:1:4
    plot3( t*1e12 , theta(m)*ones(1,N)/(2*pi), abs(E1_all(m,:)).^2
, 'b' , 'LineWidth',2 )
    hold on
end
for m = 5:1:length(theta)
    plot3( t*1e12 , theta(m)*ones(1,N)/(2*pi), abs(E1_all(m,:)).^2
, 'b:' , 'LineWidth',1)
    hold on
end
axis([0 100 -inf inf -inf inf])
hold off
title('Calculated Laser Output Pulses')

%%% Use figure(11) only for theta values of Option 2
figure(11)
hold on
plot( t*1e12 , abs(E1_all(2,:)).^2 , 'b:' , 'LineWidth',2 )
plot( t*1e12 , abs(E1_all(7,:)).^2 , 'b' , 'LineWidth',2 )
plot( t*1e12 , abs(E1_all(11,:)).^2 , 'b--' , 'LineWidth',2 )
axis([30 80 -inf inf -inf inf])
legend( '\theta = -0.44/2\pi' , ...
        '\theta = -0.36/2\pi' , ...
        '\theta = -0.29/2\pi' )
xlabel('Time [nm]')
ylabel('Intensity Units')
title('Calculated Laser Output Pulses')

```

Bibliography

- [1] B.K. Mathason and P.J. Delfyett, "Pulsed Injection Locking Dynamics of Passively Mode-Locked External-Cavity Semiconductor Laser Systems for All-Optical Clock Recovery," *J. Lightwave Tech.*, 18, 1111-1120 (2000).
- [2] K. Smith and J.K. Lucek, "All-Optical Clock Recovery Using A Mode-Locked Laser," *Electronics Letters*, 28, 1814-1816 (1992).
- [3] X. Wang, H. Yokoyama, and T. Shimizu, "Synchronized Harmonic Frequency Mode-Locking with Laser Diodes through Optical Pulse Train Injection," *IEEE Photon. Technol. Lett.*, 8, 617-619 (1996).
- [4] A. Nirmalathas, H.F. Liu, Z. Ahmed, D. Novak, and Y. Ogawa, "Subharmonic Synchronous Mode-Locking of a Monolithic Semiconductor Laser Operating at Millimeter-Wave Frequencies," *IEEE J. Sel. Top. Quantum Electron.*, 3, 261-296 (1997).
- [5] Z. Ahmed, H.F. Liu, D. Novak, Y. Ogawa, M.D. Pelusi, and D.Y. Kim, "Locking Characteristics of a Passively Mode-Locked Monolithic DBR Laser Stabilized by Optical Injection," *IEEE Photon. Technol. Lett.*, 8, 37-39 (1996).
- [6] H. Kurita, T. Shimizu, and H. Yokoyama, "Experimental Investigations of Harmonic Synchronization Conditions and Mechanisms of Mode-Locked Laser Diodes Induced by Optical-Pulse Injection," *IEEE J. Sel. Top. Quantum Electron.*, 2, 508-513 (1996)
- [7] R.W. Boyd, *Nonlinear Optics* (Academic Press, San Diego, CA, 1992).

- [8] S.-Y. Tseng, "Development of Linear and Nonlinear Components for Integrated Optical Signal Processing," Ph.D. dissertation (University of Maryland, College Park, USA, 2006).
- [9] A. E. Siegman, *Lasers* (University Science Books, Sausalito, 1986).
- [10] G. P. Agrawal and N. A. Olsson, "Self-Phase Modulation and Spectral Broadening of Optical Pulses in Semiconductor Laser Amplifiers," *IEEE J. Quantum Electron.* 25, 2297-2306 (1989).
- [11] L. Duan, "Smoothly Wavelength-Tunable, Harmonically Mode-Locked Fiber Ring Lasers," Ph.D. dissertation (University of Maryland, College Park, USA, 2002).
- [12] A. Yariv, *Quantum Electronics* (John Wiley & Sons, Inc., California Institute of Technology, 1989).
- [13] E.A. Avrutin, J.H. Marsh, and E.L. Portnoi, "Monolithic and multi-GigaHertz mode-locked semiconductor lasers: Constructions, experiments, models and applications," *IEE Proc.-Optoelectron.*, 147, 251-278 (2000).
- [14] D.J. Derickson, R.J. Helkey, A. Mar, J.R. Karin, J.G. Wasserbauer, and J.E. Bowers, "Short Pulse Generation Using Multisegment Mode-Locked Semiconductor Lasers," *IEEE J. Quantum Electron.*, 28, 2186-2202 (1992).
- [15] H.A. Haus, "Theory of Mode Locking with a Slow Saturable Absorber," *IEEE J. Quantum Electron.*, 11, 736-746 (1975).
- [16] K.Y. Lau, "Short-Pulse and High-Frequency Signal Generation in Semiconductor Lasers," *J. Lightwave Technol.*, 7, 400-419 (1989).

- [17] P.-T. Ho, L.A. Glasser, E.P. Ippen, and H.A. Haus, "Picosecond pulse generation with a cw GaAlAs laser diode," *Appl. Phys. Lett.*, 33, 241-242 (1978).
- [18] D.J. Derickson, P.A. Morton, and J.E. Bowers, "Comparison of timing jitter in external and monolithic cavity mode-locked semiconductor lasers," *Appl. Phys. Lett.*, 59, 3372-3374 (1991).
- [19] R.G.M.P. Koumans and R. van Roijen, "Theory for Passive Mode-Locking in Semiconductor Laser Structures Including the Effects of Self-Phase Modulation, Dispersion, and Pulse Collisions," *IEEE J. Quantum Electron.*, 32, 478-492 (1996).
- [20] Y.-K. Chen and M.C. Wu, "Monolithic Colliding-Pulse Mode-Locked Quantum-Well Lasers," *IEEE J. Quantum Electron.*, 28, 2176-2185 (1992).
- [21] S.D. Brorson, Z. Wang, T. Franck, S. Bischoff, A. Møller-Larsen, J.M. Nielsen, J. Mørk, and M.P. Sørensen, "Characterization of Wavelength Chirping in Modelocked Monolithic CPM Lasers," *IEEE Photon. Technol. Lett.*, 7, 1148-1150 (1995).
- [22] J.P. Hohimer and G.A. Vawter, "Passive mode locking of monolithic semiconductor ring lasers at 86 GHz," *Appl. Phys. Lett.*, 63, 1598-1600 (1993).
- [23] F. Camacho, E.A. Avrutin, P. Cusumano, A. Saher Helmy, A.C. Bryce, and J.H. Marsh, "Improvements in Mode-Locked Semiconductor Diode Lasers Using Monolithically Integrated Passive Waveguides Made by Quantum-Well Intermixing," *IEEE Photon. Technol. Lett.*, 9, 1208-1210 (1997).

- [24] C.J.K. Richardson and J. Goldhar, "Solid-State Repetition-Rate Tunable Semiconductor Colliding-Pulse Mode-Locked Laser," *IEEE Photon. Technol. Lett.*, 16, 978-980 (2004).
- [25] S. Arahira and Y. Ogawa, "Repetition-Frequency Tuning of Monolithic Passively Mode-Locked Semiconductor Lasers with Integrated Extended Cavities," *IEEE J. Quantum. Electron.*, 33, 255-264 (1997).